Experimental determination of the lacunar-canalicular permeability using cyclic loading

by

Mohammed Benalla

A dissertation submitted to the Graduate Faculty in Engineering in partial fulfillment of the requirements for the degree of Doctor of Philosophy, The City University of New York

2012

This manuscript has been read and accepted for the Graduate Faculty in Engineering satisfaction of the dissertation requirement for the degree of Doctor of Philosophy in Biomedical Engineering

_____	_____
Date	Professor Stephen C. Cowin, Ph.D. Chair of Examining Committee
_____	_____
Date	Professor Luis Cardoso, Ph.D. Co-Mentor
_____	_____
Date	Professor Mumtaz Kassir, Ph.D. Executive Officer

Susannah P. Fritton, Ph.D., *Biomed. Engr., CCNY*

Ali M. Sadegh, Ph.D., *Mech. Engr., CCNY*

Gaffar Gailani, Ph.D, *Mech. Engr. Tech., NYCCT*

Supervision Committee

THE CITY UNIVERSITY OF NEW YORK

Abstract

Experimental determination of the lacunar-canalicular permeability using cyclic loading

By

Mohammed Benalla

Adviser: Professor Stephen C. Cowin

Co-Advisor: Professor Luis Cardoso

Current theoretical and experimental evidence suggests that the sensory bone cells are activated by the induced drag from fluid flowing through the lacunar-canalicular porosity, PLC. One of the most important parameters of the interstitial fluid flow is the PLC permeability. However, the reported experimental measurements of this permeability are several orders of magnitude below the values predicted by analytical studies. The discrepancy between theoretical and experimental values of PLC permeability could be due to the assumptions considered in the formulation of analytical models, the estimation of unknown parameters, the difficulty to perform experiments on the PLC without the influence of the vascular porosity, PV, as well as the lack of freshness, type and origin of samples.

In this thesis, innovative analytical and experimental approaches were proposed to accurately estimate the PLC permeability that was determined in a single osteon, a domain in which the PLC can be separated from the PV. The osteon was idealized as a poroelastic annular disk, and the loss tangent was investigated at different loading frequencies. A sensitivity study of the analytical model has showed that the porosity is the most influential parameter, and that the loss tangent was frequency dependent.

The PLC permeability was determined based on experimental measurements of loss tangent on human osteons that were curve fitted to the analytical model at different frequencies. The novelty in determining the PLC permeability in this research stems from several aspects that have been neglected in previous studies. First, the use of fresh human samples that include the PLC and exclude the PV. Second, measurement of the model parameters independently for each osteon. Third, the frequency dependence of the PLC permeability was measured.

The study showed that the loss-tangent of the osteon changes a few hours after isolation of the sample and that the lack of freshness could be an important factor on the large variability in PLC permeability in literature. It was also discovered that there exist a strong correlation between porosity and PLC permeability. The average PLC permeability in 60 human osteons was found to be $(6.15\pm0.83)10^{-22}\ m^2$, in agreement with previously reported values.

To
My Whole Family
Especially
My Lovely
Mother & Father,

Acknowledgments

I am profoundly grateful to so many people who have been part of my life during these last four years and contributed to the accomplishment of this thesis.

Foremost, I would like to express my heartily gratitude and sincere appreciation to my mentor Professor Stephen Cowin for his guidance and patience throughout my PhD studies. His doors were always open when I needed his advice. His clear and simple explanations for complicated problems helped me find my way through this thesis. I am really thankful for his encouragement, support and the way he enriched my growth as student as well as the man of science I want to be.

I am deeply thankful to Professor Luis Cardoso for his advice, supervision and vital contribution to this thesis. I am really thankful for his encouragement and support as a professor and as a friend during the hardest times of this graduate study.

I wish to extend my special gratitude to Professor Susannah Fritton for here careful following and wonderful guidance during my PhD terms and for the wonderful course she taught me. Many thanks go to Professor Ali Sadegh for his warm encouragement and valuable suggestions during my second exam. Special thanks go also to the AGEP program in the person of Dr. Gail Smith for her advice.

I would like to thank my best friend Dr. Gaffar Gailani for his advice and moral support during my graduate study and lab-mates, Divya Sharma, Mohammad Souzanchi and Paolo Palacio for the wonderful discussions we had and great time we spent together.

Finally, but not least I would like to thank my wonderful family. My parents deserve a special acknowledgement. My mother Fatima and my father Ali were the first people who showed me the path of the learning process and encouraged me to enjoy it since ever, my brothers and sisters for their encouragements and my sweet wife, who is in process of increasing our family size, for her love and support.

At the end, I would like to present my apology to all those who contributed from close or far to the successful realization of this thesis and I couldn't mention their names. Words fail me to express my appreciation and sincere gratitude.

Table of Contents

List of tables

List of figures

Nomenclatures

$\hat{A}_r$, $\hat{A}_\theta$, $\hat{A}_z$	Three components of the 6D vector representing the Biot effective stress coefficient for PLC
r	arbitrary radius of the osteon
r_o	outer radius of the osteon
r_i	inner radius of the osteon
a	non-dimensional inner radius of the osteon ($a = r_i / r_o$)
$\hat{\mathbf{C}}^i$	($i = m, d, u$) elasticity or stiffness matrix for the matrix material, drained elastic constants and undrained elastic constants (2^{nd} order tensor in 6D)
c	pore fluid pressure diffusion constant in the lacunar-canalicular porosity
C^*	dynamic elastic modulus
$\hat{\boldsymbol{E}}$	strain, a vector in 6D, equivalent to the strain tensor in 3D
E	modulus of elasticity
f_o	constant of integration determined in equation (15)
I_o, I_1	modified Bessel functions of the first kind
i	imaginary number ($i = \sqrt{-1}$)
K^f	compressibility of the fluid
K^i_{Reff}	Reuss lower bound on the effective (isotropic) bulk modulus of the anisotropic elastic material ($i = m, d$)
K_o, K_1	modified Bessel functions of the second kind

K_{rr}	radial permeability
$\tilde{p}(r,t)$	pore fluid pressure in the PLC
$\tilde{u}(r,t)$	displacement vector
ber_n	real part of Kelvin functions (n= 0, 1)
bei_n	imaginary part of Kelvin functions (n= 0, 1)

Greek Symbols

ε_o	strain amplitude of the cyclic applied strain
ϕ	porosity
λ	ratio of r / r_o (non-dimensional)
ω	angular frequency associated with the cyclic loading
$\bar{\omega}$	dimensionless angular frequency
μ	viscosity of the pore fluid
ν_{ij}	Poisson's ratios ($i, j = r, \theta, z$)
σ^*	average resultant stress due the applied cyclic strain
σ_o	magnitude of the average resultant stress
Υ	constant of dimension force
Λ	solid-fluid compliance contrast coefficient
$\tilde{\zeta}(r,t)$	variation of fluid content and
d	phase angle

Subscripts and Superscripts

d	indicates the drained condition of the porous solid

u	indicates the undrained condition of the porous solid
f	indicates the fluid component
m	indicates the matrix material of the porous solid

Chapter 1

Introduction

1.1. Background

Beyond its function in transporting nutrients to osteocytes contained in the lacunae and taking away their wastes, bone fluid is believed to play a major role in the mechanosensory process. Understanding mechanosensory phenomena will shed more light on how to deal with osteoporosis, how to cope with microgravity and how to increase the longevity of bone implants.

Several characteristics of bone microarchitecture, such as porosity, lacunae density, canalicular number and canalicular tortuosity are believed to contribute to the permeability in the lacunar-canalicular porosity, PLC. For instance, an increase in the PLC or canalicular number will reduce the interstitial fluid flow resistivity, and increase the intrinsic permeability of the PLC, while an increase in canaliculi tortuosity would produce the opposite effect.

The interconnection between the vascular porosity (PV) and PLC has also an important effect on interstitial fluid flow. Indeed, the difference in pore size of the PV and the PLC has an effect on the pressure gradient between these two systems. The pressure gradients in the PLC system are responsible for driving the fluid flow. These pressure gradients are produced by deformation in the mineralized matrix during bone loading, which in turn depend on the magnitude of the load applied to bone and the stiffness of the mineralized matrix material. The bone matrix material is composed of minerals and proteins in addition to water. The way these constituents are combined together renders the osseous tissue stiff and light weight. Thus, the stiffness of the matrix material plays an important role on the infinitesimal deformations that the bone tissue undergoes under mechanical loading, the pressure gradients generated in the PV and PLC systems, and the mechanosensation by osteocytes.

1.2. Bone structure and constitution

At the macroscopic level, skeletal tissue is generally composed of two architectural structures, i) cortical or compact bone and ii) trabecular or cancellous bone (Figures 1-1). On the microscopic level, cortical bone contains three levels of porosity nested one inside the other as a set of a Russian dolls. The three porosities are the vascular porosity (PV), the canaliculi in the lacunar-canalicular porosity (PLC) and the collagen-apatite porosity (PCA).

The walls of the PV and the PLC porosities are composed roughly of 70% minerals, mainly hydroxyapatite, and 22% proteins, mainly type I collagen and 8% of water. The hydroxyapatite is a brittle material while type I collagen is a soft material. The way these materials are organized in varied hierarchical scales (Figure 1-2) renders the bone tough and lightweight. At the lowest level of the cortical bone structure, each individual fiber is composed of an array of mineralized collagen fibrils. The mineralized collagen fibrils, which are roughly 100 nm in diameter and 5 – 10 μm in length, are the basic constituent of the matrix material. The fibrils consist of an assembly of 300 nm long and 1 nm thick collagen molecules. The collagen fibrils are fastened and covered by tiny mineral crystals of hydroxyapatite. These crystals are parallel and tiny layers with a thickness of 1.5 – 4.5 nm. With growth and maturation the fibrils become mineralized. At the nano-scale dimension, the collagen fibrils are formed by staggered arrays of collagen molecules, each molecule is built of three polypeptides twisted in a triple helical rope and stabilized by hydrogen bonding between residues. The component of each tropocollagen is a glycine amino acid composed from proline and hydroxyproline. The outstanding features of bone, such as toughness, lightweight and energy dissipation, are more related to the way the seven hierarchical levels of structures are organized, Figure 1-2.

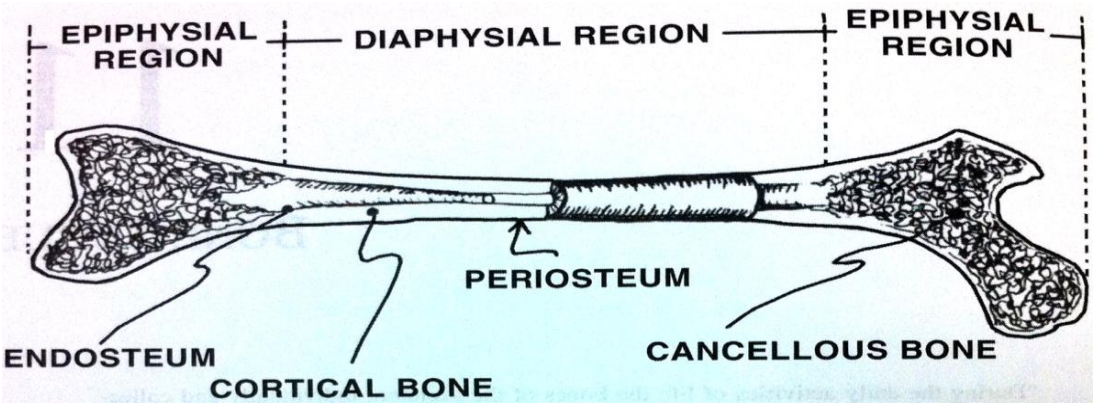

Figure 1-1. *Longitudinal section of the femur illustrating cancellous and cortical bone types (Adapted from Cowin, 1981)*

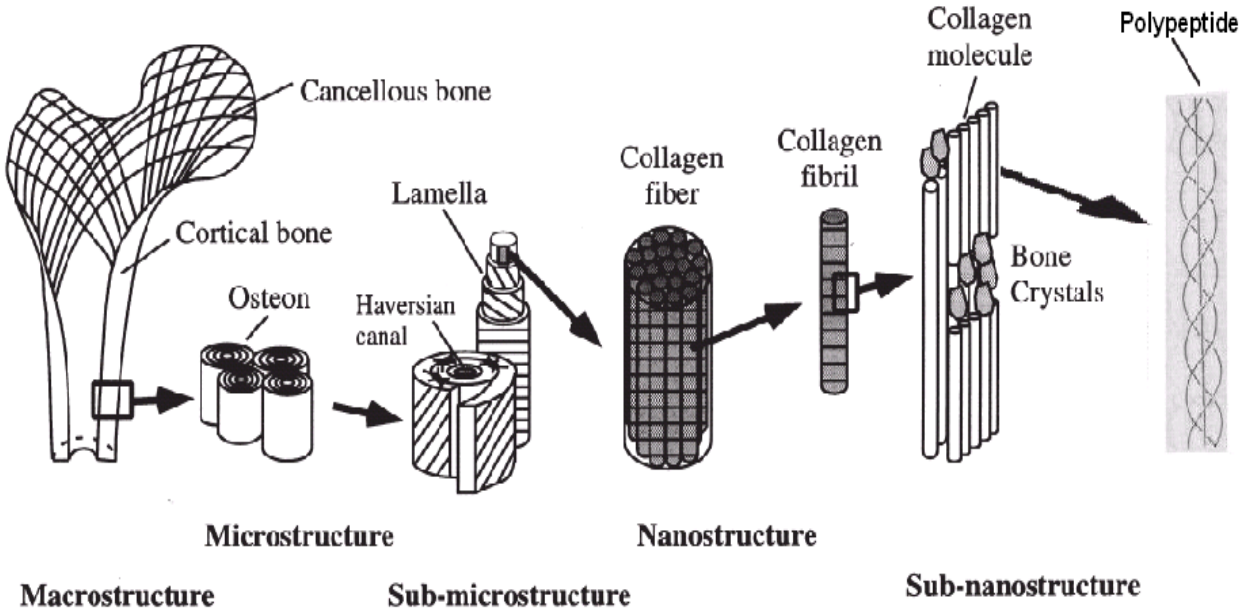

Figure 1-2. *Hierarchical structure of bone; (a) bone tissue, macroscopic structure; (b) osteons (~100 µm); (c) lamellae (3-7 µm); (d) collagen fiber (~ 100 nm); (e) collagen fibril (~ 1 nm); (f) collagen molecule and mineral crystals; (g) tropocollagen. Adapted from Vankan et al., (1996)*

1.3. Bone porosities

There are three different levels of porosity contained in the osteon, the bone microstructure. The largest pore size is approximately 50 μm diameter and associated with the vascular porosity (PV), the second largest pore size is approximately 0.3 μm diameter and associated with the canaliculi in the lacunar canalicular porosity (PLC), while the smallest pore is approximately 10 nm diameter and associated with the collagen-apatite porosity, PCA (Figure 1-2), Cowin and Doty (2007). The PV consists of the Haversian and Volkmann canals.

The Haversian lumens are vertical and run approximately along the centerline of osteons; they are connected horizontally to each other via the Volkmann canals. The PLC is composed of the lacunae and the canaliculi. The lacunae have an approximately elliptical shape and contain the osteocytes, the sensory bone cells, while the canaliculi contain the osteocytic processes that connect the osteocytes in the lacunae to each other and to the osteoblasts lining the wall separating the PLC from the PV. There is no fluid flow in the PCA because all the molecules of water inside this porosity are bounded by interaction to the ionic crystals (Cowin 1999). The interstitial fluid in the other two large porosities, the PV and the PLC, has the ability to flow from porosity size to other. The bone fluid flow arises from the difference of the pore pressures created in the two porosities. The pressure gradient in the PLC mainly originates from the applied external loadings that bone undergoes. Beyond the interstitial fluid the two porosities contain soft tissues as well. The soft tissues housed in the two porosities are divided to three categories, blood vessels, nerves and bone cells. The two first categories are housed in the PV while the location of the bone cells depend upon bone cell type, as described in the following section.

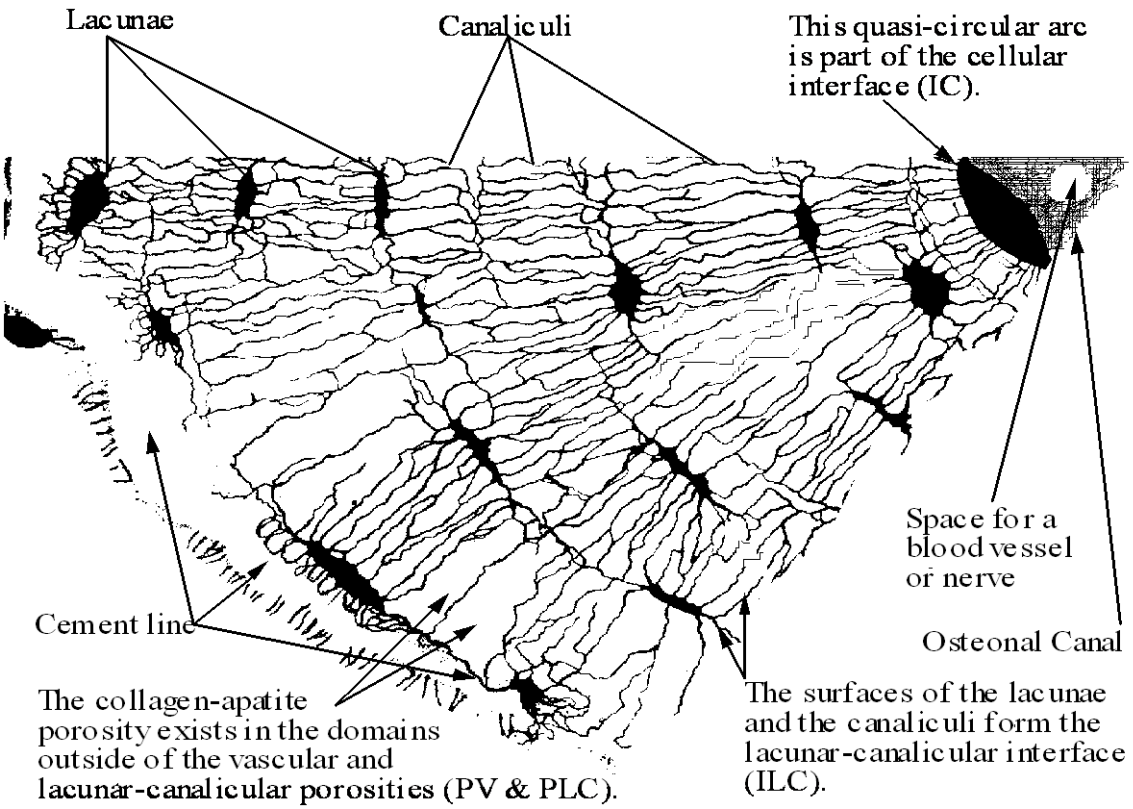

Figure 1-3*. A pie-shaped section of an osteon. The osteonal canal is on the upper right, the cement line to the left. The osteonal canal is part of the vascular porosity (PV), the lacunae and the canaliculi are part of the lacunar-canalicular porosity (PLC) and the material in the space that is neither PV or PLC contains the collagen-apatite porosity (PCA).The three interfaces, the cement line, the cellular interface (IC) and the lacunar-canalicular interface are each indicated. The radius of an osteon is usually about 100 μm, and the long axis of a lacuna is about 15 μm. Using this information it should be possible to establish the approximate scale of the printed version of this illustration. (Adapted from Cowin, 1999)*

1.4. Bone cells

There are three types of bone cells: osteocytes, osteoblasts, and osteoclasts (Figure 1-3): Osteocytes are the most abundant cells in bone. A representative area of 1 mm^2 of mature human femoral bone contains approximately 650 osteocytes Vashisht et al. (2000). Osteocytes are the only cells inside the mineralized matrix of the PLC porosity. In the three dimensional directions, each osteocyte radiates roughly 62 cell processes (Remaggi et al., 1998) that run along the canaliculi porosity and communicate with neighboring cells, osteocytes and osteoblasts (Cowin and Doty, 2007). Processes of two different cells are connected with a gap junction. Osteocytes are believed to be the sensory bone cells.

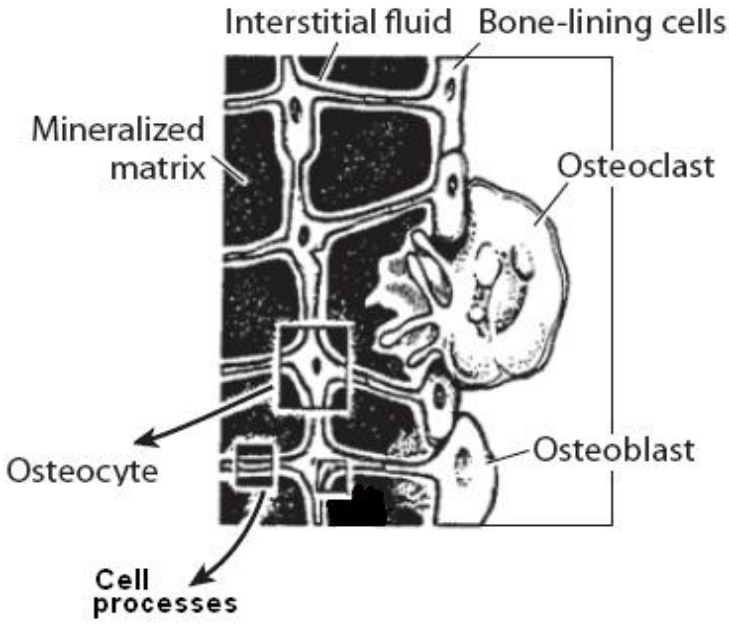

Figure 1-4. *Bone cells (adapted from Rubin et al., 1990)*

Osteoblasts are connected to each other and to osteocytes by gap junctions. They line the internal wall of the vascular porosity and attach to the osteocytes cell processes through the

canaliculi. Bone growth and remodeling are performed by osteoblasts. While fulfilling their duty, the entrapped osteoblasts inside the matrix differentiate gradually to osteocytes.

Osteoclasts are multi-nucleated large cells present in the interstitial fluid of the PV close to the osteoblasts. They are responsible for bone resorption. Osteoclasts encompass from 2 to 50 nuclei and have diameters that may reach 100 µm (Cowin and Doty, 1989).

1.5 Bone mechanosensory and mechanotransduction mechanisms

Due to the weight bearing and muscles contractions osseous tissue is continuously subjected to mechanical loadings. Under this mechanical loading bone is subjected to infinitesimal deformations that create pressure gradients inside the bone porosities that are completely filled with interstitial fluid. These changes of pressure cause the bone fluid to flow from the regions of higher pressure to the regions of lower pressure. This fluid motion is sensed by the bone cells and is considered to be the signal for bone adaptation, Han et al (2004). The manner in which mechanical loading-drives bone to resorb and remodel is still poorly understood and researchers are still struggling to deepen their understanding of the process.

1.5.1. Mechanosensory phenomenon

It has become accepted that bone modeling and remodeling processes are performed by the orchestrated action of three different types of bone cells. Osteocytes are the only cells contained inside the bone matrix and the best candidates to sense the effect of load. After sensing the mechanical loads, osteocytes are believed to send a cellular signaling to osteoclasts and osteoblasts in order to start the resorption and the remodeling activities, respectively. *In vitro* experiments with sensory bone cells reveal that cellular-level strains greater than 5000 microstrain (µε) are required to excite osteocytes, Fritton and Weinbaum (2009). However, 5000 µε may cause damage to the bone structure since the maximum

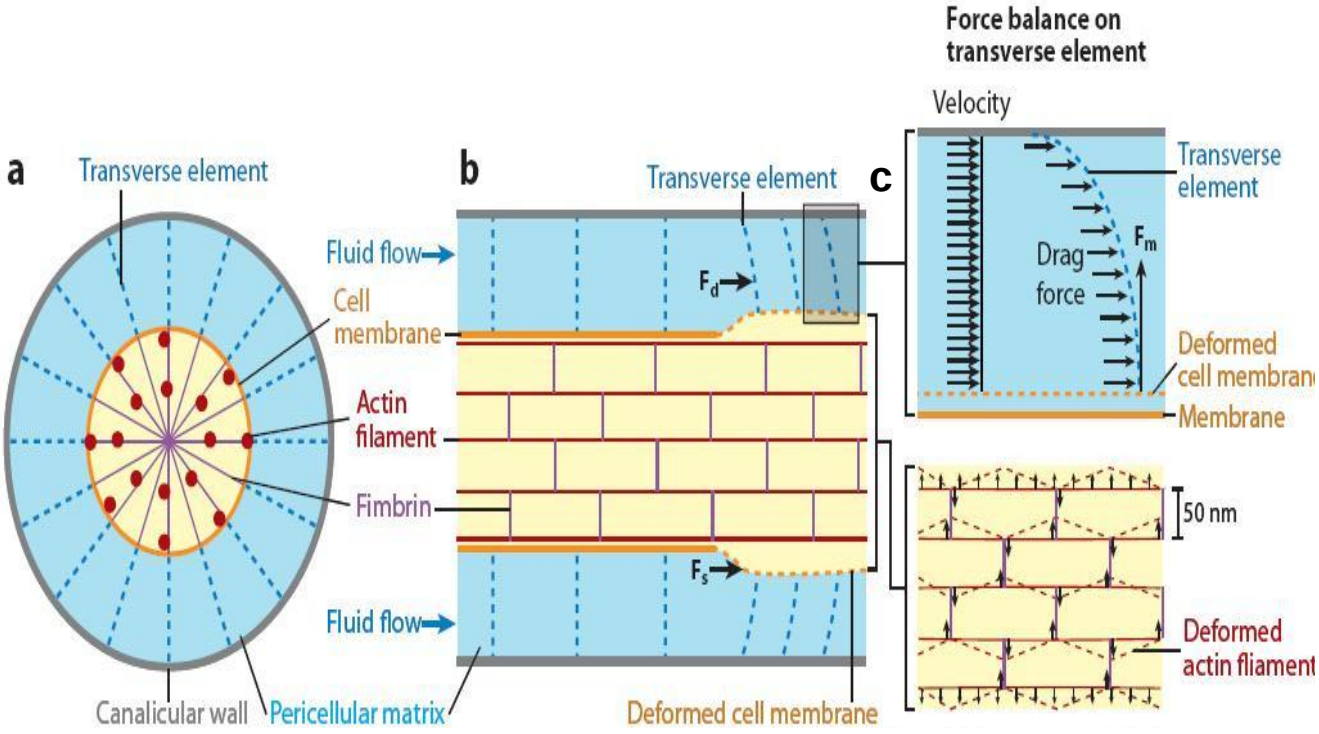

Figure 1-4. *Strain amplification showing osteocyte process in cross section. (a) Longitudinal. (b) Transverse. (c) Interstitial fluid drug force and deformation of actin filament. (Adopted from You et al., 2001)*

physiological strain bone can barely reach is 2000 με approximately (Burr et al. 1996, Fritton and Rubin 2001).

Several studies have demonstrated that the interstitial fluid flow induced by mechanical loading may amplify the cellular level strain sensation. One of the developed scenarios that explain how the interstitial fluid amplifies the strain cellular level is based on the fluid shear stress applied on the osteocyte plasma membrane and process. A second scenario assumed that the deformation of the cytoskeleton processes (Figure 1-4) is caused by the drag force applied by the fluid flow on the pericellular matrix. The latter assumption is believed to deform the osteocyte processes and extend the tethering fibers in more pronounced way than the fluid shear stress does, which raises the cellular strain to the required level (Fritton and Weinbaum, 2009). Once the osteocytes are excited, the mechanosensory phenomenon is completed and the mechanotransduction phenomenon begins.

1.5.2. Mechanotransduction phenomenon

It is still unclear how the mechanical loadings initiate cellular responses in order to adjust the bone structure. Several explanations are suggested to explain this conversion process. As the osteocytes are the sensory cells, they should be able to translate their sensation into a biochemical signal in order to orchestrate the functionality of the working cells, osteoblasts and osteoclasts. Actually, it is believed that the osteocytes can manage bone resorption and remodeling in different steps (Turner and Pavalko, 1998). Some researches indicate that apoptotic osteocytes or damaged bone matrix areas may represent a determinant motive in locating the resorption zone, Lanyon (1993). In this case, the osteocytes are believed to activate and direct the osteoclasts to the resorption site by secreting nitric oxide (NO) and prostaglandins that are transported via the interstitial fluid, Burger and Klein-Nulend (1999). Once the osteoclasts reach the resorption site, they start removing the old bone. The osteoclasts cease their

activities and leave the resorbed spot once the old bone is removed. Afterwards, osteocytes may activate osteoblasts in two different ways. One way is via intracellular pathways trough gap junctions with calcium ions (Ca^{2+}) and the second is by secretion of substances into the interstitial fluid similarly to the way the osteoclasts are activated. After being activated osteoblasts fill in the resorption cavity and begin forming new bone by depositing osteoid matrix mainly composed from type I collagen. The collagen is then mineralized which increases its stiffness.

1.5.3 Bone permeability

Permeability is a constant that indicates the ability of a poroelastic material to transmit fluid within its porous medium. Thus, the importance of bone permeability stems from its aspect as a key parameter determining the interstitial fluid flow. Since the intrinsic architecture of the bone porosity is composed fof two domains with two orders of magnitude difference in size, the pore fluid flow behaves differently in the PLC than in the PV. Therefore, the consideration of bone permeability is divided in a PV permeability and PLC permeability.

1.5.3.1. The PV Permeability

The PV porosity consists of the Volkmann and Haversian canals. This porosity is a low-pore-fluid-pressure domain because the PV permeability has a sufficiently large pore size to permit a fast decay of the pressure pulse. As the PV contains thin walled blood vessels carrying blood with a pressure of 40 to 60 mmHg a large PV pressure could cause the blood vessels to collapse, another reason for the PV pressure to not greatly exceed the blood pressure. The PV

permeability is roughly estimated between 10^{-11} and 10^{-15} m^2, Zhang et al. (1998) and Dellaman et al. (1991), respectively.

1.5.3.2. The PLC Permeability

The PLC permeability is associated with the lacunae where the osteocytes reside and with the canaliculi where the osteocyte processes exist. The osteocyte processes are connected to each other via gap junctions. The fact that the pores of this porosity have a diameter two orders of magnitude smaller than that of the PV reduces its permeability and therefore raises the pore fluid pressure over that in the PV and creates fluid flow between the two chambers. The interstitial fluid flow in the PLC is believed to be a significant factor in the mechanosensory and mechanotransduction phenomenon. However, the measurement of the permeability of the PLC has not been accomplished with sufficient accuracy to date. The main reason is related to the topological intertwining of the PV with the PLC. The values of the PLC permeability reported in the past are questioned. The reason why the accuracy of these values of the PLC permeability are questioned is related to the fact that most of them represent a combined PLC and PV measurement rather than a PLC measurement alone. In the last 21 years the value of the PLC permeability have decreased from $k_{rr} = 1.47\ 10^{-20}$ m^2 (Zhang et al. 1998) to $k_{rr} = 5\ 10^{-25}$ m^2 (Gailani et al. 2009) in certain loading cases. The history of the determination of the PLC permeability shows that this fluid flow property is still challenging. For this reason researchers are still developing new approaches in order to determine the PLC permeability accurately.

In this thesis, a description of the poroelastic boundary value problems employed to model the flow of interstitial pore fluid between lacunae and canaliculi in bone tissue are formulated in §3. In §3, solution to these boundary value problems is obtained and formulation

of the analytical model of the loss tangent is expressed. Experimental determination of the PLC permeability based on a curve fitting of the analytical model vs. experimental data of the loss tangent that an osteonal specimen exhibits under cyclic loading are performed in §4. Also, a novel investigation of the PLC permeability with respect to frequency as well as the relationship relating the permeability and the porosity in the lacunar canalicular system are investigated in §4. In last chapter a general conclusion along with future works are discussed.

References

Abramowitz M, Stegun IA (1964) Handbook of Mathematical functions with Formulas, Graphs

and Mathematical Tables. National Bureau of Standards Applied Mathematics Series 55, 379- 80

Bonivtch AR, Bonewald LF, Nicolella DP (2007) Tissue strain amplification at the osteocyte lacuna: a microstructural finite element analysis. J Biomech 40(10):2199-2206.

Burr DB, Milgrom C, Fyhrie D, Forwood M, Nyska M (1996) In vivo measurement of human tibialstrains during vigorous activity. Bone 18:405–10

Burger EH, Klein-Nulend J (1999) Mechanotransduction in bone-role of the lacuno-canalicular network. FASEB J. ;13:S101–12.

Cowin SC (1999) Bone poroelasticity. J. Biomech. 32: 217-238

Cowin SC (1981) Mechanical properties of bone. Mechanical of structured media. APS Selvadurai. pp 151- 184.

Cowin SC, Doty SB (2007) Tissue Mechanics. Springer. pp 350, 352

Cowin SC, Doty SB (1989) Bone mechanics. Boca Raton. pp 242, 248

Cowin SC, Gailani G, Benalla M (2009) Hierarchical Poroelasticity: Movement of interstitial fluid between porosity levels in bones. Phil. Trans. R. Soc. 367: 3401–43

Cowin SC, Moss-Salentijn L, Moss ML (1991) Candidates for the mechanosensory system in bone. J. Biomech.Eng. 113:191–97

Dillaman RM, Roer RD, Gay DM. Fluid movement in bone: theoretical and empirical. J Biomech 1991;24(Suppl 1):163–77.

Fritton SP, Weinbaum S (2009) Fluid and solute transport in bone: Flow induced mechanotransduction. Annu. Rev. Fluid Mech. 41: 347–74

Fritton SP, Rubin CT (2001) In vivo measurement of bone deformations using strain gages. In Bone Mechanics Handbook, ed. SC Cowin, pp. 8.1–8.41. Boca Raton, FL: CRC

Gailani GB, Benalla M, Mahamud R, Cowin SC, Cardoso L (2009) Experimental Determination of the Permeability in the Lacunar-Canalicular Porosity of Bone. J. Biomech. Eng. 131: 1010071-7

Lanyon LE (1993) Osteocytes, strain detection, bone modeling and remodeling. Calcif Tissue Int. 53:S102–106. S106–107.

Remaggi F, Cane V, Palumbo C, Ferretti M (1998) Histomorphometric study on the osteocyte lacuno-canalicular network in animals of different species. I. Woven-fibered and parallel fibered bones. Italian Journal of Anatomy and Embryology 103: 145–155

Rubin CT, McLeod KJ, Bain SD (1990) Functional strains and cortical bone adaptation: epigenetic assurance of skeletal integrity. JBiomech. 23:43-54.

Turner CH, Pavalko FM (1998) Mechanotransduction and functional response of the skeleton to physical stress: the mechanisms and mechanics of bone adaptation. J Orthop Sci 3:346-355.

Vankan WJ, Huyghe JM, Janssen JD, Huson A (1996) Poroelasticity of saturated solids with an application to blood perfusion. Int. J. Engng Sci. 34,1019-3b

Vashishth D, Verborgt O, Divine G, Schaffler MB, and Fyhrie, D. P., 2000, ‘‘Decline in Osteocyte Lacunar Density in Human Cortical Bone Predicts the Accumulation of Microcracks With Age,’’ Bone, 26, pp. 375–380.

You L, Cowin SC, Schaffler MB,Weinbaum S (2001) A model for strain amplification in the actin cytoskeletonof osteocytes due to fluid drag on pericellular matrix. J. Biomech. 34:1375–86

Zhang D, Weinbaum S, Cowin SC (1998) Estimates of the peak pressures in the bone pore water. J. Biomech. Eng. 120: 697-703

Chapter 2

Bone poroelasticity

2.1. Introduction

Bone physiological loadings and their effects on the intrinsic functionality of the skeletal tissue represent one of the important fields in biomechanics. The doctrine of bone adaptation in response to mechanical environment was first illustrated by Wolff in 1892, which is known as Wolff's law. A simple way to portray the response of bone tissue to mechanical loading in terms of interstitial fluid flow can be developed by thinking about a fluid saturated spongy material. Under compression and extension the fluid will flow out of and into the material, respectively. The volume of the spongy material will also tend to increase if its exterior openings are sealed and the pore fluid is increased (Cowin and Doty 2007). The main ideas underlying the theory of bone poroelasticity are based on the difference in the pore fluid pressure between the vascular porosity, PV, and the lacunar canalicular porosity, PLC. This difference in the pore pressure causes the interstitial fluid movement that nourishes the bone cells and originates the transduction mechanism.

2.2. History of bone poroelasticity

The theory of poroelasticity was first applied in soil and geomechanics. It concerned different subjects such as consolidation problems, seismic wave propagation, and seabed mechanics. This theory was also established by Biot in several papers. In Biot (1941) the isotropic case was considered, and in Biot (1955) the theory is generalized to anisotropic materials. General solutions to the elastic equations were established in Biot (1956-a). The theory of wave propagation in such systems was examined in Biot (1956-b).

During the second half of the last century, the theory of poroelasticity has been applied successfully to the biomedical field. In the last 50 years poroelasticity has been used to determine

bone permeability by studying the confined and unconfined compression tests of a porous disc compressed between two parallel plates (Figure 2-1a and b).

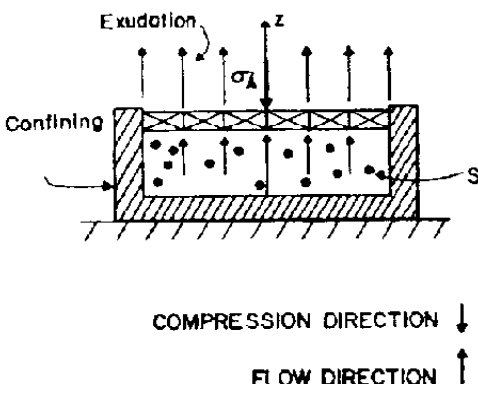

***Figure 2-1a**. Confined compression*

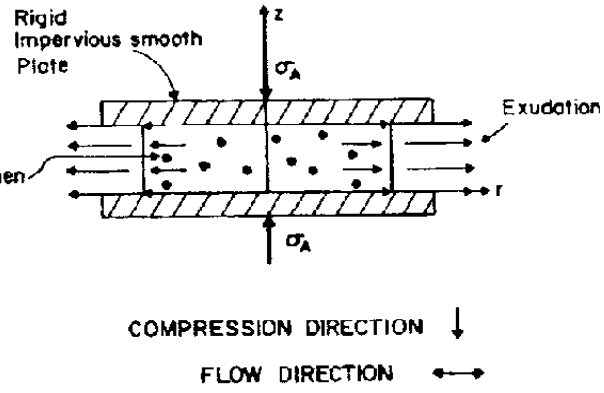

***Figure 2-1b**. Unconfined compression*

Cowin and Mehrabadi (2007) obtained a theoretical solution for the unconfined compression test of poroelastic material using the governing equations of the theory of anisotropic poroelastic materials without the constituent incompressibility constraint. The approach is applied to the unconfined compression of a circular porous disk and illustrated the effects of compressibility vs. incompressibility and transverse isotropy vs. isotropy. They also demonstrated the effects of changing the porosity on the load intensity and reported that the theoretical approach can be applied to hard materials like living bone tissues when incompressibility is not assumed. In Gailani et al. (2008), the work of Cowin and Mehrabadi (2007) was extended to annular disks subjected to stress relaxation test while in Cowin et al. (2009) and Benalla et al. (2012) the annular disk was subjected to a cyclic loading. The main objective behind all these studies was to accurately determine the PLC permeability and investigate the interaction of the pore pressure and fluid flow between the PV and the PLC.

2.3. Formulation of the poroelastic constitutive equations

The theory of poroelasticity in bone employs the same mechanical concepts as those applied to fluid-filled porous rock. There are three sets of poroelastic constitutive equations, the stress-strain-pore pressure, the fluid content-stress-pore pressure and Darcy's law.

2.3.1. Stress-strain-pore pressure relations

The displacement vector is denoted by **u** and second order tensor representation in 3D of the strain tensor is **E**. The strain-displacement relations in three dimensions are written in the form

$$\mathbf{E} = (1/2)((\nabla \otimes \mathbf{u})^{\mathrm{T}} + \nabla \otimes \mathbf{u}). \tag{1}$$

The symbol $\hat{\mathbf{E}}$ is used to represent the second order strain tensor **E** as a vector in 6D,

$$\hat{\mathbf{E}} = [\hat{E}_1, \hat{E}_2, \hat{E}_3, \hat{E}_4, \hat{E}_5, \hat{E}_6]^T = [E_{11}, E_{22}, E_{33}, \sqrt{2}E_{23}, \sqrt{2}E_{13}, \sqrt{2}E_{12}]^T .$$

The stress-strain-pore pressure constitutive relation for a saturated porous medium is that the strain $\hat{\mathbf{E}}$ in the saturated porous medium is linearly related, not only to the stress $\hat{\mathbf{T}}$, but also to the fluid pressure p in the fluid-filled pores, thus one can write the stain-stress-pore pressure relation

$$\hat{\mathbf{E}} = \hat{\mathbf{S}}^d \cdot \hat{\mathbf{T}} + \hat{\mathbf{S}}^d \cdot \hat{\mathbf{A}} p \,, \tag{2}$$

or the stress-pore pressure- strain relation

$$\hat{\mathbf{T}} + \hat{\mathbf{A}} p = \hat{\mathbf{C}}^d \cdot \hat{\mathbf{E}} \,, \tag{3}$$

where $\hat{\mathbf{S}}^d$ represents the drained anisotropic compliance elastic constants of the saturated porous medium and $\hat{\mathbf{C}}^d$ is its reciprocal, the drained anisotropic elasticity tensor. They are called the drained elastic constants because they are measured in situations in which the fluid pressure *p* in the fluid-filled pores is negligible or zero. Draining all the pores before the test or doing the test so slowly causes the pores to drain from a negligible fluid pressure. In a porous medium the pores are assumed to be connected; there are no unconnected pores that prevent the flow of fluid through them. The six-dimensional vector $\hat{\mathbf{A}}$ (three-dimensional symmetric second rank tensor **A**), introduced by (2), is called the *Biot effective stress coefficient vector* (6D) or *tensor* (3D) at the porosity level P. The Biot effective stress coefficient vector $\hat{\mathbf{A}}$ is related to the difference between effective drained elastic constants $\hat{\mathbf{S}}^d$ and the elastic compliance tensor of the matrix material, $\hat{\mathbf{S}}^m$, by the formula (Nur and Byerlee, 1971; Carroll, 1979; Cowin and Mehrabadi, 2007; Cowin and Doty, 2007)

$$\hat{\mathbf{A}} = (\hat{\mathbf{I}} - \hat{\mathbf{C}}^d \cdot \hat{\mathbf{S}}^m) \cdot \hat{\mathbf{U}} . \tag{4}$$

The Biot effective stress coefficient vector $\hat{\mathbf{A}}$ is so named because it is employed in the definition of the *effective stress* $\hat{\mathbf{T}}^{eff}$:

$$\hat{\mathbf{T}}^{eff} = \hat{\mathbf{T}} + \hat{\mathbf{A}} p . \tag{5}$$

This definition of effective stress reduces the stress-strain-pressure relation (2) to the same form as Hooke's law, thus

$$\hat{\mathbf{E}} = \hat{\mathbf{S}}^d \cdot \hat{\mathbf{T}}^{eff} . \tag{6}$$

This constitutive equation is a modification of Hooke's law to include the effect of the pore pressure. When $p = 0$ the stress-strain-pore pressure relations (2) and (3) or (5) and (6) coincide with anisotropic Hooke's law. The advantage of the representation (6) is that the fluid-saturated porous material may be thought of as an ordinary elastic material with a compliance matrix $\hat{\mathbf{S}}^d$, but one subjected to the "effective stress" $\hat{\mathbf{T}}^{eff}$ rather than (ordinary) stress $\hat{\mathbf{T}}$. The drained elastic compliance tensor $\hat{\mathbf{S}}^d$ may be evaluated from knowledge of the pore structure of the medium and the elastic compliance tensor $\hat{\mathbf{S}}^m$, or vice versa, using composite or effective medium theory. In case of orthotropic symmetry the drained compliance matrix $\hat{\mathbf{S}}^d$ has the representation

$$\hat{\mathbf{S}}^{\mathbf{d}} = \begin{bmatrix} \frac{1}{E_1^d} & \frac{-\nu_{21}^d}{E_2^d} & \frac{-\nu_{31}^d}{E_3^d} & 0 & 0 & 0 \\ \frac{-\nu_{12}^d}{E_1^d} & \frac{1}{E_2^d} & \frac{-\nu_{32}^d}{E_3^d} & 0 & 0 & 0 \\ \frac{-\nu_{13}^d}{E_1^d} & \frac{-\nu_{23}^d}{E_2^d} & \frac{1}{E_3^d} & 0 & 0 & 0 \\ 0 & 0 & 0 & \frac{1}{2G_{23}^d} & 0 & 0 \\ 0 & 0 & 0 & 0 & \frac{1}{2G_{13}^d} & 0 \\ 0 & 0 & 0 & 0 & 0 & \frac{1}{2G_{12}^d} \end{bmatrix} \tag{6a}$$

2.3.2 Fluid content-stress-pore pressure relations

The fluid content-stress-pore pressure constitutive relation involves all the basic field variables for poroelasticity, the total stress $\hat{\mathbf{T}}$, the pore pressure p, the strain in the solid matrix $\hat{\mathbf{E}}$, and the variation in (dimensionless) fluid content ζ. The variation in fluid content ζ is the

variation of the fluid volume per unit volume of the porous material due to diffusive fluid mass transport; it is defined as the difference between the strain of the pore space and the strain of the fluid volume in the pore space. The variation in fluid content ζ is equal to the product of the porosity ϕ and the fluid density ρ_f, divided by a reference value of the fluid density ρ_{fo}, thus $\zeta = \phi\rho_f / \rho_{fo}$. The variation in fluid content ζ depends not only upon the strain $\hat{\mathbf{E}}$ in the solid matrix, but also upon the strain induced by the pore pressure *p*, thus

$$\zeta = \hat{\mathbf{A}} \cdot \hat{\mathbf{E}} + \Lambda p \,, \tag{7}$$

where

$$\Lambda = \hat{\mathbf{U}} \cdot \hat{\mathbf{S}} \cdot \hat{\mathbf{A}} + \phi(\frac{1}{K^f} - \frac{1}{K^m_{Reff}}), \tag{8}$$

and where ϕ is the porosity, K^f is the bulk modulus of the fluid and K^m_{Reff} is the Reuss effective bulk modulus of an anisotropic elastic material (Cowin and Mehrabadi, 2007). In the case of isotropy this expression for Λ reduces to

$$\Lambda = \frac{1}{K^m_{Reff}}(1 - \frac{K^d_{Reff}}{K^m_{Reff}}) + \phi(\frac{1}{K^f} - \frac{1}{K^m_{Reff}}). \tag{9}$$

The variation in fluid content ζ is also linearly related to both the stress $\hat{\mathbf{T}}$ and the pore pressure *p*,

$$\zeta = \hat{\mathbf{A}} \cdot \hat{\mathbf{S}}^d \cdot \hat{\mathbf{T}} + C^d_{eff}\, p \tag{10}$$

where

$$C_{eff}^{d} = \frac{1}{K_{Reff}^{d}} - \frac{1}{K_{Reff}^{m}} + \phi\left(\frac{1}{K^{f}} - \frac{1}{K_{Reff}^{m}}\right). \tag{11}$$

The relation between C_{eff}^{d} and Λ is

$$C_{eff}^{d} = \Lambda - \hat{\mathbf{U}} \cdot \hat{\mathbf{S}}^{m} \cdot \hat{\mathbf{A}} + \left(\frac{1}{K_{Reff}^{d}} - \frac{1}{K_{Reff}^{m}}\right). \tag{12}$$

2.3.3 Darcy's law

The constitutive equations of poroelasticity developed thus far are the strain-stress-pore pressure relations (2) and the fluid content-stress-pore pressure relation (7). The other constitutive relation of poroelasticity is Darcy's law that relates the fluid mass flow rate, $\rho_f\mathbf{v}$, to the gradient (∇p) of the pore pressure p (Darcy, 1856),

$$\rho_f\mathbf{v} = -\,\mathbf{H}\nabla p\ (\mathbf{x}, t),\ \mathbf{H} = (\mathbf{H})^{T}. \tag{13}$$

The coefficient tensor **H** in Darcy's law may be represented by $\mathbf{H} = \rho_{fo}\,\mathbf{K}/\mu$ where **K** is the intrinsic Darcy's law permeability tensor, ρ_{fo} is a reference value of the fluid density and μ is the fluid viscosity. The intrinsic permeability tensor **K** has units of length squared and is a function of the porous structure only, not the fluid in the pores; thus Darcy's law (13) takes the form

$$\mathbf{q} = (\phi\rho_f/\rho_{fo})\mathbf{v} = -\,(1/\mu)\mathbf{K}\cdot\nabla p(\mathbf{x}, t),\ \mathbf{K} = (\mathbf{K})^{T}, \tag{14}$$

where the mass flux **q** has the dimensions of velocity.

2.3.4 Mass and momentum conservation

The conservation of mass in the form expressed by the equation of continuity is

$$\frac{\partial \rho}{\partial t} + \nabla \cdot (\rho \mathbf{v}) = 0 . \tag{15}$$

The form of the mass conservation equation (15) is altered to apply to the pore fluid volume by first replacing ρ by $\phi \rho_f$ in (15) and then dividing the equation through by ρ_{fo}, thus

$$\frac{1}{\rho_{fo}} \frac{\partial \phi \rho_f}{\partial t} + \frac{1}{\rho_{fo}} \nabla \cdot (\phi \rho_f \mathbf{v}) = 0 . \tag{16}$$

The form of (16) is changed by noting that the variation in fluid content ζ is given by $\zeta = \frac{\phi \rho_f}{\rho_{fo}}$ and the use of (14), thus

$$\frac{\partial \zeta}{\partial t} + \nabla \cdot \mathbf{q} = 0 . \tag{18}$$

The stress equations of motion in three dimensions,

$$\rho \ddot{\mathbf{u}} = \nabla \cdot \mathbf{T} + \rho \mathbf{b} , \ \mathbf{T} = \mathbf{T}^T , \tag{19}$$

have no simple representation in the 6D vector notation, and the conventional notation is employed; $\ddot{\mathbf{u}}$ represents the acceleration and **b** the body force.

2.3.5. Governing differential equations

There are many methods of approach to the solution of poroelastic problems for compressible media. The method selected depends upon the information that is provided and the fields that are to be calculated. One approach that has been effective is to solve for the variation in fluid content ζ if the stress or the strain field is known or may be calculated without reference

to the variation in fluid content ζ. The diffusion equation for the variation in volume fraction is obtained by first substituting Darcy's law (14) into the expression (18) for the conservation of mass and subsequently eliminating the pore pressure by use of (7), thus

$$\frac{\partial \zeta}{\partial t} - \frac{1}{\mu\Lambda}\hat{\mathbf{K}}\cdot\hat{\mathbf{O}}[\zeta] = -\frac{1}{\mu\Lambda}\hat{\mathbf{K}}\cdot\hat{\mathbf{O}}[\hat{\mathbf{A}}\cdot\hat{\mathbf{E}}]. \tag{20}$$

Where $\hat{\mathbf{O}}$ is the six-dimensional vector representation of the three-dimensional double gradient tensor defined by $O = \nabla\otimes\nabla\,(trO = \nabla^2)$. The components of $\hat{\mathbf{O}}$ are

$$\hat{\mathbf{O}} = \left[\frac{\partial^2}{\partial x_1^2}, \frac{\partial^2}{\partial x_2^2}, \frac{\partial^2}{\partial x_3^2}, \sqrt{2}\frac{\partial^2}{\partial x_2 \partial x_3}, \sqrt{2}\frac{\partial^2}{\partial x_1 \partial x_3}, \sqrt{2}\frac{\partial^2}{\partial x_1 \partial x_2}\right].$$

The difference to equation (20) shows that the time rate of change of the fluid content ζ is due either to fluid flux or to volume changes that are caused by the strain field. It is possible to replace the strain on the right hand side of (20) by stress in which case (20) becomes

$$\frac{\partial \zeta}{\partial t} - \frac{1}{\mu C_{eff}^{d}}\hat{\mathbf{K}}\cdot\hat{\mathbf{O}}[\zeta] = -\frac{1}{\mu C_{eff}^{d}}\hat{\mathbf{K}}\cdot\hat{\mathbf{O}}[\hat{\mathbf{A}}\cdot\hat{\mathbf{S}}^{\mathrm{d}}\cdot\hat{\mathbf{T}}], \tag{21}$$

where C_{eff}^{d} and Λ are related by (12).

Diffusion equations for the pressure field are also employed in the solution of poroelastic problems. The first diffusion equation for the pore pressure field is obtained by first substituting Darcy's law (14) into the expression (18) for the conservation of mass and subsequently eliminating the variation in fluid content ζ by use of (10), thus

$$\frac{\partial p}{\partial t} - \frac{1}{\mu\Lambda}\hat{\mathbf{K}}\cdot\hat{\mathbf{O}}[p] = -\frac{1}{\Lambda}\hat{\mathbf{A}}\cdot\frac{\partial\hat{\mathbf{E}}}{\partial t}. \tag{22}$$

The alternative diffusion equation for the pore pressure field is obtained by replacing the strain on the right hand side of (22) by stress, thus

$$\frac{\partial p}{\partial t} - \frac{1}{\mu C_{eff}^{d}} \hat{\mathbf{K}} \cdot \hat{\mathbf{O}}[p] = \frac{1}{C_{eff}^{d}} (\hat{\mathbf{U}} \cdot (\hat{\mathbf{S}}^{m} - \hat{\mathbf{S}}) \cdot \frac{\partial \hat{\mathbf{T}}}{\partial t}) . \tag{23}$$

The boundary conditions on the pore pressure field customarily employed in the solution of this differential equation are (i) that the external pore pressure *p* is specified at the boundary (a lower pressure permits flow across the boundary), (ii) that the pressure gradient ∇p at the boundary is specified (a zero pressure gradient permits no flow across the boundary), (iii) that some linear combination of (i) and (ii) is specified.

2.3.6. Poroelastic model of the lacunar-canalicular porosity level in bone tissue

The general formulation of the mathematical problem for compressible poroelastic hollow circular cylinders has been described earlier (Cowin and Mehrabadi, 2007; Gailani and Cowin 2008; Cowin et al. 2009). As earlier, transversely isotropic material symmetry is assumed. The displacement field components u_r, u_z, the pressure *p* and the variation in fluid content ζ are assumed to have the functional dependencies indicated below (Cowin and Mehrabadi, 2007, equation (47); Gailani and Cowin 2008, eqn (1); Cowin et al. 2009, eqn (24)):

$$u_r = u(r,t),\ u_z = z\varepsilon(t),\ p = p(r,t), \zeta = \zeta(r,t), \tag{24}$$

where $\varepsilon(t)$ is the applied axial loading that is $\varepsilon(t) = \varepsilon_o e^{i\omega t}$ in this case. Thus the key variables are taken to be *u(r, t), p(r, t)* and $\zeta(r, t)$ and the solutions are assumed to be of the form

$$u(r,t) = u(r)e^{i\omega t}\,,\; u_z(t) = z\varepsilon_o e^{i\omega t}\,,$$

$$p(r,t) = p(r)e^{i\omega t}\,, \zeta(r,t) = \zeta(r)e^{i\omega t}\,, \tag{25}$$

The non-zero stress components T_{rr}, $T_{\theta\theta}$ and T_{zz} are determined to be (Cowin and Mehrabadi, 2007, equation (60) and Gailani and Cowin 2008, equation (20))

The non-zero stress components are given in terms of the radial displacement $\tilde{u}(r,t)$ and the pore fluid pressure by Cowin et al., (2009), equation (5.3),

$$T_{rr} = -\hat{A}_r\,\tilde{p} + \hat{C}^d_{rr}\frac{\partial \tilde{u}}{\partial r} + \hat{C}^d_{r\theta}\frac{\tilde{u}}{r} + \hat{C}^d_{rz}\varepsilon_o e^{i\omega t}\,,\; T_{\theta\theta} = -\hat{A}_r\,\tilde{p} + \hat{C}^d_{r\theta}\frac{\partial \tilde{u}}{\partial r} + \hat{C}^d_{rr}\frac{\tilde{u}}{r} + \hat{C}^d_{rz}\varepsilon_o e^{i\omega t}\,,$$

$$T_{zz} = -\hat{A}_z\,\tilde{p} + \hat{C}^d_{rz}\left(\frac{\partial \tilde{u}}{\partial r} + \frac{\tilde{u}}{r}\right) + \hat{C}^d_{zz}\varepsilon_o e^{i\omega t}\,. \tag{26}$$

where the components of $\hat{\mathbf{C}}^d$ are the components of the drained elasticity tensor at the PLC porosity level and $\hat{\mathbf{A}}$ are those of the Biot effective stress coefficient vector. The only equation of equilibrium that is not satisfied automatically is (Cowin and Mehrabadi, 2007, equation (61); Gailani and Cowin 2008, equation (21))

$$\frac{\partial T_{rr}}{\partial r} + \frac{T_{rr} - T_{\theta\theta}}{r} = 0\,. \tag{27}$$

The relationship between $\tilde{u}(r,t)$ and $\tilde{p}(r,t)$ is obtained by substituting the expressions for T_{rr} and $T_{\theta\theta}$ given in (8a and b) into the stress equilibrium condition (9),

$$\frac{\partial \tilde{u}}{\partial r} + \frac{\tilde{u}}{r} = \frac{1}{\lambda}\frac{\partial}{\partial \lambda}(\lambda\tilde{u}) = \frac{\hat{A}_r}{\hat{C}^d_{rr}} r_o \tilde{p}(\lambda,t) + r_o f_o e^{i\omega t}\,, \tag{28}$$

where $f_o e^{i\omega t}$ is a function of time obtained in the integration with respect to r and $\hat{A}_r$ is the r component of the Biot effective stress coefficient. Since both the functions *u(r, t)* and *p (r, t)* in (25) are of the form of a product of a function of *r* times $e^{i\omega t}$ we assume that the function of time obtained in the integral has the representation $f_o e^{i\omega t}$**.** The expression (28) for $\frac{\partial u}{\partial r}+\frac{u}{r}=\frac{1}{r}\frac{\partial}{\partial r}(ru)$ may be used to calculate two expressions for the quantity $\hat{\mathbf{A}}\cdot\hat{\mathbf{E}}$,

$$\hat{\mathbf{A}}\cdot\hat{\mathbf{E}}=\hat{A}_r\left(\frac{\partial u}{\partial r}+\frac{u}{r}\right)+\hat{A}_z\varepsilon_o e^{i\omega t} \tag{29}$$

(Cowin and Mehrabadi, 2007, equation (59); Gailani and Cowin 2008, eqn (23)), one in terms of the variation in fluid content ζ and the other in terms of the pressure *p*. These expressions are needed in the diffusion equations (20) and (22) for ζ and *p*, respectively. To find $\hat{\mathbf{A}}\cdot\hat{\mathbf{E}}$ in terms of *p* substitute (28) in (29) to obtain

$$\hat{\mathbf{A}}\cdot\hat{\mathbf{E}}=\frac{\hat{A}_r\hat{A}_r}{\hat{C}^d_{rr}}\,p(r,t)+(\hat{A}_z\varepsilon_o+\hat{A}_r f_o)e^{i\omega t}, \tag{30}$$

and to find $\hat{\mathbf{A}}\cdot\hat{\mathbf{E}}$ in terms of ζ eliminate *p* in (30) using (7),

$$\hat{\mathbf{A}}\cdot\hat{\mathbf{E}}=\frac{1}{J}\{\hat{A}_r\hat{A}_r\zeta+\Lambda\hat{C}^d_{rr}[\hat{A}_z\varepsilon_o+\hat{A}_r f_o]e^{i\omega t}\}, \tag{31}$$

where the dimensionless quantity J is introduced,

$$J=\hat{A}_r\hat{A}_r+\Lambda\hat{C}^d_{rr}, \tag{32}$$

and where

$$\Lambda = C_{eff}^{d} - \frac{1}{K_{Reff}^{d}} + \frac{2}{K_{Reff}^{m}} - \frac{1}{9(1-\nu_{12}^{d}-2\nu_{13}^{d}\nu_{31}^{d})}[\frac{2E_{1}^{d}}{\left(K_{1}^{m}\right)^{2}} + \frac{4E_{1}^{d}\nu_{31}^{d}}{K_{1}^{m}K_{3}^{m}} + \frac{E_{3}^{d}(1-\nu_{12}^{d})}{\left(K_{3}^{m}\right)^{2}}], \tag{33}$$

and

$$C_{eff}^{d} = \frac{1}{K_{Reff}^{d}} - \frac{1}{K_{Reff}^{m}} + \phi(\frac{1}{K^{f}} - \frac{1}{K_{Reff}^{m}}), \tag{34}$$

which are equations (58) and (19C), respectively, in Cowin and Mehrabadi (2007). In the equations above the kernel letter *K* stands for a bulk modulus, the superscripts *d* and *f* indicate drained material and the fluid, respectively, *m* indicates the matrix material and the subscript *Reff* indicates the effective Reuss lower bound on the indicated bulk moduli (Cowin and Mehrabadi, 2007). In the compressible, transversely anisotropic case, the expression for *J* is given by (Cowin and Mehrabadi, 2007, equation (57)),

$$J = [1 - \frac{E_{1}^{d}}{3(1-\nu_{12}^{d}-2\nu_{31}^{d}\nu_{13}^{d})}(\frac{1}{K_{1}^{m}} + \frac{\nu_{31}^{d}}{K_{3}^{m}})]^{2} + \Lambda\frac{E_{1}^{d}(1-\nu_{13}^{d}\nu_{31}^{d})}{(1+\nu_{12}^{d})(1-\nu_{12}^{d}-2\nu_{31}^{d}\nu_{13}^{d})}. \tag{35}$$

The diffusive differential equation for the pore pressure is obtained by substituting (30) and $\hat{\mathbf{K}}\cdot\hat{\mathbf{O}} = K_{rr}(\frac{\partial^{2}}{\partial r^{2}} + \frac{1}{r}\frac{\partial}{\partial r})$ into (22) above, neglecting the flux terms from the other porosity levels, thus

$$\frac{\partial p}{\partial t} - \frac{K_{rr}}{\mu\Lambda}(\frac{\partial^{2} p}{\partial r^{2}} + \frac{1}{r}\frac{\partial p}{\partial r}) = -\frac{1}{\Lambda}\frac{\hat{A}_{r}\hat{A}_{r}}{\hat{C}_{rr}^{d}}\frac{\partial p}{\partial t} - \frac{i\omega}{\Lambda}(\hat{A}_{z}\varepsilon_{o} + \hat{A}_{r}f_{o})e^{i\omega t}, \tag{36}$$

or, rearranging terms,

$$\frac{\partial^{2} p}{\partial r^{2}} + \frac{1}{r}\frac{\partial p}{\partial r} - \frac{\mu}{K_{rr}}(\Lambda + \frac{\hat{A}_{r}\hat{A}_{r}}{\hat{C}_{rr}^{d}})\frac{\partial p}{\partial t} = \frac{i\omega\mu}{K_{rr}}(\hat{A}_{z}\varepsilon_{o} + \hat{A}_{r}f_{o})e^{i\omega t}, \tag{37}$$

and introducing the notation

$$\frac{1}{c}=\frac{\mu}{K_{rr}}(\Lambda+\frac{\hat{A}_r\hat{A}_r}{\hat{C}^d_{rr}})=\frac{\mu J}{K_{rr}\hat{C}^d_{rr}} \tag{38}$$

where (32) has been employed, it follows that

$$\frac{\partial^2 p}{\partial r^2}+\frac{1}{r}\frac{\partial p}{\partial r}-\frac{1}{c}\frac{\partial p}{\partial t}=\frac{i\omega\mu}{K_{rr}}(\hat{A}_z\varepsilon_o+\hat{A}_r f_o)e^{i\omega t}\,. \tag{39}$$

The equation (39) is the differential equation for the pore pressure that has an inhomogeneous part. In Cowin and Mehrabadi (2007) they formulated the differential equation for the variation in fluid content in that had a homogeneous form,

$$\frac{\partial^2\zeta}{\partial r^2}+\frac{1}{r}\frac{\partial\zeta}{\partial r}-\frac{1}{c}\frac{\partial\zeta}{\partial t}=0\,. \tag{40}$$

Based on equation (77) in Cowin and Mehrabadi (2007) the pore pressure can expressed with respect to the variation in fluid content

$$p(r,t)=\frac{\hat{C}^d_{rr}}{J}[\zeta(r,t)-\hat{A}_z\varepsilon(t)-\hat{A}_r f(t)], \tag{41}$$

Thus instead of solving both *p(r, t)* and *ζ(r,t)* one can solve only (40) for the variation in fluid content and then determine the pore pressure using equation (41).

References

Benalla M, Cardoso L, Cowin SC (2012) Analytical basis of the lacunar-canalicular permeability of bone using cyclic loading. Biomech. Model. Mechanobiol. Accepted: 14 September 2011.

Biot MA (1941) General theory of three-dimensional consolidation. J. Appl. Phys. 12, 155-164.

Biot MA (1955) Theory of elasticity and consolidation for a porous anisotropic solid. J. Appl. Phys. 26: 182-182.

Biot MA (1956-a) General solution of the equations of elasticity and consolidation for a porous material. J. of Applied Mechanics, Trans. ASME, v78, pp. 91-96

Biot MA (1956-b) Theory of propagation of elastic waves in a fluid saturated porous solid, parts I and II. J. of the Acoustical Society of America, v28, pp. 168-91

Carroll MM (1979) An Effective Stress Law for Anisotropic Elastic Deformation, *J. Geophys. Res.* 84:7510-7512.

Cowin SC, Gailani G, Benalla M (2009) Hierarchical Poroelasticity: Movement of interstitial fluid between porosity levels in bones. Phil. Trans. R. Soc. 367: 3401–43

Cowin SC, Mehrabadi MM (2007) Compressible and incompressible constituents in anisotropic poroelasticity: The problem of unconfined compression of a disk. *J. Mech. Phys. Solids.* ***55****:*161-193.

Cowin SC, Doty SB (2007) *Tissue Mechanics*. Springer

Darcy H (1856) *Les Fontains Publiques de la Ville de Dijon*, Dalmont: Paris.

Gailani GB, Cowin SC (2008) The unconfined compression of a poroelastic annular cylindrical disk. *Mechanics of Materials* 40:507-523.

Gailani GB, Benalla M, Mahamud R, Cowin SC, Cardoso L (2009) Experimental Determination of the Permeability in the Lacunar-Canalicular Porosity of Bone. J. Biomech. Eng. 131: 1010071-7

Nur A, Byerlee JD (1971) An exact effective stress law for elastic deformation of rock with fluids. *J. Geophys. Res.* **76**:6414.

Chapter 3

Analytical Basis for the Determination of the Lacunar-Canalicular Permeability of Bone Using Cyclic Loading

Accepted in BMMB journal

Abstract.

An analytical model for the determination of the permeability in the lacunar-canalicular porosity of bone using cyclic loading is described in this contribution. The objective of the analysis presented is to relate the lacunar-canalicular permeability to a particular phase angle that is measurable when the bone is subjected to infinitesimal cyclic strain. The phase angle of interest is the lag angle between the applied strain and the resultant stress. Cyclic strain causes the interstitial fluid to move. This movement is essential for the viability of osteocytes and is believed to play a major role in the bone mechanotransduction mechanism. However, certain bone fluid flow properties, notably the permeability of the lacunar-canalicular porosity, are still not accurately determined. In this paper, formulas for the phase angle as a function of permeability for infinitesimal cyclic strain are presented and mathematical expressions for the storage modulus, loss modulus, and loss tangent are obtained. An accurate determination of the PLC permeability will improve our ability to understand mechanotransduction and mechanosensory mechanisms, which are fundamental to the understanding of how to treat osteoporosis, how to cope with microgravity in long term manned space flights and how to increase the longevity of prostheses that are implanted in bone tissue.

Key Terms*: Poroelasticity, osteon permeability, phase angle, storage modulus, loss modulus, loss tangent.*

3.1. Introduction

During the last decade, an increasing amount of evidence has supported the hypothesis that osteocytes, the bone cells in the lacunae (pores) of the lacunar–canalicular porosity (PLC) are the principal mechanosensory cells of bone (Burger et al., 1995; Cowin et al., 1991; Han et al., 2004), and that they are activated by the induced drag from fluid flowing through the PLC (Cowin et al., 1995; Fritton and Weinbaum 2009; Weinbaum et al., 1994). The movement of bone fluid from the region of the bone vasculature through the canaliculi and the lacunae of the surrounding mineralized tissue is related to the poroelastic aspect of the loaded bone (Fritton et al., 2001; Remond et al., 2008; Wang et al., 2003) that exhibits creep, stress relaxation and a phase or lag angle between an applied cyclic strain and the resultant stress (Buechner et al., 2003; Cowin 1999, 2001; Lakes 1982; Nguyen et al., 2009; Swan et al., 2003).

The deformation driven fluid movement in the bone tissue accomplishes three important tasks. First, it transports nutrients to the cells in the lacunae buried in the mineralized matrix. Second, it carries away the cell waste. Third, the deformation-driven interstitial fluid movement in the PLC exerts a force on the osteocyte process, a force that is large enough for the cell to sense, which is considered as the basic mechanotransduction mechanism in bone cells in vivo.

Key to the understanding of mechanotransduction by osteocytes is knowledge of the lacunar-canalicular network permeability. An estimate of the PLC permeability was first proposed by Zeng et al., (1994) based on an ultrastructural model of the lacunar-canalicular system, predicting PLC permeability on the order of 10^{-20} to 10^{-22} m^2. Subsequent, theoretical estimates were based on Biot's poroelasticity theory, including the study by Wang et al., (1999)

Reference	Method	Permeability at the PLC
Kameo et al., (2010)	Morphology of the PLC	$3.32\ 10^{-17}$ - $1.26\ 10^{-18}$ m^2
Wang et al., (1999)	Theoretical study	$1.47\ 10^{-20}$ m^2
Smit et al., (2002)	Finite element analysis	$2.20\ 10^{-22}$ m^2
Beno et al., (2006)	Biot theory	$3.32\ 10^{-19}$ - $1.26\ 10^{-22}$ m^2
Zeng et al., (1994)	Ultrastructural model	10^{-19} - 10^{-22} m^2
Gururaja et al., (2005)	Poroelasticity model	10^{-19} - 10^{-22} m^2
Zhou et al., (2008)	FRAP	10^{-22} m^2
Gardinier et al., (2010)	Step loading experiment	$2.80\ 10^{-23}$ m^2
Oyen et al., (2008)	Nanoindentation	$4.14\ 10^{-24}$ m^2
Gailani et al., (2009)	Stress relaxation	$3.00\ 10^{-24}$ - $7.00\ 10^{-25}$ m^2

Table 3-1. *Values of the PLC permeability collected from different studies. The values are ranging from 3.32 10^{-17} m^2 to 7.00 10^{-25} m^2.*

in which the PLC of bovine bone was found in the range of 10^{-20} m^2, the approach by Gururaja et al., (2005) who obtained an estimate of the PLC permeability in both directions, the radial and circumferential, to be 10^{-22} and 10^{-19} m^2 respectively, and the study by Zhou et al., (2008) in mice, with a PLC permeability on the order of 10^{-22} m^2. Traditional permeability measurement techniques based on Darcy's technique of measuring the volume of fluid flow per unit area and per unit time across a porous layer, which is then divided by the pore pressure gradient across the layer, seem to be experimentally unfeasible. Therefore, other approaches have been developed to determine the PLC permeability. Smit et al., (2002) obtained an estimate of the PLC permeability on the order of 10^{-22} m^2 based on the best fit between finite element predictions and data from streaming potential measurements. Beno et al., (2006) found the PLC permeability in

canine bone to vary from 10^{-19} m^2 to 10^{-22} m^2. The PLC permeability of human bone was estimated by Oyen (2008) to be around 10^{-24} m^2 using nanoindentation measurements and poroelasticity theory. Curve fitting of stress-relaxation of single bovine osteons and poroelasticity theory was used by Gailani et al., (2009), finding the PLC permeability to be between 10^{-24} and 10^{-25} m^2. An estimate of the PLC permeability was provided by Kameo et al., (2010) based on measurements of fluorescent images taken with a laser confocal microscope in trabecular bone from a swine tibia and an anisotropic poroelastic analytical model, resulting in predictions of the PLC permeability on the order of 10^{-17} m^2. In their discussion Kameo et al., (2010) described difficulties with their confocal laser scanning microscopy. Only recently, the canine PLC was measured in situ by Gardinier et al., (2010), and reported as $10^{-23}m^2$ (Table 3-1).

These estimates of PLC permeability exhibit a broad variability, with values ranging from 10^{-17} to 10^{-25} m^2 (Table 3-1). Such broad range of variability may be due to the different approach/model taken to determine the PLC permeability and/or by experimental challenges associated with the measurement of small quantities as in the case of Kameo et al., (2010). Importantly, the PV and the PLC are interconnected, occupying the same three-dimensional volume of bone tissue. Thus, the pore pressure in the PLC depends upon the permeability of the PV and vice versa. In order to investigate the interaction of the pore pressure and fluid flow between the PV and the PLC, a hierarchical poroelastic model was recently developed by our group (Cowin et al., 2009). On one hand, it is difficult to measure the PV permeability without the effect of the PLC since the PLC is always contained in the tissue matrix material of samples used to measure the PV. On the other hand, the PLC permeability can be measured without the effect of the PV if a sample that contains PLC only is obtained. For this purpose, the analytical solution of a saturated compressible poroelastic annular cylinder under an unconfined stress-

relaxation test was developed (Gailani and Cowin, 2008). Predictions made by this model were compared to experimental stress-relaxation measurements made on isolated osteons in vitro (zero blood pressure), and the curve fitting between data and experiments was used to obtain the PLC permeability without the influence of the PV (Gailani et al., 2009).

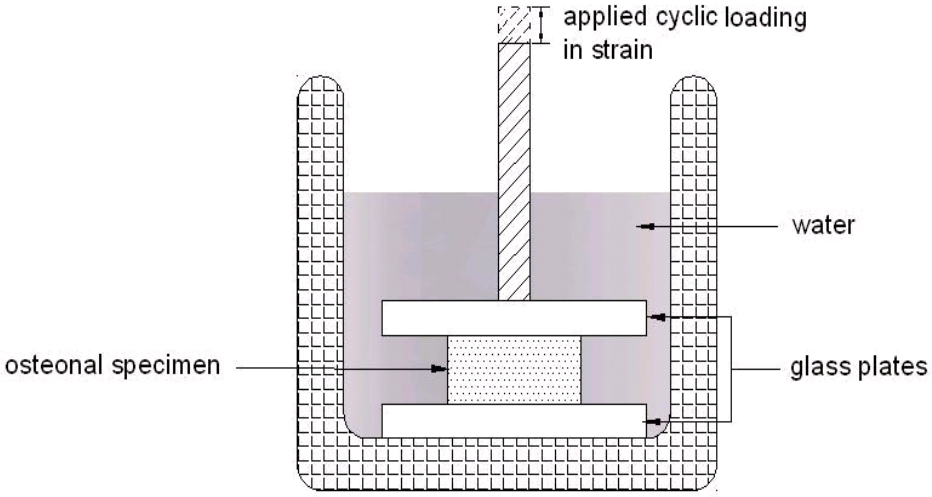

Figure 3.1. *Single osteon specimen immersed in water and subjected to unconfined cyclic loading. The specimen is compressed between rigid plates that are parallel, smooth, and impermeable. The interstitial fluid is forced to flow out of the PLC in the radial direction across the inner boundary of the annular region into the Haversian canal. No fluid flow is produced at the outer boundary since the cement line is assumed to be impermeable.*

In this paper, the solution presented in Cowin et al., (2009) and the experimental approach developed in Gailani et al., (2009) are extended to the case of harmonic loading (Figure 3-1). A description of the osteon's anatomy and physiology is presented in §2. A single osteon is idealized as a fully saturated porous annular cylinder subjected to an axial cyclic mechanical loading in order to determine formulas for the phase angle as a function of permeability and

frequency in §3. The phase angle of interest corresponds to the difference between the applied cyclic strain and the resultant stress. Also, expressions for the storage modulus, the loss modulus, and the loss tangent are obtained in §3. Numerical examples are presented in section §4, the sensitivity of the analytical model to the variation in the model parameters is considered in section §5 and a discussion of the results are in section §6. The analytical model of this paper will be used as a basis of a future experimental study in which an isolated osteonal specimen will be subjected to an applied cyclic strain in order to determine the phase angle between the applied cyclic strain and the resultant stress, and thus evaluate the frequency dependence of the PLC permeability experimentally.

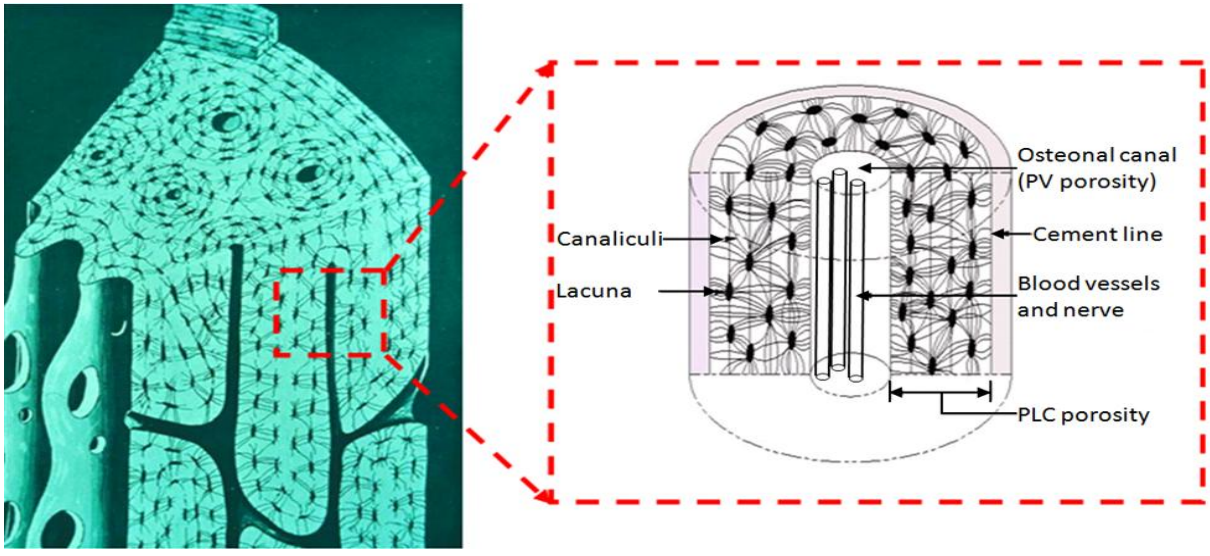

Figure 3-2. *A cartoon depicting how the cut of the osteonal cylindrical specimen should be performed in order to estimate the PLC permeability free of the influence of the PV.*

3.2. The anatomy and physiology of an osteon

The osteon is a fundamental building unit of adult human long bones at the microscopic scale. The osteon geometry is roughly cylindrical with a radius of about 100 -150 μm and it contains at its center a Haversian or osteonal canal of about 40 μm radii (Figure 3-2). It is composed of two phases, liquid and solid. The fluid phase is an interstitial liquid that surrounds blood vessels in the Haversian canal and fills all the pores in the PLC; it functions as an interchange path between the two porosities. The fluid movement depends upon the applied loading and the difference of pore pressure between the two chambers, the PLC and the central Haversian canal. The interchange occurs in two different directions, (i) transport of nutrients and oxygen from arterioles to the bone cells into the PLC and (ii) transfer of the cell waste from the lacunae to the venules in the central Haversian canal, part of vascular porosity (PV). The osteonal solid phase formation unit is a lamella 3 to 7 μm thick composed of mineralized collagen fibers oriented parallel to one another. The small regularly placed cavities observed in between lamellae are lacunae, in which osteocytes (bone cells) reside. Lacunae are connected by small canals (approximately 0.3 μm in diameter) called canaliculi. Each canaliculum contains an osteocyte cell process and these processes are connected with each other by gap junctions. The canaliculi also join the lacunae with the Haversian canal (Figure 3-2). At the outer border of each osteon are roughly 2 μm thick cement lines comprised of a mineralized matrix (Jee 1988). The annular region of the approximately cylindrical osteon is entirely composed of the PLC and the cement line. The Haversian or osteonal canal is part of the PV and has a diameter of roughly 40 μm. The osteonal canal is considered as PV because of its size and the fact that it houses vasculature and nerves as well. Beyond the fact that the PLC houses osteocytes in the lacunae, it represents all the fluid-occupied space in an osteon. In terms of movement and velocity, the

interstitial fluid behaves differently under a cyclic mechanical loading in the PLC from its behavior in the Haversian canal. The difference of the bone fluid behavior stems from the differences in geometry and the intrinsic characteristic of each domain (Fornells et al., 2007). On one hand the Haversian canal is the large-scale porosity with roughly ten orders of magnitude greater permeability (Gardinier et al., 2010) that houses blood vessels and in which pressure pulses will decay rapidly. Any significant increase of pressure in response to mechanical loading beyond blood pressure in this porosity could collapse the vessels, which will render the bone tissue ischemic if the collapse is prolonged (Cowin et al., 2009); in other words, this means that the PV remains most of the time under a lower pressure. However, on other hand, the PLC is the porosity associated with the higher pressure compared to the PV as well as longer relaxation time for pressure pulses (Yang et al., 1999; Zhang et al., 1998). Moreover, the PLC has a much lower permeability and contains osteocytes, the bone sensory cells, with their interconnected processes. The difference of pressures created between the PLC and the PV causes the fluid movement that creates forces large enough to be sensed by osteocytes. These forces are thought to activate the molecular sensor structures that are part of the mechanosensory phenomena. The whole process allows the osteocytes to orchestrate the bone resorption and manage the bone remodeling. Therefore, one can see how the determination of the PLC permeability represents a major key to improve the understanding of mechanotransduction phenomena.

3.3. Phase angle as a function of permeability

We consider a transverse segment of an isolated osteonal specimen whose annular region (PLC) between the Haversian canal and cement line is subjected to an axial cyclic loading between two

smooth, parallel and impermeable plates (Figure 3-1 and 3-2). The contact between the specimen and the plates is assumed to be frictionless and the applied load is considered to be uniformly distributed on the loaded surface. The axial cyclic loading is in the form of an applied strain, $\varepsilon_o e^{i\omega t}$, where ε_o and ω are the amplitude of the cyclic strain and its angular frequency, respectively. Axial symmetry is assumed and cylindrical coordinates are employed to represent the specimen, *r* is the radial coordinate and *z* is the axial coordinate. The displacement in the radial direction is then denoted by $\tilde{u}(r,t)$ where *t* is time. These displacement components, in addition to the pore pressure field $\tilde{p}(r,t)$ and the variation in fluid content $\tilde{\zeta}(r,t)$ a dimensionless measure of the fluid mass per unit volume of the porous material, are assumed to have the following temporal dependencies when subjected to the applied axial loading $\varepsilon(t) = \varepsilon_o e^{i\omega t}$:

$$\tilde{u}(r,t) = z\varepsilon(t),\ \tilde{p}(r,t) = p(r)e^{i\omega t},\ \tilde{\zeta}(r,t) = \zeta(r)e^{i\omega t}. \qquad (1)$$

The differential equation governing the pore pressure field is specialized from Cowin et al., (2009), equation (5.16), as

$$\frac{\partial^2 \tilde{p}}{\partial r^2} + \frac{1}{r}\frac{\partial \tilde{p}}{\partial r} - \frac{\mu}{K_{rr}}\left(\frac{\hat{A}_r^2}{\hat{C}_{rr}^d} + \Lambda\right)\frac{\partial \tilde{p}}{\partial t} = i\omega\frac{\mu}{K_{rr}}\left(\hat{A}_z\varepsilon_o + \hat{A}_r f_o\right)e^{i\omega t}. \qquad (2)$$

The notations in equation (2) that were not introduced above include the expressions for the radial elastic constant $\hat{C}_{rr}^d$, the radial intrinsic permeability K_{rr}, the coefficient Λ describing the contrast between the compliance of the solid tissue matrix material and the pore fluid, and the two components of the 6D vector representing the Biot effective stress coefficients $\hat{A}_z$ and $\hat{A}_r$.

Formulas / Constants	Transverse isotropy compressible
$\frac{1}{K_r^m}$	$\frac{1-\nu_{r\theta}^m-\nu_{rz}^m}{E_r^m}$
$\frac{1}{K_z^m}$	$\frac{1-2\nu_{rz}^m}{E_z^m}$
$\frac{1}{K_{\text{Reff}}^m}$	$\frac{2}{K_r^m}+\frac{1}{K_z^m}$
Δ_1	$1-\nu_{r\theta}^d-2\nu_{rz}^d\nu_{zr}^d$
Δ_2	$(1-\nu_{rz}^d\nu_{zr}^d)/(1+\nu_{r\theta}^d)$
Δ_3	$(1-2\nu_{zr}^d)\Delta_2/\Delta_1$
$\frac{1}{K_{\text{Reff}}^d}$	$\frac{2(1-\nu_{r\theta}^d-\nu_{rz}^d)}{E_r^d}+\frac{1-2\nu_{zr}^d}{E_z^d}$
C_{eff}^d	$\frac{1}{K_{\text{Reff}}^d}-\frac{1}{K_{\text{Reff}}^m}+\phi(\frac{1}{K^f}-\frac{1}{K_{\text{Reff}}^m})$
Λ	$C_{eff}^d-\frac{1}{K_{\text{Reff}}^d}+\frac{2}{K_{\text{Reff}}^m}-\frac{1}{\Delta_1}\left[\frac{2E_r^d}{K_r^{m^2}}+\frac{4E_r^d\nu_{zr}^d}{K_r^mK_z^m}+\frac{E_z^d(1-\nu_{r\theta}^d)}{K_z^{m^2}}\right]$
J	$\left[1-\frac{E_r^d}{\Delta_1}(\frac{1}{K_r^m}+\frac{\nu_{zr}^d}{K_z^m})\right]^2+\Lambda\frac{E_r^d\Delta_2}{\Delta_1}$
$\hat{A}_r$	$1-\frac{E_r^d}{\Delta_1}(\frac{1}{K_r^m}+\frac{\nu_{zr}^d}{K_z^m})$
$\hat{A}_z$	$1-\frac{E_z}{\Delta_1}(\frac{2\nu_{rz}^d}{K_r^m}+\frac{1-\nu_{r\theta}^d}{K_z^m})$
$\hat{C}_{rr}^d$	$\frac{\Delta_2}{\Delta_1}E_r^d$
$\hat{C}_{zz}^d$	$\frac{(1-\nu_{r\theta}^d)}{\Delta_1}E_z^d$
$\hat{C}_{r\theta}^d$	$\frac{1-\Delta_2}{\Delta_1}E_r^d$
$\hat{C}_{rz}^d$	$\frac{\nu_{rz}}{\Delta_1}E_z^d$
c	$\frac{K_{rr}C_{rr}^d}{\mu J}$

Table 3-2*.Relationships between model parameters employed.*

These symbols are introduced in the nomenclature and their formulas are provided in Table 3-2. f_o is a constant of integration to be determined. Equation (2) may be written more conveniently by introducing the dimensionless driving frequency constant $\bar{\omega}$ and a constant of dimension force Υ as

$$\bar{\omega} = \frac{\omega r_o^2}{c}, \Upsilon = \mu \hat{A}_r c, \tag{3}$$

where c is the pore fluid diffusion constant in the PLC (Table 3-2), the dimensionless radius $\lambda = r/r_o$, noting that r_o corresponds to the outer radius of the osteon: equation (2) then takes the form

$$\frac{\partial^2 \tilde{p}}{\partial \lambda^2} + \frac{1}{\lambda}\frac{\partial \tilde{p}}{\partial \lambda} - i\bar{\omega}\tilde{p} = \frac{i\bar{\omega}\Upsilon}{K_{rr}}\left(\frac{\hat{A}_z}{\hat{A}_r}\varepsilon_o + f_o\right). \tag{4}$$

The fluid flow is only in the radial direction within the annular region of the osteon (the PLC) and the solution of this ODE requires thus only two boundary conditions, (i) at $\lambda = 1$, (the outer boundary of the osteon), it is considered that there is no flow crossing the cement line, and (ii) at $\lambda = a$, (the Haversian canal wall), where a is a non-dimensional inner radius of the osteon, there is a free fluid flow between the Haversian canal and the PLC, thus

$$\frac{\partial \tilde{p}}{\partial \lambda}(1,t) = 0, \ \tilde{p}(a,t) = 0. \tag{5}$$

The solution of the ODE (4) subjected to the boundary conditions (5) is

$$\tilde{p}(\lambda,t) = \left(\bar{\Pi}(\lambda,1) - 1\right)\left(\frac{A_z}{A_r}\varepsilon_o + f_o\right)\frac{\Upsilon}{K_{rr}}e^{i\omega t}, \tag{6}$$

where

$$\bar{\Pi}(\lambda,\alpha)=\frac{\Pi(\lambda,\alpha)}{\Pi(a,\alpha)} \tag{7a}$$

and

$$\Pi(\lambda,\alpha)=I_o(\sqrt{i\bar{\omega}}\lambda)K_1(\sqrt{i\bar{\omega}}\alpha)+I_1(\sqrt{i\bar{\omega}}\alpha)K_o(\sqrt{i\bar{\omega}}\lambda)]. \tag{7b}$$

Concerning the thought experiment associated with this model, no flow is permitted across the upper and bottom boundaries of the annular section of the osteon due to close contact with the impervious and frictionless loading plates. There also exists a free fluid exchange between the Haversian canal fluid and the fluid contacting the osteonal canal at the top and bottom of the specimen.

The non-zero stress components are given in terms of the radial displacement $\tilde{u}(r,t)$ and the pore fluid pressure by Cowin et al., (2009), equation (5.3),

$$T_{rr}=-\hat{A}_r\tilde{p}+\hat{C}^d_{rr}\frac{\partial\tilde{u}}{\partial r}+\hat{C}^d_{r\theta}\frac{\tilde{u}}{r}+\hat{C}^d_{rz}\varepsilon_o e^{i\omega t}, \tag{8a}$$

$$T_{\theta\theta}=-\hat{A}_r\tilde{p}+\hat{C}^d_{r\theta}\frac{\partial\tilde{u}}{\partial r}+\hat{C}^d_{rr}\frac{\tilde{u}}{r}+\hat{C}^d_{rz}\varepsilon_o e^{i\omega t}, \tag{8b}$$

$$T_{zz}=-\hat{A}_z\tilde{p}+\hat{C}^d_{rz}\left(\frac{\partial\tilde{u}}{\partial r}+\frac{\tilde{u}}{r}\right)+\hat{C}^d_{zz}\varepsilon_o e^{i\omega t}. \tag{8c}$$

The relationship between $\tilde{u}(r,t)$ and $\tilde{p}(r,t)$,

$$\frac{\partial\tilde{u}}{\partial r}+\frac{\tilde{u}}{r}=\frac{1}{\lambda}\frac{\partial}{\partial\lambda}(\lambda\tilde{u})=\frac{\hat{A}_r}{\hat{C}^d_{rr}}r_o\tilde{p}(\lambda,t)+r_o f_o e^{i\omega t}, \tag{9}$$

is obtained by substituting the expressions for T_{rr} and $T_{\theta\theta}$ given in (8a and b) into the stress equilibrium condition

$$\frac{\partial T_{rr}}{\partial r}+\frac{T_{rr}-T_{\theta\theta}}{r}=0, \tag{9a}$$

thus, the expression for $\tilde{u}(\lambda,t)$ is given by

$$\tilde{u}(\lambda,t)=\left[\frac{1}{2}+\left(\frac{\bar{\Sigma}(\lambda,1)}{\lambda}-\frac{1}{2}\right)\right]r_o\lambda f_o e^{i\omega t}+\frac{\lambda}{C^d_{rr}}\left(\frac{\bar{\Sigma}(\lambda,1)}{\lambda}-\frac{1}{2}\right)r_o A_z\varepsilon_o e^{i\omega t}+\frac{g_o}{\lambda}e^{i\omega t}, \tag{10}$$

where

$$\Sigma(\lambda,\alpha)=\frac{1}{\sqrt{i\bar{\omega}}}\frac{\partial\Pi(\lambda,\alpha)}{\partial\lambda},\ \int\lambda\Pi(\lambda,\alpha)d\lambda=\frac{\lambda\Sigma(\lambda,\alpha)}{\sqrt{i\bar{\omega}}},\ \bar{\Sigma}(\lambda,\alpha)=\frac{\Sigma(\lambda,\alpha)}{\Pi(\lambda,\alpha)}, \tag{11}$$

and g_o is a constant of integration obtained by solving equation (9). The substitution of equations (10) and (9) into the expression of T_{rr} in (8) yields to the desired formula for the radial stress,

$$T_{rr}=-\hat{A}_r\tilde{p}+\left\{\frac{\hat{C}^d_{r\theta}+\hat{C}^d_{rr}}{2}+\left[\bar{\Pi}(\lambda,1)-1+\frac{\hat{C}^d_{r\theta}-\hat{C}^d_{rr}}{\hat{C}^d_{rr}}\left(\frac{\bar{\Sigma}(\lambda,1)}{\lambda\sqrt{i\bar{\omega}}}-\frac{1}{2}\right)\right]\frac{\hat{A}_r\Upsilon}{K_{rr}}\right\}f_o e^{i\omega t}+$$

$$\left\{\hat{C}^d_{rz}+\left[\bar{\Pi}(\lambda,1)-1+\frac{\hat{C}^d_{r\theta}-\hat{C}^d_{rr}}{\hat{C}^d_{rr}}\left(\frac{\bar{\Sigma}(\lambda,1)}{\lambda\sqrt{i\bar{\omega}}}-\frac{1}{2}\right)\right]\frac{\hat{A}_z\Upsilon}{K_{rr}}\right\}\varepsilon_o e^{i\omega t}+\left(\hat{C}^d_{r\theta}-\hat{C}^d_{rr}\right)\frac{g_o}{r_o\lambda^2}e^{i\omega t} \tag{12}$$

Because of the free fluid flow at the inner surface of the hollow cylinder, both the radial stress and the pore fluid pressure vanish. At this boundary, $\lambda=a$ and the function $\bar{\Pi}(\lambda,1)$ in equation (7a) becomes $\bar{\Pi}(a,1)=1$, thus

$$T_{rr}(a,t)=0=\left\{\frac{\hat{C}^d_{r\theta}+\hat{C}^d_{rr}}{2}+\left[\frac{\hat{C}^d_{r\theta}-\hat{C}^d_{rr}}{\hat{C}^d_{rr}}\left(\frac{\bar{\Sigma}(a,1)}{a\sqrt{i\bar{\omega}}}-\frac{1}{2}\right)\right]\frac{\hat{A}_r\Upsilon}{K_{rr}}\right\}f_o e^{i\omega t}+$$

$$\left\{\hat{C}^d_{rz}+\left[\frac{\hat{C}^d_{r\theta}-\hat{C}^d_{rr}}{\hat{C}^d_{rr}}\left(\frac{\bar{\Sigma}(a,1)}{a\sqrt{i\bar{\omega}}}-\frac{1}{2}\right)\right]\frac{\hat{A}_z\Upsilon}{K_{rr}}\right\}\varepsilon_o e^{i\omega t}+\left(\hat{C}^d_{r\theta}-\hat{C}^d_{rr}\right)\frac{g_o}{r_o a^2}e^{i\omega t}. \quad (13)$$

If we now require that the effective radial stress $T_{rr}+\hat{A}_r\tilde{p}$ vanishes at the outer surface of the osteon that corresponds to $\lambda = 1$, we obtain the following restriction:

$$T_{rr}(1,t)+\hat{A}_r\tilde{p}=0=\left[\frac{\hat{C}^d_{r\theta}+\hat{C}^d_{rr}}{2}+\left(\frac{1}{\sqrt{i\bar{\omega}}\Pi(a,1)}-\frac{\hat{C}^d_{r\theta}+\hat{C}^d_{rr}}{2\hat{C}^d_{rr}}\right)\frac{\hat{A}_r\Upsilon}{K_{rr}}\right]f_o e^{i\omega t}+$$

$$\left[\hat{C}^d_{rz}+\left(\frac{1}{\sqrt{i\bar{\omega}}\Pi(a,1)}-\frac{\hat{C}^d_{r\theta}+\hat{C}^d_{rr}}{2\hat{C}^d_{rr}}\right)\frac{\hat{A}_z\Upsilon}{K_{rr}}\right]\varepsilon_o e^{i\omega t}+\left(\hat{C}^d_{r\theta}-\hat{C}^d_{rr}\right)\frac{g_o}{r_o}e^{i\omega t}, \quad (14)$$

where $\bar{\Sigma}(1,1)=0$ and $\bar{\Pi}(1,1)=\frac{1}{\sqrt{i\bar{\omega}}\Pi(a,1)}$. Equations (13) and (14) permit the evaluation of the two constant of integrations f_o and g_o. As g_o is not needed to define the expression of the pore pressure (equation 6), only f_o is evaluated. This is accomplished by multiplying equation (13) by a^2 and subtracting the result from (14); thus,

$$f_o=\frac{\left[a_1-\hat{C}^d_{rz}\left(1-a^2\right)K_{rr}\right]\varepsilon_o}{\frac{\hat{C}^d_{r\theta}+\hat{C}^d_{rr}}{2}\left(1-a^2\right)K_{rr}+\left(\frac{\hat{A}_r-\hat{A}_z}{\sqrt{i\bar{\omega}}\Pi(a,1)}-\hat{A}_r\right)\Upsilon-a_1}, \quad (15)$$

where we have defined

$$a_1 = \left(\frac{\hat{C}^d_{r\theta} - \hat{C}^d_{rr}}{\hat{C}^d_{rr}} \left(\frac{a\bar{\Sigma}(a,1)}{\sqrt{i\bar{\omega}}} + \frac{1-a^2}{2} \right) - \frac{1}{\sqrt{i\bar{\omega}}\Pi(a,1)} \right) \hat{A}_z \Upsilon . \tag{16}$$

Then, by substituting equation (15) into (6), the expression for the pore pressure may be written in the form

$$\tilde{p}(\lambda,t) = \bar{\Pi}(\lambda,1) - 1 \left(\frac{\hat{A}_z}{\hat{A}_r} + \frac{\left[a_1 - \hat{C}^d_{rz} \;\; 1-a^2 \;\; K_{rr} \right] \varepsilon_o}{\frac{\hat{C}^d_{r\theta} + \hat{C}^d_{rr}}{2} \;\; 1-a^2 \;\; K_{rr} + \left(\frac{\hat{A}_r - \hat{A}_z}{\sqrt{i\bar{\omega}}\Pi(a,1)} - \hat{A}_r \right) \Upsilon - a_1} \right) \frac{\Upsilon}{K_{rr}} \varepsilon_o e^{i\omega t} . \tag{17}$$

We are now in a position to calculate $\sigma^*(t)$, the average resultant stress due to the applied cyclic strain loading $\varepsilon(t) = \varepsilon_o e^{i\omega t}$. In this case $\sigma^*(t)$ is defined by

$$\sigma^*(t) = \frac{2}{1-a^2} \int_a^1 T_{zz} \lambda d\lambda , \tag{18}$$

where $\lambda = r/r_o$ is the dimensionless radial coordinate and a is the value of λat the inner cylindrical surface. The substitution of equations (9) and (10) into the expression of T_{zz} in equation (8) leads to

$$T_{zz} = -\left(\bar{\Pi}(\lambda,1) - 1 \right) \left(\frac{\hat{A}_z}{\hat{A}_r} \varepsilon_o + f_o \right) \frac{\hat{A}_z \Upsilon}{K_{rr}} e^{i\omega t} + \hat{C}^d_{rz} \left[1 + \left(\bar{\Pi}(\lambda,1) - 1 \right) \frac{\hat{A}_z \Upsilon}{\hat{C}^d_{rr} K_{rr}} \right] f_o e^{i\omega t} +$$

$$\left(\bar{\Pi}(\lambda,1) - 1 \right) \frac{\hat{C}^d_{rz} \hat{A}_z \Upsilon}{\hat{C}^d_{rr} K_{rr}} \varepsilon_o e^{i\omega t} + \hat{C}^d_{zz} \varepsilon_o e^{i\omega t} ; \tag{19}$$

then, after replacing the expression of T_{zz} from equation (19) into equation (18) and solving the integral, the final form of $\sigma^*(t)$ becomes

$$\sigma^*(t) = C^*(\bar{\omega})\varepsilon(t), \tag{20}$$

where the dynamic modulus $C^*(\bar{\omega})$ is expressed as

$$C^*(\bar{\omega}) = \frac{2}{1-a^2}\left\{\left[\hat{C}^d_{rz}\frac{1-a^2}{2} - \left(\frac{\hat{A}_r}{\hat{C}^d_{rr}}\hat{C}^d_{rz} - \hat{A}_z\right)\left(\frac{a\bar{\Sigma}\ a,1}{\sqrt{i\bar{\omega}}} + \frac{1-a^2}{2}\right)\right]\times\right.$$

$$\frac{\left[a_1 - \hat{C}^d_{rz}\ 1-a^2\ K_{rr}\right]}{\frac{\hat{C}^d_{r\theta}+\hat{C}^d_{rr}}{2}\ 1-a^2\ K_{rr} + \left(\frac{\hat{A}_r-\hat{A}_z}{\sqrt{i\bar{\omega}}\Pi(a,1)} - \hat{A}_r\right)\Upsilon - a_1} +$$

$$\left.\hat{C}^d_{zz}\frac{1-a^2}{2} - \left(\frac{\hat{C}^d_{rz}}{\hat{C}^d_{rr}} - \frac{\hat{A}_z}{\hat{A}_r}\right)\left(\frac{a\bar{\Sigma}(a,1)}{\sqrt{i\bar{\omega}}} + \frac{1-a^2}{2}\right)\hat{A}_z\frac{\Upsilon}{K_{rr}}\right\}. \tag{21}$$

In this case $C^*(\bar{\omega})$ can take the following expression

$$C^*(\bar{\omega}) = C^d_{zz} + \frac{c_1 - c_2K_{rr}}{c_3K_{rr}+c_4} - \frac{c_5}{K_{rr}}, \tag{21a}$$

with c_i, (i=1, 2, 3, 4, 5), constants, defined as

$$c_1 = \left[\hat{C}^d_{rz} - \left(\frac{\hat{A}_r}{\hat{C}^d_{rr}}\hat{C}^d_{rz} - \hat{A}_z\right)\left(\frac{2a\bar{\Sigma}\ a,1}{1-a^2\ \sqrt{i\bar{\omega}}} + 1\right)\right]a_1,$$

$$c_2 = 2\hat{C}^d_{rz}\left[\hat{C}^d_{rz} - \left(\frac{\hat{A}_r}{\hat{C}^d_{rr}}\hat{C}^d_{rz} - \hat{A}_z\right)\left(\frac{a\bar{\Sigma}\ a,1}{\sqrt{i\bar{\omega}}} + \frac{1-a^2}{2}\right)\right],\ c_3 = \frac{\hat{C}^d_{r\theta}+\hat{C}^d_{rr}}{2}\ 1-a^2\ ,$$

$$c_4 = \left(\frac{\hat{A}_r-\hat{A}_z}{\sqrt{i\bar{\omega}}\Pi(a,1)} - \hat{A}_r\right)\Upsilon - a_1, \text{ and } c_5 = \left(\frac{\hat{C}^d_{rz}}{\hat{C}^d_{rr}} - \frac{\hat{A}_z}{\hat{A}_r}\right)\left(\frac{2a\bar{\Sigma}\ a,1}{1-a^2\ \sqrt{i\bar{\omega}}} + 1\right)\hat{A}_z\Upsilon. \tag{21b}$$

The average resultant stress can also be written as

$$\sigma^*(t) = \sigma_o e^{i(\omega t - \delta(\bar{\omega}))} = \sigma_o e^{-i\delta(\bar{\omega})} e^{i\omega t}\,, \tag{22}$$

thus

$$C^*(\bar{\omega}) = C_o e^{-i\delta(\bar{\omega})}, \quad C_o = \frac{\sigma_o}{\varepsilon_o}, \tag{23}$$

where ε_o and σ_o are, respectively, the magnitudes of the applied cyclic strain and the average resultant stress in the osteon while $\delta(\bar{\omega})$ is the phase angle representing the time delay between the harmonic strain and the resultant stress. Equation (23) is an explicit form of the frequency-dependent stiffness (or dynamic modulus of elasticity) of the tissue, which is a function of the porosity and the unknown permeability as shown in equations (21) and (21a). The dynamic modulus $C^*(\bar{\omega})$ is thus dependent on the symmetry and compressibility conditions of the material. In this paper we will restrict our study to the case of the transverse isotropic symmetry with compressible matrix material and a compressible fluid that corresponds to the physical properties of the osteon. In soft tissues such as cartilage, the assumption that the fluid and solid constituents of the poroelastic medium are both incompressible is reasonable because the bulk modulus of the tissue and its constituent fluid are about the same magnitude. For bone tissue, however, the effective bulk modulus of the poroelastic solid constituent of bone tissue is approximately six times stiffer than that of the fluid constituent (Cowin and Doty 2007). Therefore, it is apparent that the pressures in the solid and fluid phases are significantly different compared to the soft tissue situation where they are approximately the same. Thus, the constituent incompressibility assumption that is acceptable for soft tissues is inappropriate for

hard tissues and if this incompressibility assumption is kept for bone tissue, large errors in the determination of bone fluid pressures will emerge.

All the parameters appearing in equation (21) are summarized in Table 3-2 and the values used for the numerical examples in section §4 are expressed in Table 3-3. Using Euler's formula we can write

$$C^*(\bar{\omega}) = C_o e^{i\delta(\bar{\omega})} = C_o \cos[\delta(\bar{\omega})] + iC_o \sin[\delta(\bar{\omega})] = C'(\bar{\omega}) + iC''(\bar{\omega}), \tag{24}$$

where $C'(\bar{\omega})$ is known as the storage modulus and $C''(\bar{\omega})$ as the loss modulus of the osteon. From the equation (24) the expression of the loss tangent is

$$\tan[\delta(\bar{\omega})] = \frac{C''(\bar{\omega})}{C'(\bar{\omega})} = \frac{\sin[\delta(\bar{\omega})]}{\cos[\delta(\bar{\omega})]}. \tag{25}$$

The detail of calculating the storage modulus and loss modulus that represent the real and imaginary parts of $C^*(\bar{\omega})$ is recorded in the appendix, equation (24A), where their formulas for $C'(\bar{\omega})$ and $C''(\bar{\omega})$ are given as

$$C'(\bar{\omega}) = \frac{2}{1-a^2}(m_6 + m_7) \text{ and } C''(\bar{\omega}) = \frac{2}{1-a^2}\ n_6 + n_7\ , \tag{26}$$

where the coefficients m_6, n_6, m_7 and n_7 are defined as

$$\begin{cases} m_6 = \dfrac{(\beta_1\beta_3 - \beta_2\beta_4)\beta_5 + (\beta_1\beta_4 + \beta_2\beta_3)\beta_6}{\beta_5^2 + \beta_6^2}, \\ n_6 = \dfrac{[(\beta_1\beta_3 - \beta_2\beta_4)\beta_6 + (\beta_1\beta_4 + \beta_2\beta_3)\beta_5]}{\beta_5^2 + \beta_6^2}, \end{cases} \tag{27}$$

parameter values		
Constant	Value	Unit
$E_r^m = E_\theta^m$	18.6	GPa
E_z^m	22.32	GPa
$\nu_{r\theta}^m = \nu_{\theta r}^m$	0.322	
$\nu_{zr}^m = \nu_{z\theta}^m$	0.312	
K_{rr}	10^{-22} , 10^{-23} and 10^{-24}	m^2
K_f	2.3	GPa
ϕ	[0.05, .15]	
Δ_1	0.5103	
Δ_2	0.6939	
$\hat{C}_{rr}^d$	20.63	GPa
$\hat{C}_{rz}^d$	7.479	GPa
$\hat{C}_{r\theta}^d$	7.194	GPa
$\hat{C}_{zz}^d$	18.949	GPa
$1/K_{Reff}^m$	$6.23\ 10^{-9}$	GPa^{-1}
$1/K_{Reff}^d$	$8.58\ 10^{-9}$	GPa^{-1}
Λ	$4.52\ 10^{-9}$	GPa^{-1}
$\hat{A}_r$	$0.236\ 10^{-9}$	
$\hat{A}_z$	$0.216\ 10^{-9}$	
J	0.712	
c	$53.71\ 10^{-9}$	m^2s^{-1}

Table 3-3*. Numerical values of the model parameters employed.*

With

$$\begin{cases} \beta_1 = \hat{C}^d_{rz}\dfrac{1-a^2}{2} + \left(\dfrac{\hat{A}_r}{\hat{C}^d_{rr}}\hat{C}^d_{rz} - \hat{A}_z\right)\left(am_4 + \dfrac{1-a^2}{2}\right), & \beta_2 = a\left(\dfrac{\hat{A}_r}{\hat{C}^d_{rr}}\hat{C}^d_{rz} - \hat{A}_z\right)n_4, \\ \beta_3 = \left[\hat{C}^d_{rz}\left(a^2-1\right)K_{rr} - m_5\right], & \beta_4 = n_5, \\ \beta_5 = \dfrac{\hat{C}^d_{r\theta}+\hat{C}^d_{rr}}{2}\left(1-a^2\right)K_{rr} + \left(m_2\left(\hat{A}_r - \hat{A}_z\right) - \hat{A}_r\right)\hat{A}_z\Upsilon - m_5, & \beta_6 = \left(\hat{A}_r - \hat{A}_z\right)n_2\Upsilon - n_5. \end{cases} \tag{28}$$

and

$$\begin{cases} m_7 = \hat{C}^d_{zz}\dfrac{1-a^2}{2} + \dfrac{\hat{A}_z\Upsilon}{K_{rr}}\left(\dfrac{\hat{C}^d_{rz}}{\hat{C}^d_{rr}} - \dfrac{\hat{A}_z}{\hat{A}_r}\right)\left(am_4 + \dfrac{1-a^2}{2}\right), \\ n_7 = \left(\dfrac{\hat{C}^d_{rz}}{\hat{C}^d_{rr}} - \dfrac{\hat{A}_z}{\hat{A}_r}\right)\dfrac{a\hat{A}_z n_4\Upsilon}{K_{rr}}, \end{cases} \tag{29}$$

where $m_1, n_1, m_2, n_2, m_4, n_4, m_5$ and n_5 are defined in the appendix A, equations (7A, 8A, 9A, 11A and 13A), and involve the Kelvin functions ber_n and bei_n (n = 0,1).

3.4. Numerical results

The loss modulus, storage modulus and loss tangent are calculated as functions of the permeability, porosity and frequency for the case of a cylindrical osteon subjected to cyclic loading using equations (25) and (26). For these calculations, two sets of bone elastic constants are needed. The first set is the matrix material constants (E^m_r, E^m_z, $v^m_{r\theta}$, v^m_{rz} and v^m_{zr}) and the second

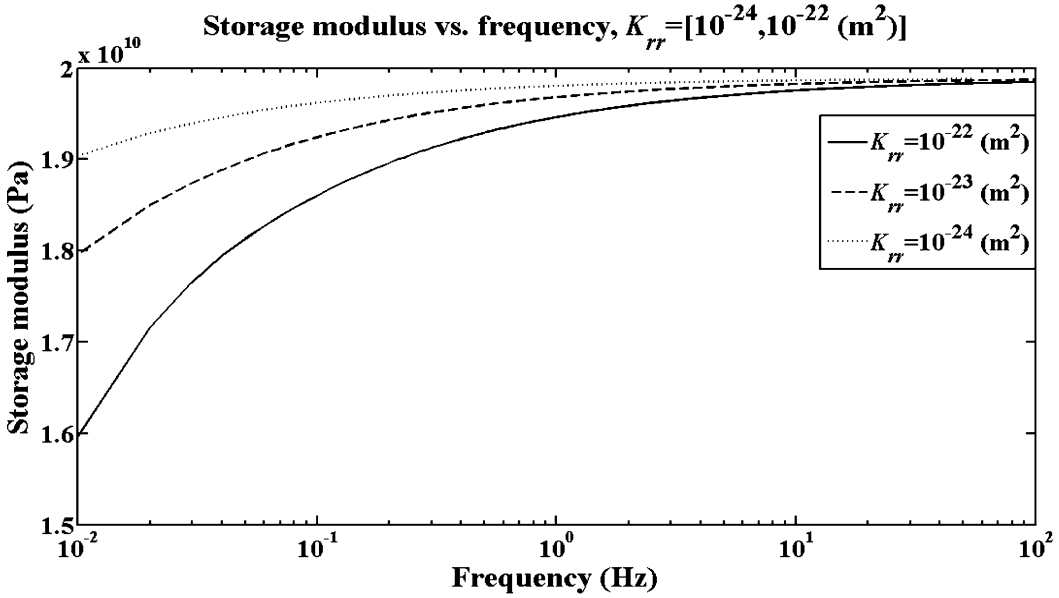

Figure 3-3. *Plots of the storage modulus $C'(\bar{w})$, equation (26), as a function of frequency in the PLC, considering 10% porosity (f) and three different values of permeability, K_{rr} = {10^{-22}, 10^{-23}, 10^{-24} (m^2)}.*

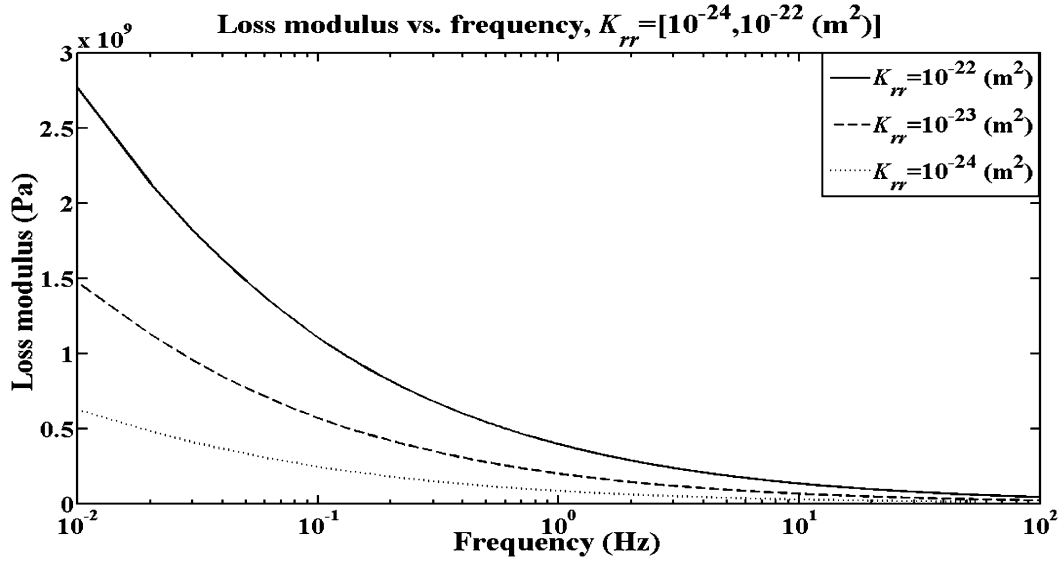

Figure 3-4. *Plots of the loss modulus $C''(\bar{w})$ equation (26), as a function of frequency in the PLC, using $\phi = 0.01$ and K_{rr} = {10^{-22}, 10^{-23}, 10^{-24} (m^2)}.as a function of frequency.*

set is the drained poroelastic constants ($E_r^d, E_z^d, \nu_{r\theta}^d, \nu_{rz}^d$ and ν_{zr}^d). The values of the matrix material constants are adopted from Cowin et al., (2009), and summarized in Table 3-3. The drained elastic constants and the drained Poisson's ratios can be approximated as a function of the porosity and the matrix material constants (Yang et al., 1999),

$$E_r^d = E_r^m\left(1-\phi\right)^{1.92},\ E_z^d = E_z^m\left(1-\phi\right)^{2.80},$$
$$\nu_{r\theta}^d = 0.298\left(1-\phi\right)^{-0.45},\ \nu_{rz}^d = 0.246\left(1-\phi\right)^{-0.19},\ \nu_{zr}^d = 0.295\left(1-\phi\right)^{-0.69}. \quad (30)$$

The behavior of the storage and loss moduli as functions of frequency in an osteon is shown respectively in Figures 3-3 and 3-4. This result was obtained considering 10% porosity (Table 3-4) and using three different values of intrinsic permeability, 10^{-22}, 10^{-23} and 10^{-24} m^2 of the PLC. In these two figures the loss modulus decreases and the storage modulus increases as the permeability decreases from 10^{-22} to 10^{-24} m^2 within the range of frequency analyzed (0.01 to 100 Hz). Therefore, the loss tangent, the ratio of the loss modulus to the storage modulus, should decrease when the permeability decreases, as shown in Figure 3-5, the plot of loss tangent. The storage modulus, the loss modulus and the loss tangent are larger at low frequencies respectively from Figures 3-3, 3-4 and 3-5, therefore, the calculations of loss tangent shown in Figure 3-6 were limited to the frequency range [0.01 - 1 (Hz)]. Figure 3-6 is a 3D-plot of the loss tangent with respect to porosity and permeability at three different frequencies [0.01, 0.1, 1 (Hz)]. This figure provides the possibility of analyzing the behavior of the loss tangent from three different perspectives. First, it shows how the loss tangent decreases as the frequency increases for different values of porosity and permeability. Second, at any constant value of porosity, it shows that the loss tangent increases with an increase in permeability. Third, it illustrates how the loss tangent decreases when the porosity increases at any constant value of permeability.

Reference	Method	PLC Porosity
Gardinier et al., (2010)	Based on Cowin et al., (1999)	5%
Fritton, S*	Confocal microscopy and microstructural measurements	10%
Goulet et al., (2009)	Theoretical estimation based on capillaric and spherical-shell models	12%
Kameo et al., (2010)	Confocal microscopy and microstructural measurements	23%

Table 3-4. *Values of the PLC porosity collected from different studies. The values are ranging from 5% to 23%.*

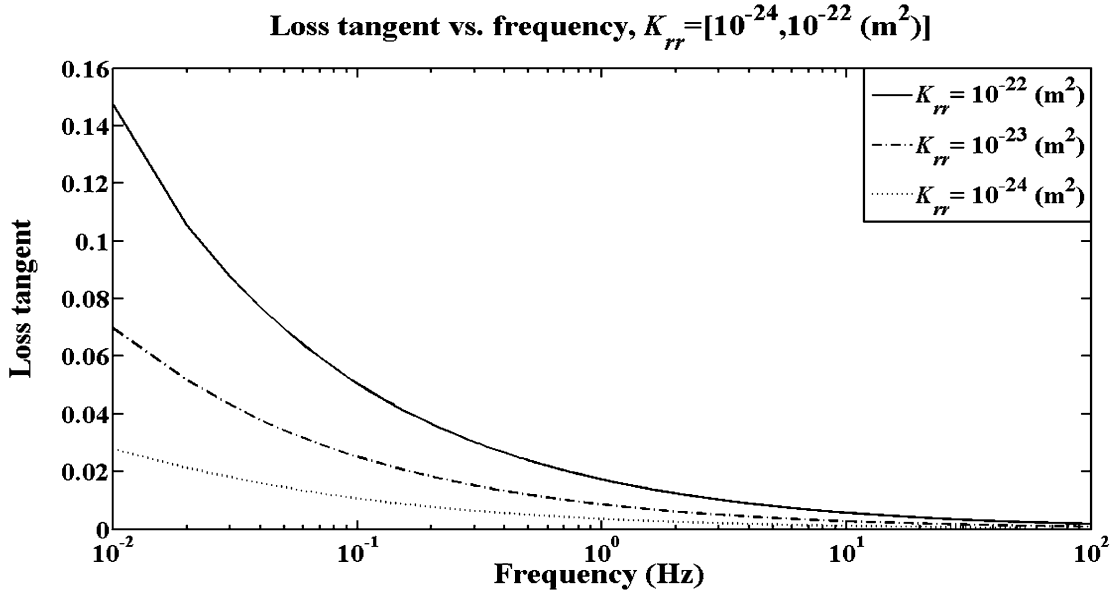

Figure 3-5. *Plots of the loss tangent* $\tan[\delta(\bar{\omega})]$ *in the PLC, equation (25), using* $\phi = 0.01$ *and* K_{rr} *= {10^{-22}, 10^{-23}, 10^{-24} (m^2)} vs. frequency. The loss tangent is the ratio of the imaginary and real parts of the normalized average resultant stress.*

in the evaluation of the expression for the loss tangent can be performed in two different ways. The first method is called derivative-based sensitivity analysis (Wu and Luo, 2011) and consists of determining the partial derivative of the loss tangent with respect to each parameter that may play a key role in determining the value of the expression for the loss tangent. Each partial derivative represents the rate of change of the loss tangent with respect to the related parameter. In other words, the output of each partial derivative illustrates how the corresponding parameter influences the loss tangent and a plot of all the partial derivatives will depict the hierarchy of the corresponding parameters in terms of their degree of influence on the behavior of the loss tangent. The second method is called numerical parametric sensitivity analysis (Ramtani, 2007), and it is based on perturbing the value of each parameter individually with a given percentage of variation considered to be representative of the physiological variability in the osteon. The coefficient of variation, *CV*, produced in the output of the model (loss tangent) as a consequence of the change in value of an input parameter was calculated as the ratio between the standard deviation *SD* and the mean value of the loss tangent generated by the variation on each input of the model individually (equation 30),

$$CV = 100\frac{SD\left(\tan[\delta(\bar{\omega})]\right)}{mean\left(\tan[\delta(\bar{\omega})]\right)}. \tag{31}$$

The sensitivity of the solution for the loss tangent with respect to its significant parameters other than the permeability, specifically the porosity and the two Young's moduli of the matrix material, the radial E_r^m and the axial E_z^m, was evaluated. The algebraic expressions for the loss tangent and its derivative with respect to porosity are dimensionless while the derivatives of the loss tangent with respect to the elastic material constants are not. In order to plot and compare the partial parametric derivatives of the loss tangent, the derivatives with respect to the Young's

moduli are made nondimensional. The nondimensionalized radial E_r^m and the axial E_z^m Young's moduli are then given by

$$E_i^{mo} = \frac{E_i^m}{K^f}, \left(i = r, z\right), \tag{32}$$

where E_i^{mo} are the dimensionless Young's moduli in the radial (i=r) and axial (i=z) directions while K^f is the compressibility of the interstitial fluid. Figure 3-7 shows the results of the derivative-based sensitivity analysis by indicating the degree of influence of each parameter on the output of the loss tangent model. The higher curve with the solid linetype corresponds to the partial derivative of the loss tangent with respect to porosity while the two lower curves with the dotted and the dashed linetypes correspond to the derivatives of the loss tangent with respect to the dimensionless matrix material Young's moduli E_r^{mo} and E_z^{mo}. The hierarchy of the three curves shows that the influence of the porosity on the values of the loss tangent is much higher than the influence of the axial or radial matrix material Young's moduli. This behavior was confirmed by using the numerical parametric sensitivity analysis method. A –20% to +20% perturbation was applied independently to each set of parameters, resulting in an average deviation on the loss tangent of 20% in the case of the porosity while it didn't exceed respectively 0.8% and 1% for the case of the radial and the axial matrix material Young's moduli.

Recently, we have determined the PLC permeability of an isolated osteon using stress relaxation measurements (Gailani et al., 2009) that were based on a stress relaxation poroelastic model of an annular poroelastic cylinder as described in Gailani and Cowin (2008). The stress relaxation test procedure was replaced in this study by cyclic loading, which is closer to the normal physiological loading condition in bones than the stress relaxation test. Ambulation of a

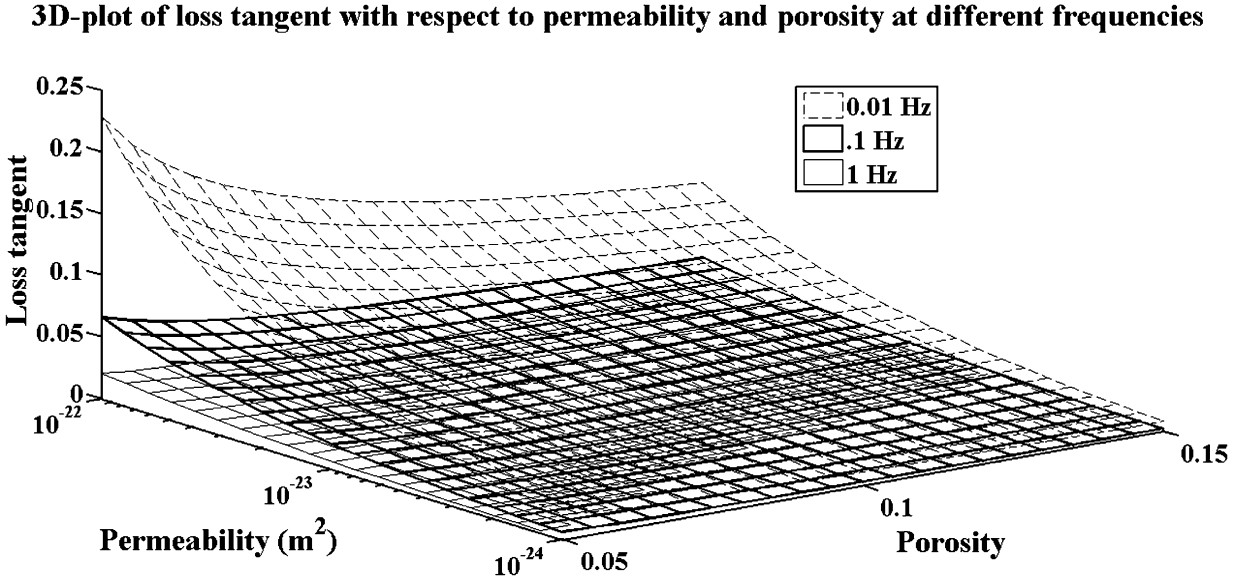

Figure 3-6. *3D-plots of loss tangent $\tan[\delta(\bar{\omega})]$ with respect to porosity and permeability at three different frequencies, 0.01, 0.1 and 1 (Hz). The ranges of permeability and porosity are respectively $[10^{-22}, 10^{-24}\ (m^2)]$ and [0.05, 0.15].*

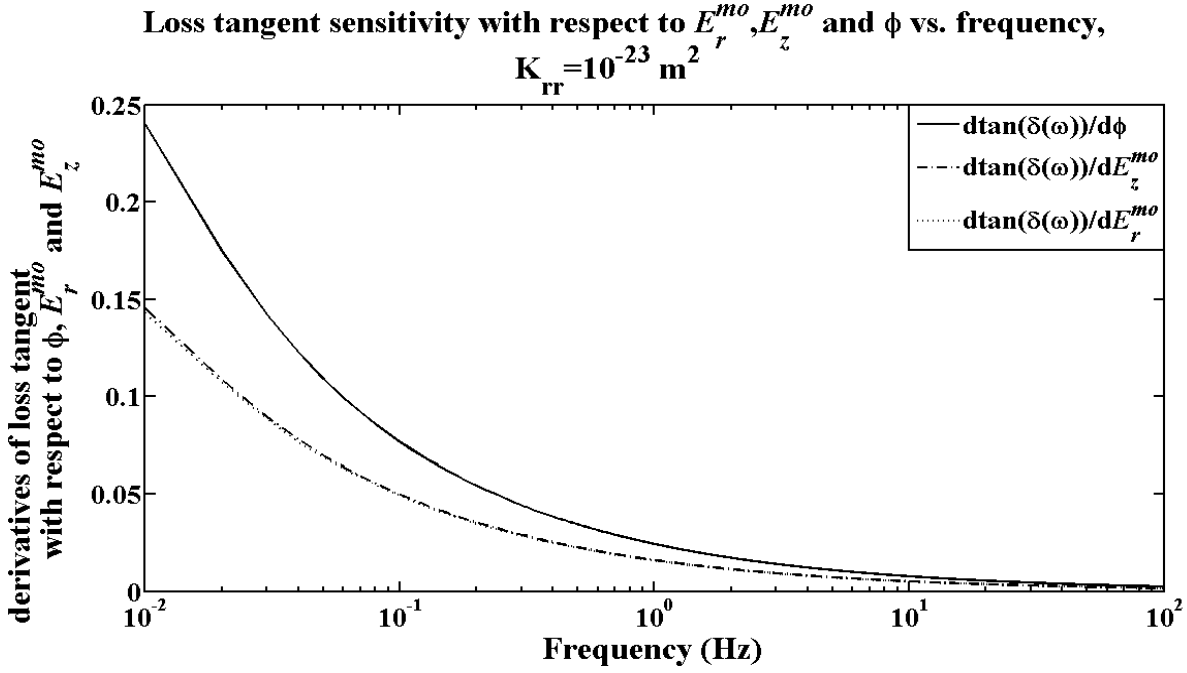

Figure 3-7. *Derivative-based sensitivity plot of the loss tangent with respect to porosity and dimensionless matrix material Young's moduli with $K_{rr} = 10^{-23}\ m^2$. The higher curve with the solid linetype corresponds to the partial parametric derivative of the loss tangent while the two other curves with the dotted and the dashed linetypes correspond respectively to the partial parametric derivatives of the loss tangent with respect to the normalized elastic matrix material constants E_r^{mo} and E_z^{mo}.*

human body involves frequencies of about one Hertz and muscles have operational frequencies in the 30 Hertz range while measurements have shown that frequencies of several hundred Hertz occur in moving living bones (Cowin and Doty 2007).

3.5. Discussion

This paper is a part of a continuing work aimed at the development of a model describing the phase angle that an osteonal specimen exhibits under cyclic mechanical loading in the case of specified elastic constants depends mainly upon the permeability and porosity. Expressions for the storage modulus, loss modulus and loss tangent are obtained from the poroelastic model. Figures 3-3, 3-4 and 3-5 depict respectively the 2D- plots of the storage modulus, the loss modulus and the loss tangent with respect to frequency for the parameter values specified in Table 3-3. Figure 3-6 illustrates the 3D-plots of the loss tangent with respect to permeability and porosity at different frequencies [0.01, 0.1, 1 (Hz)] while Figure 3-7 represents the plots of the loss tangent derivatives with respect to the porosity and the elastic matrix material Young's moduli at a permeability of 10^{-23} m^2. The plots in Figure 3-3 refer to the storage modulus, which illustrate how the effective stiffness of an osteon specimen behaves with frequency. At low frequencies these curves increase sharply, then, the increasing rate of the storage modulus starts decreasing monotonically until it becomes almost steady around 10^2 Hz. The plots of Figure 3-4 represent the loss modulus while Figures 3-5 and 3-6 represent the loss tangent. The plots of loss tangent and loss modulus express how the energy dissipation and mechanical damping vary in an osteonal sample with respect to frequency, permeability and porosity. In contrast to the curves for the storage modulus that are increasing with frequency, the curves for the loss modulus

(Figure 3-4) and the loss tangent (Figure 3-5) are decreasing. At high frequencies these curves converge towards zero asymptotically, which means that the behavior of the bone sample at high frequencies is purely elastic. The storage modulus, the loss modulus and the loss tangent are respectively represented with cosine, sine and tangent of the phase angle by the formulas represented in equations (24) and (25). In other words, this means that there is a causal relation between the variability of these physical properties and the variation of the phase angle. The results from this analytical model are the foundation for the experimental design of a forthcoming study, in which the variation of the phase angle with respect to frequency will be used to determine the permeability of the lacunar-canalicular porosity in a section of a single osteon. In particular, it can be inferred from the curves in Figures 3-3, 3-4, 3-5 and 3-7 that the most sensitive range of frequency for the planned experimental study would be between 10^{-2} and 10^{1} Hz. Importantly, this range of frequency contains the physiological level of frequency at which mechanical loading is considered to be applied to bone in humans. Moreover, it can be concluded from Figure 3-7 that the porosity is the most influential parameter affecting the magnitude of the loss tangent, and that the loss tangent is highly sensitive to the frequency, decreasing exponentially as the frequency increases.

The numerical results produced by our model are close to the results of loss tangent previously reported in the literature. For instance, the values of loss tangent predicted by this model and presented in Figure 3-5 are close to the experimental loss tangent curves presented by Garner et al., (2000). From their Figures 3-5 and 3-4, the reported values of loss tangent are between 0.06 at 10^{-2} Hz and 0.02 at 10^{2} Hz. In another study by Drabousky (2009), the loss modulus and storage modulus are plotted in their Figures 3.20 and 3.22 respectively. At the same frequencies, the values of loss tangent calculated from their curves vary from 0.075 to 0.015. In

this study, the values of the loss tangent obtained from our analytical model are between 0.14 at 10^{-2} Hz and 0.005 at 10^{2} Hz. The small differences in the behavior of the storage modulus, the loss modulus and the loss tangent that can be observed with a comparison of the plots in Figures 3-3, 3-4 and 3-5 with the corresponding figures from Garner et al., (2000) and Drabousky (2009) may be attributed to two facts. First, we assumed that our specimens were microscopic cylindrical sections of osteons that included only the PLC and excluded the PV, while they used in both studies macroscopic samples that included the PLC and the PV. Second, we calculated our analytical models based on cyclic strain and resultant stresses, while in both papers they adopted different experimental approaches to determine their data. In Garner et al., (2000) the loss tangent was determined in cylindrical specimen harvested from human tibia in the transversal and longitudinal directions. For the transversal direction the authors used bending moments and resultant bending deformation while in the longitudinal direction they used harmonic torque and resultant angular displacement experiments. Concerning the second paper, Drabousky (2009) used tensile relaxation tests at different load magnitudes and strain rates to determine the loss modulus and the storage modulus in cylindrical equine cortical bone specimens.

Finally, the present work contains two limitations. First, the geometrical idealization of the osteonal specimen as a right circular cylinder approximately corresponds to the shape of the osteon. Second, the impermeable boundary condition assumed at the cement line for the ODE (4) might not be totally correct. Wang et al., (1999) assumed that the cement line is slightly permeable. However, even if this permeability exists, it is negligible in comparison to the one at the inner boundary between the PLC and the PV porosities.

Appendix: Determination of the real and imaginary parts of $C^*(\bar{\omega})$

The expression of the modulus $C^*(\bar{\omega})$ in equation (21) contains hierarchical complex components such as a_1 and $\frac{a\bar{\Sigma}(a,1)}{\sqrt{i\bar{\omega}}}$ with

$$\bar{\Sigma}(a,1)=\frac{\Sigma(a,1)}{\Pi(a,1)}, \tag{1A}$$

and

$$\begin{cases}\Sigma(a,1)=I_1(a\sqrt{i\bar{\omega}})K_1(\sqrt{i\bar{\omega}})-I_1(\sqrt{i\bar{\omega}})K_1(a\sqrt{i\bar{\omega}}),\\ \Pi(a,1)=I_o(a\sqrt{i\bar{\omega}})K_1(\sqrt{i\bar{\omega}})+I_1(\sqrt{i\bar{\omega}})K_o(a\sqrt{i\bar{\omega}})\end{cases} \tag{2A}$$

where I_n and K_n (n= 0, 1) are Bessel functions. Now if we let $x_1=\sqrt{\bar{\omega}}$ and $x_2=a\sqrt{\bar{\omega}}$, the forms of $\Sigma(a,1)$ and $\Pi(a,1)$ in (2A) are rewritten as

$$\begin{cases}\Pi(a,1)=I_o(x_2\sqrt{i})K_1(x_1\sqrt{i})+I_1(x_1\sqrt{i})K_o(x_2\sqrt{i}),\\ \Sigma(a,1)=I_1(x_2\sqrt{i})K_1(x_1\sqrt{i})-I_1(x_1\sqrt{i})K_1(x_2\sqrt{i}).\end{cases} \tag{3A}$$

From Abramowitz and Stegun (1964), equations (9.9.1) and (9.9.2), we have

$$\begin{cases}I_o(xe^{\frac{i\pi}{4}})=ber_o x+i(bei_o x),\ I_1(xe^{\frac{i\pi}{4}})=bei_1 x-i(ber_1 x),\\ K_o(xe^{\frac{i\pi}{4}})=ker_o x+i(kei_o x),\ K_1(xe^{\frac{i\pi}{4}})=-kei_o x+i(ker_o x),\end{cases} \tag{4A}$$

where ber_n, bei_n (n = 0, 1) are Kelvin functions. Thus,

$$
\begin{aligned}
I_o(x_2\sqrt{i})K_1(x_1\sqrt{i}) &= [ber_o x_2 + i(bei_o x_2)][-kei_1 x + i(ker_1 x)] \\
&= -ber_o x_2 kei_1 x_1 + i(ber_o x_2 \ker_1 x_1) - i(bei_o x_2 kei_1 x_1) - bei_o x_2 ker_1 x_1 , \\
&= -ber_o x_2 kei_1 x_1 - bei_o x_2 ker_1 x_1 + i(ber_o x_2 ker_{11} x_1 - bei_o x_2 kei_1 x_1)
\end{aligned} \tag{5A}
$$

and

$$
\begin{aligned}
I_1(x_1\sqrt{i})K_o(x_2\sqrt{i}) &= [bei_1 x_1 - i(ber_1 x_1)][ker_o x_2 + i(kei_o x_2)] \\
&= bei_1 x_1 ker_o x_2 + i(bei_1 x_1 kei_o x_2) - i(ber_1 x_1 ker_o x_2) + ber_1 x_1 kei_o x_2 , \\
&= bei_1 x_1 ker_o x_2 + ber_1 x_1 kei_o x_2 + i(bei_1 x_1 kei_o x_2 - ber_1 x_1 ker_o x_2)
\end{aligned} \tag{6A}
$$

which means

$$
\begin{aligned}
\Pi(a,1) &= I_o(x_2\sqrt{i})K_1(x_1\sqrt{i}) + I_1(x_1\sqrt{i})K_o(x_2\sqrt{i})] \\
&= -ber_o x_2 kei_1 x_1 - bei_o x_2 ker_1 x_1 + i(ber_o x_2 ker_1 x_1 - bei_o x_2 kei_1 x_1) \\
&\quad + bei_1 x_1 ker_o x_2 + ber_1 x_1 kei_o x_2 + i(bei_1 x_1 kei_o x_2 - ber_1 x_1 ker_o x_2) \\
&= -ber_o x_2 kei_1 x_1 - bei_o x_2 ker_1 x_1 + bei_1 x_1 ker_o x_2 + ber_1 x_1 kei_o x_2 \\
&\quad + i(ber_o x_2 ker_1 x_1 - bei_o x_2 kei_1 x_1 + bei_1 x_1 kei_o x_2 - ber_1 x_1 ker_o x_2) \\
&= m_1 + in_1 .
\end{aligned} \tag{7A}
$$

Following the expression (7A) the term $\dfrac{1}{\sqrt{i\bar{\omega}}\Pi(a,1)}$ in equation (8) is rewritten as

$$
\frac{1}{\sqrt{i\bar{\omega}}\Pi(a,1)} = \frac{1}{\sqrt{i\bar{\omega}}(m_1 + in_1)} = m_2 + in_2 \text{ since } \sqrt{i\bar{\omega}} = \sqrt{\bar{\omega}}e^{\frac{i\pi}{4}} = \sqrt{\frac{\bar{\omega}}{2}}(1+i) \tag{8A}
$$

with

$$
m_2 = \frac{m_1 - n_1}{\sqrt{\frac{\bar{\omega}}{2}}((m_1 - n_1)^2 + (m_1 + n_1)^2)} \text{ and } n_2 = \frac{-m_1 - n_1}{\sqrt{\frac{\bar{\omega}}{2}}((m_1 - n_1)^2 + (m_1 + n_1)^2)} . \tag{9A}
$$

From the other side the substitution of equations (4A) into the form of $\Sigma(a,1)$ from (3A) leads to

$$\begin{aligned}\Sigma(a,1) &= I_1(x_2\sqrt{i})K_1(x_1\sqrt{i}) - I_1(x_1\sqrt{i})K_1(x_2\sqrt{i}) \\ &= -ber_1x_2kei_1x_1 - bei_1x_2ker_1x_1 + i(ber_1x_2ker_1x_1 - bei_1x_2kei_1x_1) \\ &\quad - bei_1x_1ker_1x_2 - ber_1x_1kei_1x_2 - i(-bei_1x_1kei_1x_2 + ber_1x_1ker_1x_2) \\ &= -ber_1x_2kei_1x_1 - bei_1x_2ker_1x_1 - bei_1x_1ker_1x_2 - ber_1x_1kei_1x_2 \\ &\quad + i(ber_1x_2ker_1x_1 - bei_1x_2kei_1x_1 - bei_1x_1kei_1x_2 + ber_1x_1ker_1x_2) \\ &= m_3 + in_3,\end{aligned} \tag{10A}$$

and by replacing (8A) and (10A) in $\frac{\bar{\Sigma}(a,1)}{\sqrt{i\bar{\omega}}}$ defined in equations (1A) and (8A), the general form becomes

$$\frac{\bar{\Sigma}(a,1)}{\sqrt{i\bar{\omega}}} = m_4 + in_4, \tag{11A}$$

where

$$\begin{cases} m_4 = \sqrt{\dfrac{2}{\bar{\omega}}}\,\dfrac{m_3(m_1+n_1)+n_3(n_1-m_1)}{m_1^2+n_1^2}, \\ n_4 = \sqrt{\dfrac{2}{\bar{\omega}}}\,\dfrac{m_3(m_1-n_1)+n_3(n_1+m_1)}{m_1^2+n_1^2}. \end{cases} \tag{12A}$$

Then, by substituting equations (11A) and (8A) into equation (16) the expression of a_1 is rewritten as

$$a_1 = m_5 + in_5, \tag{13A}$$

where

$$\begin{cases} m_5 = \dfrac{\left(\hat{C}^d_{rr} - \hat{C}^d_{r\theta}\right)}{\hat{C}^d_{rr}}\left(am_4 + \dfrac{1-a^2}{2} - m_2\right)\hat{A}_z\Upsilon, \\ n_5 = (a\dfrac{\left(\hat{C}^d_{rr} - \hat{C}^d_{r\theta}\right)}{\hat{C}^d_{rr}}n_4 - n_2)\hat{A}_z\Upsilon. \end{cases} \tag{14A}$$

Now let's write $C^*(\bar{\omega})$ from equation (21) as

$$C^*(\bar{\omega}) = \frac{2}{1-a^2}[H_1 + H_2]a, \tag{15A}$$

where

$$H_1 = \left[\hat{C}^d_{rz}\frac{1-a^2}{2} - \left(\frac{\hat{A}_r}{\hat{C}^d_{rr}}\hat{C}^d_{rz} - \hat{A}_z\right)\left(\frac{a\bar{\Sigma}(a,1)}{\sqrt{i\bar{\omega}}} + \frac{1-a^2}{2}\right)\right]\times$$

$$\frac{\left[a_1 - \hat{C}^d_{rz}\ 1-a^2\ K_{rr}\right]\varepsilon_o}{\frac{\hat{C}^d_{r\theta} + \hat{C}^d_{rr}}{2}\ 1-a^2\ K_{rr} + \left(\frac{\hat{A}_r - \hat{A}_z}{\sqrt{i\bar{\omega}}\Pi(a,1)} - \hat{A}_r\right)\hat{A}_z - a_1}, \tag{16A}$$

and

$$H_2 = \hat{C}^d_{zz}\frac{1-a^2}{2} + \left(\frac{\hat{C}^d_{rz}}{\hat{C}^d_{rr}} - \frac{\hat{A}_z}{\hat{A}_r}\right)\left(\frac{a\bar{\Sigma}(a,1)}{\sqrt{i\bar{\omega}}} + \frac{1-a^2}{2}\right)\frac{\hat{A}_z\Upsilon}{K_{rr}}. \tag{17A}$$

Thus, from one side the substitution of equations (11A) and (13A) into equation (16A) gives

$$H_1 = [\hat{C}^d_{rz}\frac{1-a^2}{2} + (\frac{\hat{A}_r}{\hat{C}^d_{rr}}\hat{C}^d_{rz} - \hat{A}_z)(a(m_4 + in_4) + \frac{1-a^2}{2})]\times$$

$$\frac{\{[m_5 + in_5 - \hat{C}^d_{rz}(a^2-1)K_{rr}\}}{\frac{\hat{C}^d_{r\theta} + \hat{C}^d_{rr}}{2}(1-a^2)K_{rr} + [(m_2 + in_2)(\hat{A}_r - \hat{A}_z) - \hat{A}_r]\Upsilon - m_5 - in_5]} = m_6 + in_6, \tag{18A}$$

where

$$\begin{cases} m_7 = \dfrac{(\beta_1\beta_3 - \beta_2\beta_4)\beta_5 + (\beta_1\beta_4 + \beta_2\beta_3)\beta_6}{\beta_5^2 + \beta_6^2}, \\ n_7 = \dfrac{(\beta_1\beta_4 + \beta_2\beta_3)\beta_5 + (\beta_2\beta_4 - \beta_1\beta_3)\beta_6}{\beta_5^2 + \beta_6^2}, \end{cases} \tag{19A}$$

with

$$\begin{cases} \beta_1 = \hat{C}_{rz}^d \dfrac{1-a^2}{2} + \left(\dfrac{\hat{A}_r}{\hat{C}_{rr}^d} \hat{C}_{rz}^d - \hat{A}_z \right) \left(am_4 + \dfrac{1-a^2}{2} \right), & \beta_2 = a \left(\dfrac{\hat{A}_r}{\hat{C}_{rr}^d} \hat{C}_{rz}^d - \hat{A}_z \right) n_4, \\ \beta_3 = \left[\hat{C}_{rz}^d \left(a^2 - 1 \right) K_{rr} - m_5 \right], & \beta_4 = n_5, \\ \beta_5 = \dfrac{\hat{C}_{r\theta}^d + \hat{C}_{rr}^d}{2} \left(1 - a^2 \right) K_{rr} + \left(m_2 \left(\hat{A}_r - \hat{A}_z \right) - \hat{A}_r \right) \hat{A}_z \Upsilon - m_5, & \beta_6 = \left(\hat{A}_r - \hat{A}_z \right) n_2 \Upsilon - n_5. \end{cases} \tag{20A}$$

From the other side, by substituting equation (11A) into equation (17A), the expression of H_2 is rewritten as

$$H_2 = m_7 + in_7, \tag{21A}$$

where

$$\begin{cases} m_7 = \hat{C}_{zz}^d \dfrac{1-a^2}{2} + \dfrac{\hat{A}_z \Upsilon}{K_{rr}} \left(\dfrac{\hat{C}_{rz}^d}{\hat{C}_{rr}^d} - \dfrac{\hat{A}_z}{\hat{A}_r} \right) \left(am_4 + \dfrac{1-a^2}{2} \right), \\ n_7 = \left(\dfrac{\hat{C}_{rz}^d}{\hat{C}_{rr}^d} - \dfrac{\hat{A}_z}{\hat{A}_r} \right) \dfrac{a\hat{A}_z n_4 \Upsilon}{K_{rr}}, \end{cases} \tag{22A}$$

Finally by introducing equations (21A) and (18A) into (15A) the expression of the normalized pressure $C^*(\bar{\omega})$ is rewritten as

$$C^{*}(\bar{\omega}) = C^{'}(\bar{\omega}) + iC^{''}(\bar{\omega}), \tag{23A}$$

where

$$\begin{cases} C^{'}(\bar{\omega}) = \dfrac{2}{1-a^{2}}(m_{6} + m_{7}), \\ C^{''}(\bar{\omega}) = \dfrac{2}{1-a^{2}}(n_{6} + n_{7}). \end{cases} \tag{24A}$$

References

Abramowitz M, Stegun IA (1964) Handbook of Mathematical functions with Formulas, Graphs and Mathematical Tables. National Bureau of Standards Applied Mathematics Series 55, 379- 80

Beno T, Yoon YJ, Cowin SC, Fritton SP (2006) Estimation of bone permeability using accurate microstructural measurements. J. Biomech. 39: 2378–87

Buechner PM, Lakes RS (2003) Size effects in the elasticity and viscoelasticity of bone. Biomech. Model. Mechanobiol. 1: 295 – 301

Burger EH, Klein-Nulend J, van der Plas A, Nijweide PJ (1995) Function of Osteocytes in Bone–Their Role in Mechanotransduction. J. Nutr. 125(7 Suppl):2020S-2023S

Cowin SC (1999) Bone poroelasticity. J. Biomech. 32: 217-238

Cowin SC (2001) Bone mechanics handbook. 2nd edn Boca Raton, FL: CRS Press. 17: 2-5

Cowin SC, Doty SB (2007) Tissue Mechanics. Springer. pp 348, 360

Cowin SC, Gailani G, Benalla M (2009) Hierarchical Poroelasticity: Movement of interstitial fluid between porosity levels in bones. Phil. Trans. R. Soc. 367: 3401–43

Cowin SC, Moss-Salentijn L, Moss ML (1991), ‘‘Candidates for the Mechanosensory System in Bone,’’ J. Biomech. Eng. 113: 191–197

Cowin SC, Weinbaum S, Zeng Y (1995) A case for bone canaliculi as the anatomical site of strain-generated potentials, J. Biomech. 28: 1281-96

Drabousky DP (2009) Prony Series Representation and Interconversion of Viscoelastic Material Functions of Equine Cortical Bone. Department of Mechanical and Aerospace Engineering, Western Reserve University

Fornells P, García-Aznar JM, Doblaré M (2007) A finite element dual porosity approach to model deformation-induced fluid flow in cortical bone. Ann. Biomed. Eng. 35: 1687–1698

Fritton SP, Wang L, Weinbaum S, Cowin SC (2001) Interaction of mechanical loading, blood flow, and interstitial fluid flow in osteonal bone. Proceedings of the Bioengineering conference. BED 50: 341-42

Fritton SP, Weinbaum S (2009) Fluid and solute transport in bone: Flow induced mechanotransduction. Annu. Rev. Fluid Mech. 41: 347–74

Gailani GB, Benalla M, Mahamud R, Cowin SC, Cardoso L (2009) Experimental Determination of the Permeability in the Lacunar-Canalicular Porosity of Bone. J. Biomech. Eng. 131: 1010071-7

Gailani GB, Cowin SC (2008) The unconfined compression of a poroelastic annular cylindrical disk. Mechanics of Materials. 40: 507-23

Gardinier JD, Townend CW, Jen KP, Wu Q, Duncan RL, Wang L (2010). In situ permeability measurement of the mammalian lacunar-canalicular system. J. Bone 46: 1075-81

Garner E, Lakes R, Lee T, Swan C, Brand R (2000) Viscoelastic dissipation in compact bone: implications for stress-Induced fluid flow in bone. J. Biomech. Eng. 122: 167-172

Goulet GC, Coombe D, Martinuzzi RJ, Zernicke RF (2009) Poroelastic evaluation of fluid movement through the lacunocanalicular system. Ann. Biomed. Eng. 37-7: 1390–1402

Gururaja S, Kim HJ, Swan CC, Brand RA, Lakes RS (2005) Modeling deformation-induced fluid flow in cortical bone's canalicular–lacunar system. Ann. Biomed. Eng. 33: 7- 25

Han Y, Cowin SC, Schaffler MB, Weinbaum S (2004) Mechanotransduction and strain amplification in osteocyte cell processes and flow across the endothelial glycocalyx. Proc. Nat. Acad. Sci. USA. 101: 16689-94

Jee W (1988) The skeletal tissues. In L. Weiss (Ed.), Cell and Tissue Biology: a Textbook of Histology. Baltimore: Urban & Schwarzenberg. pp 207

Kameo Y, Adachi T, Sato N, Hojo M (2010) Estimation of bone permeability considering the morphology of lacuno-canalicular porosity. Journal of the Mechanical Behavior of Biomedical Materials , 3: 240-248

Lakes RS (1982) Dynamical study of couple stress effects in human compact bone. J. Biomech. Eng. 104: 7–11

Nguyen V, Lemaire T, Naili S (2009) Numerical study of deformation-induced fluid flows in periodic osteonal matrix under harmonic axial loading. C. R. Mecanique. 337: 268–76

Oyen ML (2008) Poroelastic nanoindentation responses of hydrated bone. J. Mater. Res. 23: 1307-14

Ramtani S (2007) Parametric sensitivity analysis applied to a specific one-dimensional internal bone remodeling problem. Computers in Biology and Medicine. 37: 1203 – 09

Rémond A, Naïli S, Lemaire T (2008) Interstitial fluid flow in the osteon with spatial gradients of mechanical properties: a finite element study. Biomech. Model. Mechanobiol. 7: 487–95

Smit TH, Huyghe JM, Cowin SC (2002) Estimation of the poroelastic parameters of bone. J. Biomech. 35: 829-36.

Swan CC, Lakes RS, Brand RA, Stewart KJ (2003) Micromechanically based poroelastic modeling of fluid flow in Haversian bone. J. Biomech. Eng. 125: 25-37

Wang L, Fritton SP, Cowin SC, Weinbaum S (1999) Fluid pressure relaxation depends upon osteonal microstructure: modeling an oscillatory bending experiment. J. Biomech. 32: 663-72

Wang L, Fritton SP, Weinbaum S, Cowin SC (2003) On bone adaptation due to venous stasis. J. Biomech. 36: 1439-51

Weinbaum S, Cowin SC, Zeng Y (1994) A model for the excitation of osteocytes by mechanical loading-induced bone fluid shear stresses. J. Biomech. 27: 339-60

Wu D, Ci S, Luo H (2011). A theoretical framework for interaction measure and sensitivity analysis in cross-layer design. ACM Transactions on Modeling and Computer Simulation. 21: 1-26

Yang G, Kabel J, Rietbergen BV, Odgaard A, Huiskes R, Cowin SC (1999). The Anisotropic Hooke's Law for Cancellous Bone and Wood. Journal of Elasticity. 53: 125–146

Zeng Y, Cowin SC, Weinbaum S (1994) A fiber matrix model for fluid flow and streaming potentials in the canaliculi of an osteon. Ann. Biomed. Eng. 22: 280–92

Zhang D, Weinbaum S, Cowin SC (1998) Estimates of the peak pressures in the bone pore water. J. Biomech. Eng. 120: 697-703

Zhou X, Novotny JE, Wang L (2008) Modeling fluorescence recovery after photobleaching in loaded bone: potential applications in measuring fluid and solute transport in the osteocytic lacunar–canalicular system. Ann. Biomed. Eng. 36: 1961–77

Chapter 4

Experimental Determination of the Lacunar-Canalicular Permeability of Human Cortical Bone Using Cyclic Loading

To be submitted to the PNAS

Abstract.

The intrinsic permeability associated with the lacunar-canalicular porosity (PLC) of bone is a property that plays a critical role in bone interstitial fluid flow. This flow is thought to be the stimulus of the mechanosensory phenomenon associated with osteocytes, the sensory cells in bone. However, theoretical and experimental values of PLC permeability span several orders of magnitude, suggesting that has not been determined with sufficient accuracy to date. The PLC permeability based on theoretical analysis ranges from 10^{-17} to $10^{-23}m^2$, and the experimental measurements reported in the literature range from 10^{-22} to $10^{-25}m^2$. Major difficulties associated with the measurement of the PLC permeability include, (a) the influence of the vascular porosity (PV) on the measurements since both are intertwined in cortical bone tissue, (b) the challenge to perform direct measurements of permeability on samples with very small intrinsic permeability (i.e. 10^{-17} to 10^{-25} m^2) and very small size (i.e., 100 to 250 μm in diameter and 0.5 mm in height), (c) the complexity of performing the measurements of the PLC permeability in human bone *in vivo*, (d) the imprecise knowledge concerning boundary conditions and the values for the key material parameters in our analytical models for estimating the PLC permeability.

In this study, we have made an effort to address and limit the effect of most of those concerns. First, bone specimens that contain the PLC and exclude the PV (i.e. single osteon samples) were prepared for experimental testing. Second, while direct measurements of PLC permeability using Darcy's experiment cannot be performed in those samples, they permit estimating the PLC permeability by curve fitting of experimental data of the phase delay (phase angle between the applied strain and the produced stress) during cyclic loading of isolated osteons and a poroelastic model of an annular cylinder representing an osteon under harmonic loading (Benalla et al., 2011). Third, *in vivo* measurement cannot be carried out in human

tissues; however, performing *ex vivo* experiments in fresh samples is possible. Therefore, experiments were performed in osteons that were harvested from the mid-diaphysis of fresh human femora and tested within five hours of their cutting to investigate the variability of the loss tangent with respect to time. Fourth, inputs of the model (lacunar-canalicular porosity, tissue elastic modulus) were measured/estimated for each osteon.

In addition to the complexity in measuring the PLC permeability, there is a lack of data on the role of loading frequency (or the strain rate) on the behavior of the PLC permeability. Therefore, the behaviors of the loss tangent and the PLC permeability with respect to frequency were investigated. Since our sensitivity study indicated that the most important parameter affecting both loss tangent and PLC permeability was the porosity of the lacunar-canalicular domain, the correlation coefficient between loss tangent and PLC as well as between PLC permeability and PLC were determined. The intrinsic permeability in the radial direction of the lacunar-canalicular porosity at physiological ranges of frequencies was found to be of the order of 10^{-22} m^2 and exhibited a frequency-dependent behavior, characterized by a linear decrease of the PLC permeability at a rate of $-3x10^{-24}$ m^2/Hz within the range of 1 and 100 Hz. The PLC permeability values found in this study are in reasonable agreement with both theoretical and experimental approaches. More specifically, they lie in the low range of PLC permeability by theoretical models and in the high range of PLC permeability by experimental approaches.

Key Terms: *Lacunar-canalicular porosity, phase angle, human cortical bone, harmonic loading, micromechanical loading, micro computed tomography.*

4.1. Introduction

Bone tissue has the capability of adapting its local tissue mass and architecture to its mechanical environment (Wolff, 1892). This remodeling process requires external forces to be sensed by osteocytes, the principal mechanosensory cells of bone that reside in the lacunae (pores) of the lacunar–canalicular porosity, PLC (Cowin 1999). Mechanical loading of bones produces movement of bone fluid from the region of the bone vasculature through the canaliculi and the lacunae of the surrounding mineralized tissue, and in the reverse direction, accomplishing three important tasks. First, it transports nutrients to the cells in the lacunae buried in the mineralized matrix. Second, it carries away the cell waste. Third, the deformation-driven interstitial fluid movement in the PLC exerts a force on the osteocyte process, a force that is large enough for the cell to sense, which is considered as the basic mechanotransduction mechanism in bone cells *in vivo* (Cowin et al. 1991; Weinbaum et al. 1994; Cowin et al. 1995; Fritton and Weinbaum 2009).

The lacunar-canalicular permeability is a major factor influencing the fluid transport and the mechanotransduction phenomenon in bone. However, studies of permeability in human cortical bone are scarce. An estimate of the PLC permeability was first proposed by Zang et al. (1998) based on an ultrastructural model of the lacunar-canalicular system, predicting PLC permeability on the order of 10^{-20} to 10^{-22} m^2. Based on Biot's poroelasticity theory, Wang et al. (1999) found the PLC permeability of bovine bone to be in the range of 10^{-20} m^2, Gururaja et al. (2005) reported the PLC permeability to be 10^{-22} and 10^{-21} m^2, and Zhou et al. (2008) obtained an estimate of the PLC permeability in mice on the order of 10^{-22} and 10^{-21} m^2.

Traditional permeability measurement techniques based on Darcy's technique of measuring the volume of fluid flow per unit area and per unit time across a porous layer, which

is then divided by the pore pressure gradient across the layer, seem to be experimentally unfeasible. Therefore, other approaches have been developed to determine the PLC permeability in bone. Smit et al. (2002) obtained an estimate of the PLC permeability on the order of 10^{-22} m^2 based on the best fit between finite element predictions and data from streaming potential measurements. Beno et al. (2006) found the average measurements of PLC permeability in different species (chick, rabbit, bovine, horse, dog, and human) based on a microstructural model from Weinbaum et al. (1994) and measurements from the literature to vary from 10^{-20} m^2 to 10^{-23} m^2. The PLC permeability of human bone was estimated by Oyen (2008) to be around 10^{-24} m^2 using nanoindentation measurements and poroelasticity theory. The canine PLC was measured *in situ* by Gardinier et al. (2010), using step loading of intact bone and reported as 10^{-23} m^2.

The influence of the pore fluid behavior in the vascular porosity (PV) on the pore fluid behavior in PLC and vice-versa was analyzed in the hierarchical poroelastic model presented in Cowin et al. (2009). In that paper, the question of pore fluid movement due to cyclic loading and blood pressure from the perivascular region to the bone cells in the lacunae was addressed. The vascular porosity and the lacunar-canalicular porosity are interconnected and occupy the same three-dimensional volume of bone tissue. The PLC permeability can be measured without the effect of the PV if a bone sample that contains PLC only is obtained. With this objective in mind, the analytical solution of a saturated compressible poroelastic annular cylinder under an unconfined stress-relaxation test was developed (Gailani and Cowin, 2008). Predictions made by this model were compared to experimental stress-relaxation measurements obtained from isolated osteons *in vitro* (zero blood pressure), and the curve fitting between the model and experiment data was used by Gailani et al. (2009) to obtain the PLC permeability without the influence of the PV between 10^{-24} and 10^{-25} m^2. These estimates of PLC permeability exhibit a

broad variability, with values ranging from 10^{-17} to 10^{-25} m^2 (Table 3-1). Such a broad range of variability may be due to the different approach/model taken to determine the PLC permeability and/or by experimental challenges associated with the measurement of this small quantity.

The current contribution is an expansion of an ongoing effort (Cowin, 1999; Cowin and Mehrabadi 2007; Gailani and Cowin 2008; Cowin et al., 2009; Benalla et al. 2011; Gailani and Cowin 2011) aimed at the study of fluid transport in bone. In particular, the effect of the loading frequency on the PLC permeability has not been characterized before and it is physiologically relevant to the loading of bone during walking or running. The approach developed in Gailani and Cowin (2008) and Gailani et al. (2009) was extended to develop a frequency-dependent analytical model of the PLC permeability under harmonic loading (Benalla et al., 2011). A single osteon was idealized as a fully saturated porous annular cylinder subjected to an axial cyclic strain loading in order to determine formulas for the phase angle as a function of permeability and frequency. The analytical model developed in Benalla et al. (2011) was used as a basis of the experimental study presented here, in which an isolated osteon was subjected to an applied cyclic strain in order to determine the phase angle between the applied cyclic strain and the resultant stress, and thus evaluate the frequency dependence of the PLC permeability experimentally. Also, expressions for the storage modulus, the loss modulus, and the loss tangent were obtained. The variability of the storage modulus, the loss modulus and the loss tangent were analyzed with respect to frequency, permeability and porosity. The different plots of loss tangent and loss modulus expressed how the energy dissipation varied in a cyclically strained osteon while the curves for the storage modulus showed how the osteon samples responded as purely elastic at high frequencies. More importantly, the sensitivity study of the loss tangent using the derivative-based sensitivity and the numerical parametric sensitivity analysis showed that the porosity is

one of the most influential parameters of the model because it affects both the permeability and the effective elastic constants of the porous matrix material in bone.

4.2. Analytical model

4.2.1. Formulation of the loss tangent with respect to frequency

The analytical model in Benalla et al. (2011) considers a section of an osteon idealized as a fully saturated porous annular cylinder with compressible constituents and transverse isotropic symmetry subjected to a harmonic mechanical loading. The axial cyclic loading in the form of an applied strain is

$$\varepsilon(t) = \varepsilon_o e^{i\omega t}, \tag{1}$$

where ε_o and ω are the amplitude of the cyclic strain and its angular frequency, respectively. Under the same assumptions as in Cowin et al. (2009), but for zero blood pressure, Benalla et al. (2011) determined the governing equation of the pore pressure of an osteon leading to the frequency-dependent relationship between stress and strain in the osteonal model:

$$\sigma^*(t) = C^*(\bar{\omega})\varepsilon(t) \text{ with } \bar{\omega} = \frac{\omega r_o^2}{c}, \tag{2}$$

where $\bar{\omega}$ is the dimensionless angular frequency, r_o the outer radius of the osteon and c is the pore fluid pressure diffusion constant in the PLC (defined in Table 3-2) with $C^*(\bar{\omega})$ given by

$$C^*(\bar{\omega}) = C_{zz}^d + \frac{c_1 - c_2 K_{rr}}{c_3 K_{rr} + c_4} - \frac{c_5}{K_{rr}} \text{ and } C^*(\bar{\omega}) = C_o e^{-i\delta(\bar{\omega})} \text{ with } C_o = \frac{\sigma_o}{\varepsilon_o}, \tag{3}$$

C^* is a complex-valued modulus, whose magnitude and phase depend on the c_i (i=1-5) components:

$$c_1 = \left[\hat{C}^d_{rz} - \left(\frac{\hat{A}_r}{\hat{C}^d_{rr}}\hat{C}^d_{rz} - \hat{A}_z\right)\left(\frac{2a\bar{\Sigma}\ a,1}{1-a^2\ \sqrt{i\bar{\omega}}} + 1\right)\right] a_1, \tag{4}$$

$$c_2 = 2\hat{C}^d_{rz}\left[\hat{C}^d_{rz} - \left(\frac{\hat{A}_r}{\hat{C}^d_{rr}}\hat{C}^d_{rz} - \hat{A}_z\right)\left(\frac{a\bar{\Sigma}\ a,1}{\sqrt{i\bar{\omega}}} + \frac{1-a^2}{2}\right)\right], \tag{5}$$

$$c_3 = \frac{\hat{C}^d_{r\theta} + \hat{C}^d_{rr}}{2}\ 1-a^2\ , \tag{6}$$

$$c_4 = \left(\frac{\hat{A}_r - \hat{A}_z}{\sqrt{i\bar{\omega}}\Pi(a,1)} - \hat{A}_r\right)\Upsilon - a_1, \tag{7}$$

and

$$c_5 = \left(\frac{\hat{C}^d_{rz}}{\hat{C}^d_{rr}} - \frac{\hat{A}_z}{\hat{A}_r}\right)\left(\frac{2a\bar{\Sigma}\ a,1}{1-a^2\ \sqrt{i\bar{\omega}}} + 1\right)\hat{A}_z\Upsilon, \tag{8}$$

where C^d_{zz} is the axial elastic normal stress constant, K_{rr} is the intrinsic permeability in the radial direction, ε_o is the magnitude of the applied cyclic strain and σ_o is the magnitude of the average resultant stress in the osteon while $\delta(\bar{\omega})$ is the phase angle representing the angular delay between the applied strain and the resultant stress. All the components of the c_i coefficients in equations (4, 8) as well as the functions $\Pi(a,1)$ and $\bar{\Sigma}\ a,1$ were defined in Benalla et al. (2011), Tables (2) and equations (7, 12), respectively. Based on Euler's formula, the dynamic modulus C^* can be written as

$$C^*(\bar{\omega}) = C_o e^{i\delta(\bar{\omega})} = C_o \cos[\delta(\bar{\omega})] + iC_o \sin[\delta(\bar{\omega})] = C'(\bar{\omega}) + iC''(\bar{\omega}), \quad (9)$$

where $C'(\bar{\omega})$ is known as the storage modulus and $C''(\bar{\omega})$ as the loss modulus of the loaded osteon. From equation (9) the expression of the loss tangent is

$$\tan[\delta(\bar{\omega})] = \frac{C''(\bar{\omega})}{C'(\bar{\omega})} = \frac{\sin[\delta(\bar{\omega})]}{\cos[\delta(\bar{\omega})]}. \quad (10)$$

Formulas for the storage modulus and the loss modulus as well as their detailed calculations are presented in equation (29) and the appendix of Benalla et al. (2011), respectively. The ratio of the loss modulus over the storage modulus represents the loss tangent that an osteonal specimen exhibits when it is subjected to cyclic strain, equation (10).

4.2.2 Formulation of the PLC permeability with respect to loss tangent and frequency

In order to express the PLC permeability with respect to loss tangent and frequency, the equation (3) is reformulated as

$$K_{rr}{}^2(C_{zz}^d c_3 - c_2 - C^* c_3) + K_{rr}(C_{zz}^d c_4 - C^* c_4 - c_5 c_3) - c_5 c_4 = 0, \quad (11)$$

all the coefficients of the equation (11) are complex. Importantly, equation (11) can be separated into real and imaginary parts,

$$\left[\beta_1 K_{rr}^2\ \omega\ + \beta_2 K_{rr}\ \omega\ + \beta_3\right] + i\left[\alpha_1 K_{rr}^2\ \omega\ + \alpha_2 K_{rr}\ \omega\ + \alpha_3\right] = 0, \quad (12)$$

where β_n and α_n, (n = 1-3), are the coefficients of the two quadratic expressions in equation (12). Solutions of the quadratic expressions provide values of the PLC permeability with respect

to specified frequency values: C^* is a component of the coefficients in the quadratic equation (11). Using equations (9) and (10), C^* is expressed with respect to the loss tangent as

$$C^*(\bar{\omega}) = \frac{C_o}{\sqrt{\tan^2[\delta(\bar{\omega})]+1}}\left(1+i\tan[\delta(\bar{\omega})]\right). \quad (13)$$

Equation (13) permits the complex modulus C^* to be computed based on experimental measurements of the loss tangent at different loading frequencies. Measurements of this complex modulus as well as the evaluations of the porosity and elastic modulus of the osteon will be used to estimate the frequency-dependent permeability of the PLC in single human osteons.

4.3. Materials and Methods

4.3.1 Sample preparation

Approximately one hundred osteons were extracted from the mid-diaphysis of fresh frozen femurs from three human female donors provided by the National Disease Resource Center (NDRI, Philadelphia, PA). The age of the donors was 53, 62 and 75 years old and their medical history excludes any metabolic bone diseases or skeletal cancer. Femurs were kept at -80 °C prior to cutting a 10 mm length segment from the mid-diaphysis. Cortical segments were thawed, cleaned of soft tissue and bone marrow. Then, 0.5 mm thick cross-sections were machined from each segment using a low speed diamond saw (Buehler, Lake Bluff, IL) to obtain smooth and parallel surfaces. Phosphate Buffered Saline, PBS, was used as cooler and hydrant providing to the tissue a physiological ion concentration during all the cutting process.

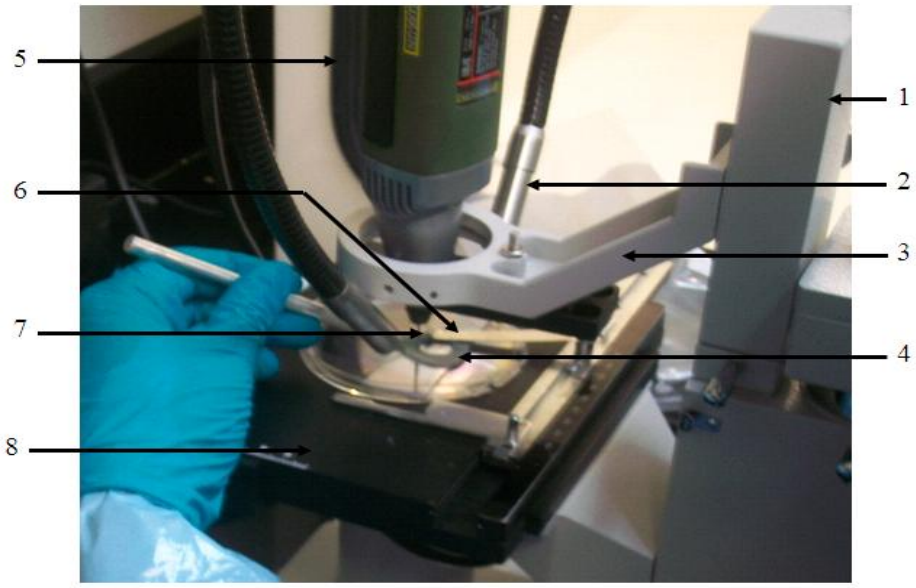

Figure 4.1: *Cutting of an osteon specimen, 1- microscope arm equipped with manual micrometer used to vertically move the drilling machine, 2- fiber optic illuminator, 3- microscope platform adapted as drilling machine holder, 4- 0.5mm width cross section from the mid-diaphysis of a human femur, 5- drilling machine, 6- bone section holder, 7- diamond core drill bit, 8- microscope stage.*

Immediately after the 0.5 mm thick cortical bone section was prepared, it was placed on the stage of the microscope and secured with a glass slide holder that prevented motion of the sample during the cutting. A small drilling machine (Proxxon, Greenville, WI) was adapted to the upper illuminator arm of an inverted biological microscope (XSB-1A, Hicksville, NY). Two flexible fiber optic high intensity illuminators (Fiber-Lite MI-152, Charlestown, WV) were placed on opposite sides of the drilling machine to illuminate the sample from the top surface, allowing improvement of the visualization of the osteon to be cut (Figure 4-1). The vertical position of the microscope arm can be manually adjusted to slowly move the drilling machine towards the sample. The drilling machine holds a 1 mm outer-diameter diamond drill bit (UKAM Industrial, Valencia, CA) which was aligned with the center of the microscope field of view. An osteon with a circular shape was identified using the microscope and placed at the center of the field of view, which was previously aligned with the diamond drill bit. The lowest rotary velocity was selected in the drilling machine, and the cutting of the osteon was performed by slowly and carefully moving the drilling machine downwards into the sample until the osteon was completely cut. During the whole isolation procedure the bone specimens have been kept hydrated with the PBS solution. Also, the inner and the outer diameters for each osteon were measured from the specimen's top view visualized with a Zeiss light microscope (Carl Zeiss microscopy, Monument, CO) and recorded with an Olympus DP72 high-resolution (4140 x 3096 pixels, Westmont, IL) digital video camera (Figure 4-2). The outer diameter of single osteons isolated using the miniature diamond drill bit ranged between 200 and 250 μm.

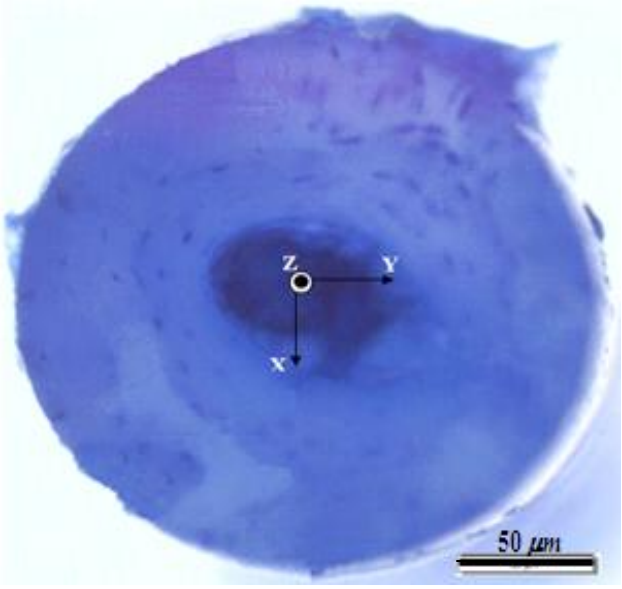

Figure 4-2. *Top view of an osteonal specimen with a centralized Haversian canal of 41 μm in diameter and an outer diameter of 218 μm*

4.3.2. Micromechanical loading

A small uniaxial cyclic loading apparatus was developed to measure the stress produced in a single osteon undergoing harmonic strain. The experimental device works under displacement-control using the nano-capture software (Physic Instruments, Auburn, MA) through a digital controller (E-709, Physic Instruments, Auburn, MA) connected in a closed loop to a preloaded piezoelectric linear actuator (P-841.10, Physic Instruments, Auburn, MA). The linear actuator has a maximal push/pull force of 5 *N* and a displacement resolution of 3 *nm*. From the top, the piezoelectric actuator is held with a Z-stage-9065 (New Focus, Irvine, CA) vertically aligned to a load cell, GS series gram force 10 g-sensor (Transducer Technique Inc, Temecula, CA), Figure 4-3. The osteon is placed over a stainless steel platen at the top of the load cell, immersed in PBS solution, and cyclically strained with the piezoelectric actuator under different frequencies ranging from 1 to 100 Hz. The load cell's output signal due to the applied strain is amplified using an instrumentation amplifier (INA 122, Texas Instruments, Dallas, TX) previously calibrated using standard weights to display the measured force in grams. Voltages were converted into digital signals using a data acquisition interface LABVIEW (V8.5, National Instruments, Austin, Texas). In order to perform a cyclic stress under specific frequencies, the user inputs the desired strain magnitude, 0.1% of sample height, with a specific frequency in the nano-capture software which then sends the commands through the digital controller to the linear actuator. The cyclic strains applied by the piezoelectric actuator as well as the resultant stresses acquired from the load cell were collected with LABVIEW and their normalized values were plotted with respect to each other in MATLAB (MathWorks, Natick, MA) in order to determine the phase angle from the slope of a linear fit model of the data.

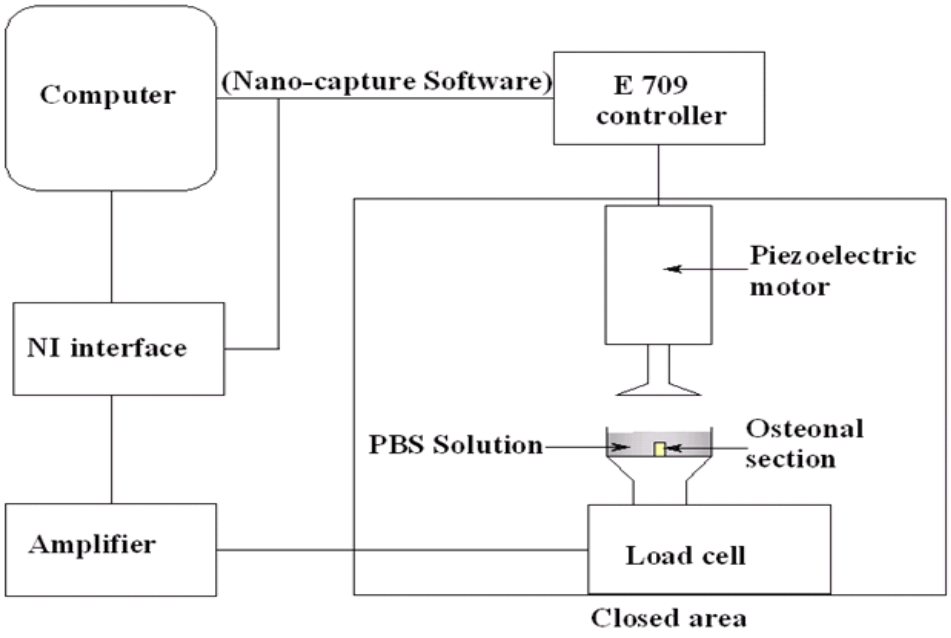

Figure 4-3a. *Schematic representation of micromechanical loading system*

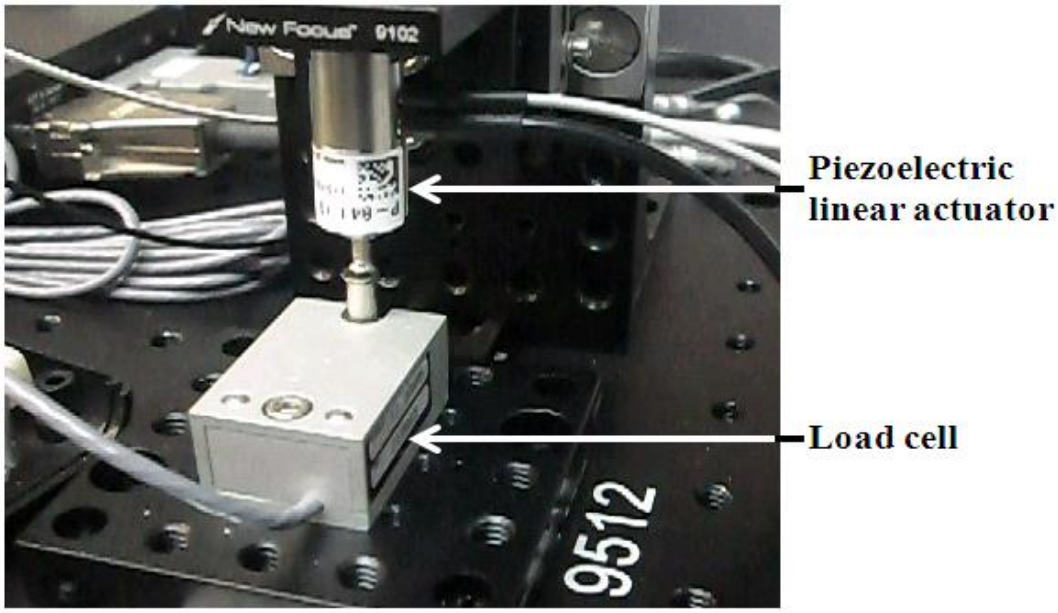

Figure 4-3b*. Photograph of uniaxial cyclic strain apparatus*

The study of the phase angle between the applied stress and resultant strain was performed based on their values normalized with respect to their magnitudes. The normalized applied stress and the normalized resultant strain were plotted with respect to time (Figure 4-4a). The closeness of the two curves reflects the small size of the phase angle between the applied strain and the resultant stress. The normalized resultant stress is then plotted versus the applied normalized cyclic strain (Figure 4-4b). The slope of a linear fit model of the data in Figure 4-4b characterizes the loss tangent

Experiment 1: *Effect of osteon's storage time on the loss tangent measurements*

The mechanical properties of post mortem fresh frozen tissue change as a function of the time elapsed after being thawed for experimental testing. Since the PLC permeability will be determined by curve fitting experimental measurements of the loss tangent in thawed samples of fresh human bone, the extent to which the freshness of the specimen affects such measurements needs to be evaluated. For this purpose, we carried out an experiment with the objective of determining the effect of time between sample preparation and the measurement of the loss tangent at a single frequency value. For this first test, two subsets of osteon specimens (n = 9/group) were cyclically loaded with a magnitude of 1000 με and 1Hz frequency. The first set was loaded five times every sixty minutes, hereafter designated as the *hourly* group. The second set was loaded every 24 hours for five days, and henceforth named as the *daily* group. Samples in the *daily* group were stored in PBS at -20 ^{o}C, and thawed before testing every day. Data from these tests determined the time window between the cutting and mechanical loading of the

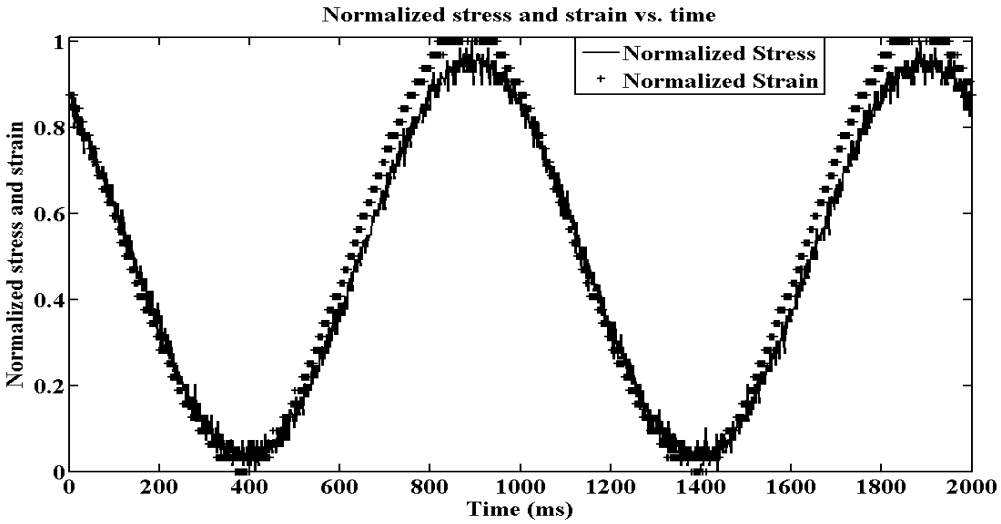

Figure 4-4a. *Plot of the normalized applied strain and the normalized resultant stress with respect to time. The magnitude of the applied strain was 1000 με and the frequency was 1Hz*

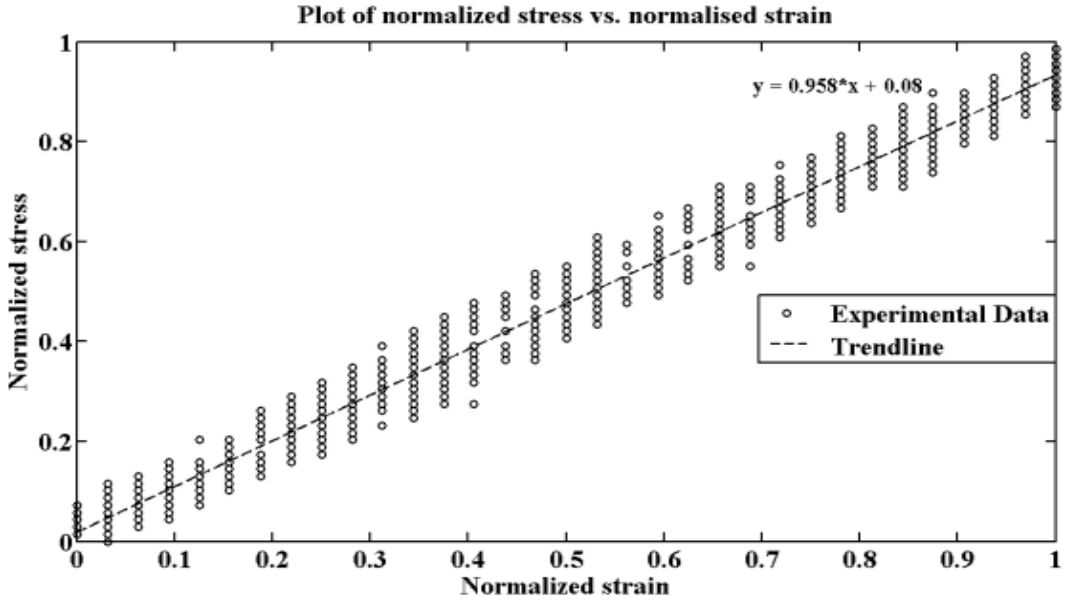

Figure 4-4b. *Plot of the normalized resultant stress versus the normalized applied strain. The magnitude of the strain applied in this loading was 1% at a frequency of 1 Hz. The slope of the linear fit model determines the value of the loss tangent during the related loading.*

osteons that may be permitted without their properties being changed due to the time lapsed after their isolation.

Experiment 2: *Measurement of osteon's loss tangent at different frequencies*.

A second experiment was performed to determine the loss tangent and intrinsic PLC permeability, as well as the changes in PLC permeability as a function of frequency. Experimental data on loss tangent were collected as a function of frequency in a larger set of twenty samples per femur that were used to estimate the intrinsic permeability of each osteon in the lacunar-canalicular domain based on curve fitting of data to the analytical model over a range of loading frequencies. Specifically, the cyclic strain loading was performed on the sixty osteons at twelve different frequencies, {1, 2, 3, 5, 8, 10, 15, 20, 30, 50, 70, 100 Hz} in order to have close recordings of the loss tangent experimental data along the physiological range between 1 and 100 Hz. The time duration of each loading procedure was 2 minutes approximately and all experiments were performed during the weekends because of the high sensitivity of the loading apparatus to external vibrations.

For each osteon, values of the loss tangent were collected at the twelve frequencies based on the slope of the linear fit between the normalized resultant stress versus the normalized applied strain data (Figure 4-4b). The lacunar-canalicular porosity, elastic modulus, Haversian canal radius, and cement line radius were derived for each osteon based on high-resolution micro-CT (μCT) images, microscope images of the osteons and a structural model of the lacunar-canalicular morphology, as described in the following sections. Such parameters were used in the curve fitting between the analytical model and the loss tangent experimental data for each specimen.

4.3.3. μCT scanning

After micromechanical testing, osteons were scanned using a high resolution SkyScan μCT system. An acrylic holder was fabricated to contain fresh osteon samples immersed in PBS during the scanning that lasted 1h and 45 minutes. Images were acquired using a 10 MP digital detector, 10W power energy (100KV and 100μA). In order to minimize beam hardening artifacts, an aluminum filter of 0.5 mm thickness was used along with a correction algorithm (Skyscan Nrecon Software). X-ray projections were generated from the sample every 0.3 degrees, obtaining 680 consecutive views with 2.1 μm image pixel size. Five exposures by projection (1767ms exposure time) were used to produce high-contrast, low-noise images. A system alignment procedure and flat field calibration were performed prior to the scanning sequence in which the acquisition field was corrected for possible pixel defects in the digital detector using bright and dark fields.

A modified back-projection reconstruction algorithm (NRecon, V. 1.6.1.2) included in the SkyScan acquisition system was used to generate cross-section images from the planar X-ray projections. Throughout the reconstruction procedure, images were optimized using a standard post-alignment compensation algorithm, eliminating misalignment artifacts. Images were also treated using smoothing filters (kernel=1) with a Gaussian window, Ring Artifact Correction (=15) and Beam Hardening Correction (10%). All the reconstruction parameters were applied identically to all scans, with the exception of the post alignment compensation, the only parameter that should be set uniquely for each scan, which did not compromise comparative measurements.

For measurement of local tissue mineral density (TMD), a Hounsfield Units (HU) calibration procedure was performed first in the software CT-Analyzer v. 1.10 (CTAn). A volume of interest (VOI) within the calibration scan was selected containing only water. The average grey level for this VOI was obtained in CTAn, which corresponded to 0 HU, and gray level of 0 corresponded to -1000 HU. The calibration scan also contained two mineralized phantoms (0.25 and 0.75g/cm^3 of hydroxyapatite, solid rod of 2 mm diameter) that would be used for TMD calibration. A volume of interest was selected for each phantom, integrating over several images, and the measured HU density values for each phantom were then used to transform HUs into bone mineralization densities in gHA/cm^3 (grams of hydroxyapatite per centimeter cube). Cortical bone was segmented using a global thresholding procedure to exclude the volume corresponding to the lacunae and the Haversian canal, and the computation of the density corresponded then to the Tissue Mineral Density (TMD) in the PLC domain. In addition to the TMD, the total number of lacunae, the volume of the lacunae and the dimensions of each osteon were determined. All these parameters were evaluated using CTAn. Also, µCT images were used to determine the alignment of the Haversian canal at the center of the sample and the absence of density corresponded then to the Tissue Mineral Density (TMD) in the PLC domain. In addition to TMD, the total number of lacunae, the volume of the lacunae and the dimensions of each osteon were determined. All these parameters were evaluated using CTAn. Also, µCT images were used to determine the alignment of the Haversian canal at the center of the sample and the absence of cracks or inhomogeneities (i.e. resorption areas) that might increase the sample's permeability (Figure 4-5). Machined osteons that did not meet these requirements were discarded.

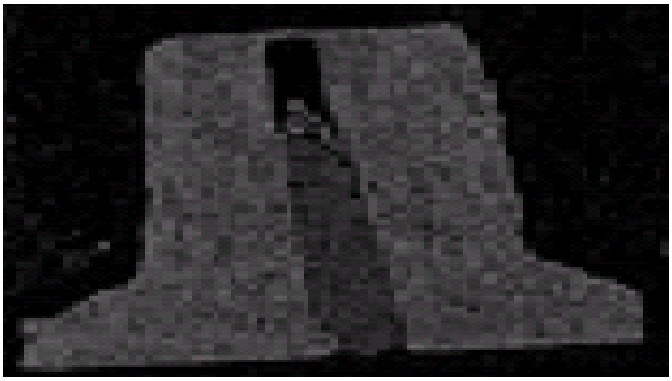

Figure 4-5a. *Sectional view of an osteon specimen following the XZ plan. The dark line in the middle represents the Haversian canal.*

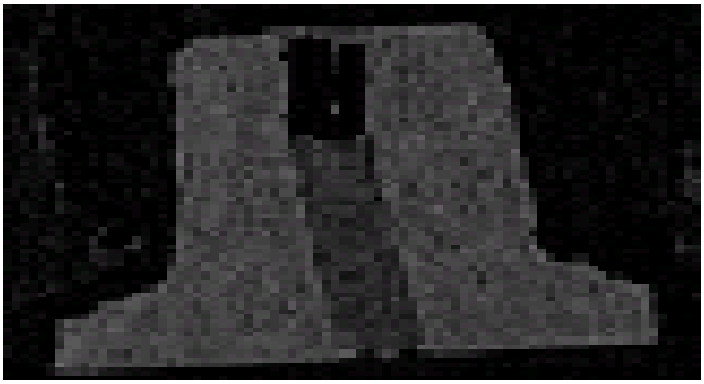

Figure 4-5b. *Sectional view of an osteon specimen following the YZ plan. The dark line at the bottom represents an inclined end of a Volkmann canal and the beginning of a Haversian canal.*

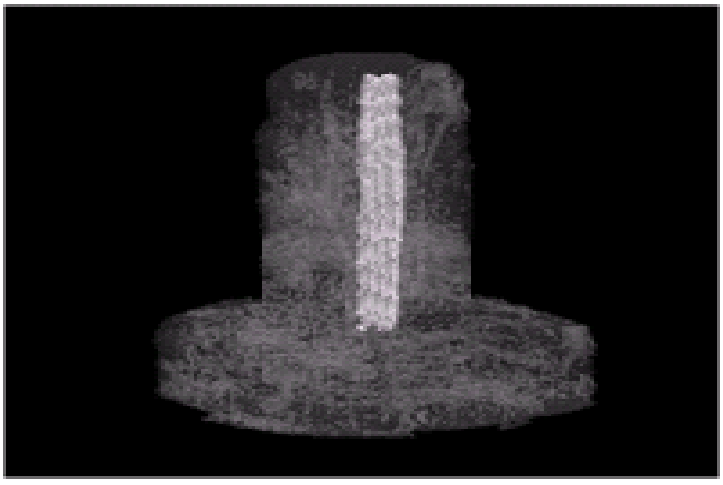

Figure 4-5c. *3D reconstruction of an osteonic sample from micro-CT scanning images. The white band in the middle represents the Haversian canal.*

4.3.4. Determination of the Lacunar-Canalicular Porosity (PLC)

The sensitivity study performed in Benalla et al. (2011) indicated that the PLC, $\phi_{PLC}(\%)$, was the most influential parameter in the determination of the permeability in the lacunar-canalicular domain. Therefore, it was decided to estimate the PLC individually for each tested osteon. The PLC was calculated as the sum of the lacunar, $\phi_{Lac}(\%)$, and the canalicular, $\phi_{Can}(\%)$, porosities, thus neglecting the mineral/collagen porosity. The lacunar porosity was assessed directly from the μCT scanning by use of the 3D analysis that gave the total volume of lacunae, which was divided by the volume of the specimen. The canalicular porosity was calculated based on a structural model. In this structural model, five parameters were used. The volume of the osteonal specimen, V_s (mm^3), the total number of the lacunae, N_{Lac}/mm^3, the inner and outer diameter of an osteon, r_i and r_o (μm), were derived from the μCT scanning while the average distance between two neighboring lacunae was evaluated based on the parallelepiped periodic unit cell (PPUC) that surrounded the lacuna. The side dimension, L (μm), of PPUC represented also the distance between two neighboring lacunae, center to center,

$$L = \left(\frac{V_s}{N_{Lac}} \right)^{1/3}. \tag{15}$$

Based on equation (15), the average length of the canaliculi, L_{Can} is

$$L_{Can} = L - 2r_{Lac}, \tag{16}$$

where r_{Lac} is the average radius of lacunae in the radial direction. In Beno et al. (2006), the average value of the radius of lacunae in the radial direction is around $r_{Lac} = 2.5\,\mu m$.

Finally, the two last parameters, the diameter of the lacunae and the number of canaliculi emanating from each lacuna were obtained from literature. You et al. (2004), by means of electron photomicrographs, evaluated the diameter of the canaliculi in the range of 259 ± 129 μm while Beno et al. (2006), based on light microscopic images from Remaggi et al. (1998), found the average number of canaliculi emanating from each lacuna to be around 62. The final formula for the canaliculi porosity, ϕ_{Can}, then is

$$\phi_{Can} = \frac{62\ 129.5^{\ 2}\pi L_{Can}}{V_s}. \tag{17}$$

4.3.5. Elastic constants of the tissue mineralized matrix

Based on μCT images and 3-D analysis of reconstructed volumes, the tissue mineral density of each scanned osteonal specimen was obtained. Using the equation (14) from Wagner et al. (2011),

$$\log_{10} E_r^m = -8.58 + 4.05\log_{10}\left\{\frac{400}{1+\ 504/\rho_{HA}}\right\}, \tag{18}$$

where ρ_{HA} is the tissue mineral density obtained from the μCT. The Young's modulus of the matrix material in the radial direction, E_r^m, was evaluated from equation (18). In the axial direction, the Young's modulus of the matrix material, E_z^m, was calculated based on a requirement that the matrix of the 4th order transversely isotropic elasticity tensor be symmetric,

$$\frac{E_r^m}{\nu_{rz}^m} = \frac{E_z^m}{\nu_{zr}^m}, \tag{19}$$

where values for ν_{zr}^m and ν_{rz}^m were adopted from Cowin et al. (2009) and represent the Poisson's ratios. Mean values of the Young's moduli for sixty osteons are summarized below (Tables 4-1). The drained elastic constants were defined with superscript *d*, E_i^d $(i = r, z)$, and calculated based on the lacunar-canalicular porosity and the Young's moduli of the matrix material (Benalla et al., 2011; equation 33).

4.3.6. Determination of the PLC permeability

The PLC permeability was determined from the curve fitting of the analytical model in Benalla et al. (2011) against experimental data of the loss tangent associated with a cyclically loaded osteon. Equation (5) represented the analytical model of the loss tangent that the osteon specimen exhibits under cyclic loading based on the traditional theory of poroelasticity (Biot 1941; 1955; Rice and Cleary 1976; Thompson and Willis 1991; Cowin and Doty 2007; Cowin and Mehrabadi 2007; Gailani and Cowin 2008; Cowin et al. 2009). The curve fitting toolbox in MATLAB was used to import the model parameters and create a custom function based on the analytical model that depends essentially on the permeability. This custom equation was then fitted to the experimental data using a least-squares algorithm built in the toolbox. The only parameter that has not been assigned a value before the actual curve fitting process was the PLC permeability K_{rr}.

4.3.7. Statistical Analysis

Descriptive statistics were obtained for porosity of the lacunae (ϕ_{Lac}), total number of lacunae in the osteon specimen (N_{Lac}), porosity of the canaliculi (ϕ_{Can}), porosity of the lacunar-canalicular domain (ϕ_{PLC}), tissue mineral density ($\rho HA/cm^3$), Young's modulus of the matrix tissue in the radial direction (E_r^m), Young's modulus in the axial direction (E_z^m) and PLC permeability (K_{rr}). Repeated measures ANOVA and Tukey's multiple comparison tests were performed to identify differences in loss tangent measured at different time points, as well as for measurements of PLC permeability at different frequencies. All tests were performed using Prism5 statistics software package (GraphPad Software Inc.) with a significance level of $p < 0.05$.

4.4. Results

4.4.1. Effect of time duration and storage condition on the osteon specimen

In order to determine the effect of the storage condition and the time duration between the cutting and the loading of the osteon, changes on loss tangent on both hourly and daily groups were analyzed. The percentage change on loss tangent as a function of time is shown for the hourly and daily groups in Figures 4-6 and 4-7, respectively. Data is shown as mean value and the error bars represent standard deviation. No significant differences were found on loss tangent measurements within the first three hours after isolation of osteons. However, a small but statistically significant change on loss tangent was found when measurements were performed at

4h and 5h after the samples were extracted. The decrease on loss tangent at 4h and 5h was smaller than 1% when compared to the first measurement at 1h.

Analysis of changes in the loss tangent as a function of time for the daily group shows a clear decrease of the loss tangent on measurements performed every 24h (Figure 4-7). This observation was corroborated by statistically significant differences when measurements at each time point were compared using repeated measurements ANOVA. The daily change in the loss tangent was found to be less than 1% approximately, and counted for almost 5% decrease at the fifth day of testing. The rate of change in the loss tangent seems to decrease between 4 and 5 days after isolation of samples. However, to confirm this observation it would be necessary to extend the period of measurements beyond 5 days. Overall, analysis of the hourly and daily results shown in Figures 4-6 and 4-7 demonstrate a small change of loss tangent over five hours when compared to five days.

The effect of hourly and daily changes of loss tangent on the PLC permeability was computed to determine whether such changes represent a significant change on PLC permeability or not. A change of 1% on loss tangent observed in the hourly group resulted in a change on PLC permeability of less than 0.1%, while the 5% change on loss tangent from the daily group produced a change on PLC permeability of 10% approximately. Therefore, testing of osteons in the second experiment of this study was performed within 5 hours to avoid any significant change on the PLC permeability due to the elapsed time after osteons isolation.

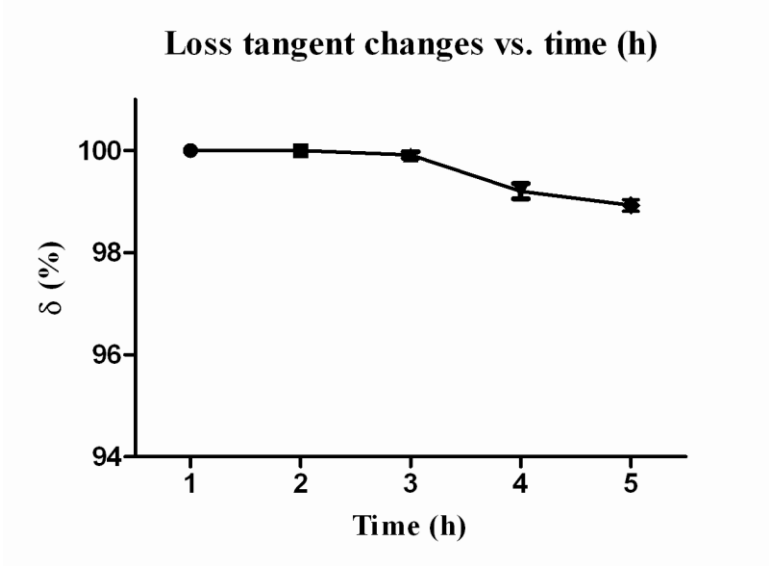

Figure 4-6. *Plot of changes* in the *loss tangent versus time for a period of five hours. Nine osteons were harvested from three different human femurs and cyclically strained with a magnitude of 1000 με at 1 Hz. The analysis of the curve behavior shows a decrease of 0.85% of the loss tangent over five hours after the cutting. The very small error bars represent the standard deviation of the loss tangent percentage.*

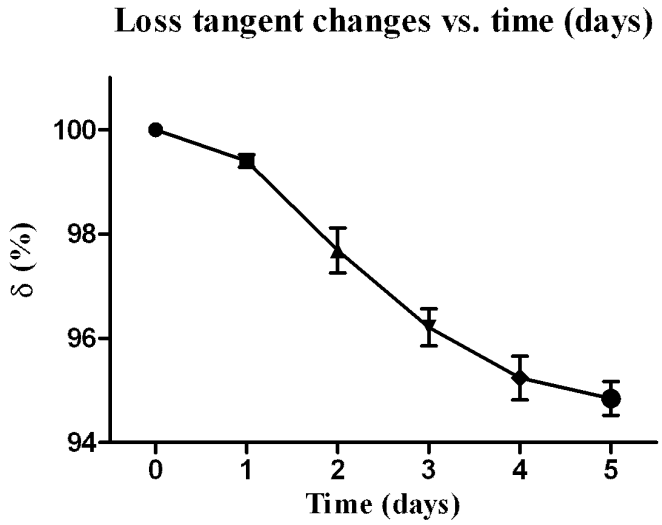

Figure 4-7. *Plot of changes* in the *loss tangent versus time for a duration of five days. The nine osteon were harvested from three different human femurs. The samples were cyclically strained with a magnitude of 1000 με at 1 Hz. The analysis of the curve behavior shows a decrease of approximately 5% at 5 days after the cutting of the osteon. The error bars in the plot represent the standard deviation of data.*

4.4.2. Determination of the analytical model parameters

Model inputs such as the PLC, Young's moduli, inner and outer radius of the osteon were individually determined for each osteon based on μCT scanning and structural model. Values for the PLC and the matrix material elastic constant are presented in Table 4-1. The inner and outer radii of the isolated osteons were determined based on μCT scanning and light microscopy (Figure 4-5). The average value of the inner and outer radius for the isolated osteons (mean ± standard deviation) were 41.5 ± 19 μm and 76 ± 32.5 μm, respectively. Other parameters such as the viscosity $\mu = 1\ cP$, compressibility of the interstitial fluid $K_f = 2.3\ GPa$, Poison's ratios $\nu_{rz} = 0.255$ and $\nu_{zr} = 0.312$ were considered as constants and adopted from Cowin et al. (2009).

4.4.3. Loss tangent vs. frequency

The PLC permeability value (mean ± SD) in the radial direction for the sixty loaded osteons based on the curve fitting of the analytical model, equation (5) versus the experimental data of the loss tangent (Figure 4-8) was found to be $K_{rr} = (6.15 \pm 0.83) 10^{-22} m^2$, (Table 4-1). Concerning the statistical changes, No significant differences were detected in the loss tangent at the several frequencies analyzed within 1 and 3Hz. The loss tangent was found significantly different at 5Hz and higher frequencies when compared to 1Hz. Importantly, the variance of loss tangent measurements decreases as the frequency increases. This change on data variance was important to find no differences on loss tangent within the frequency range {1-3Hz}, as well as the clear differences at 5Hz and higher frequencies.

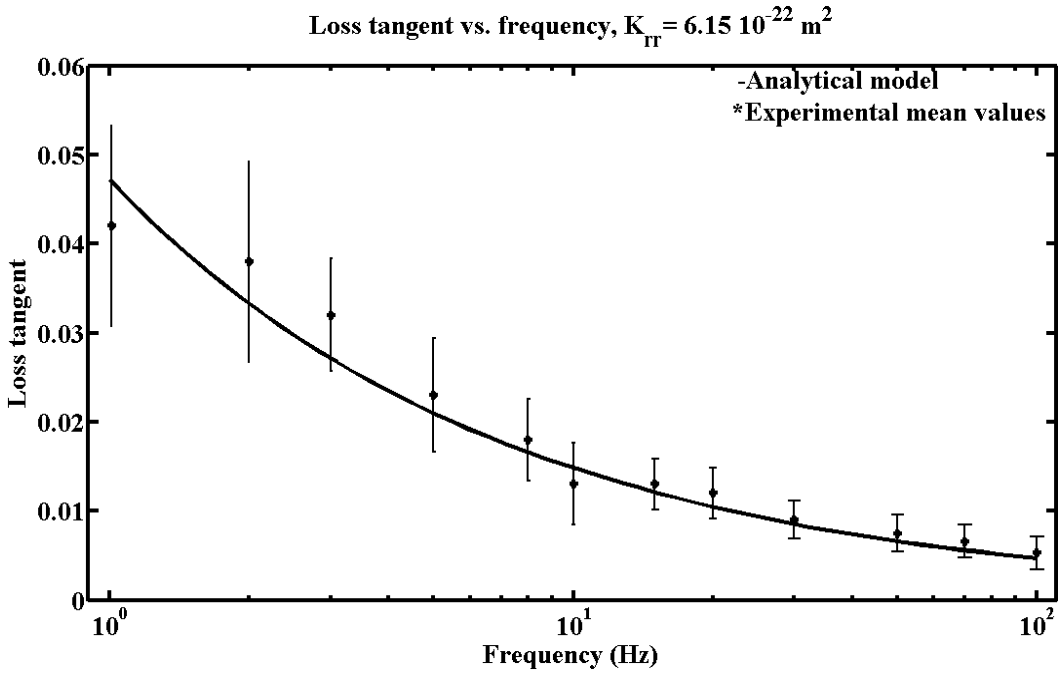

Figure 4-8*. Curve fitting of the analytical model and experimental data of the loss tangent to evaluate the intrinsic permeability in the PLC,* $K_{rr} = 6.04\,10^{-22}\,m^2$*. The curve fitting shows a good agreement in high frequencies and less agreement at lower frequencies.*

	ϕ_{Lac} (%)	N_{Lac} $1/mm^3$	ϕ_{Can} (%)	ϕ (%)	ρ_{HA} (g/cm^3)	E_r^m (GPa)	E_z^m (GPa)	K_{rr} $(10^{-22}m^2)$
Mean Value	3.40	82951	5.77	9.29	0.91	15.29	18.72	6.15
Std. Deviation	0.64	13371	0.89	1.24	0.06	1.312	1.612	0.83

Table 4-1*. Mean values along with their standard deviation for model parameters and PLC permeability determined from sixty osteons harvested from three femoral bones.*

4.4.4. Variability of the PLC permeability with respect to frequency

The values of PLC permeability were calculated for sixty osteons and plotted versus frequency (Figure 4-9) based on solving the quadratic equation (12). The curve of the PLC permeability illustrates a progressive linear decrease with respect to frequency at a rate of -3 10^{-24} m^2/Hz. The intercept at the origin, or zero frequency, represents the intrinsic frequency, which as reported above, was found to be 7.63 10^{-22} m^2. The PLC permeability values (mean ± SD) ranged between $7.51 \pm 0.62\ 10^{-22} m^2$ at 1 Hz and $4.82 \pm 0.11\ 10^{-22} m^2$ at 100 Hz. The variability of the PLC permeability with respect to frequency shows no significant differences among tested frequencies smaller than 20Hz. However, significant changes on PLC permeability were found at 30 Hz and higher frequencies when compared to the PLC permeability at 1 Hz.

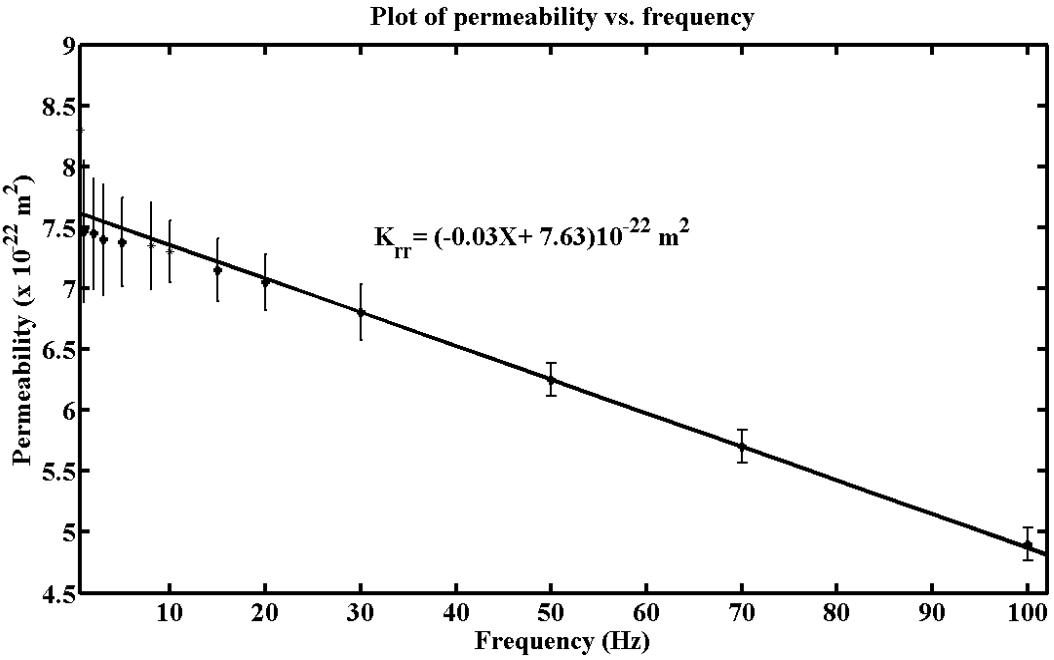

Figure 4-9*. Plot of the PLC permeability versus frequency. Values of PLC permeability were calculated using equation (12), PLC, Young's elastic modulus and loss tangent measurements acquired for each osteon loaded at different frequencies.*

4.4.5. PLC permeability and loss tangent with respect to PLC

4.4.5.1. PLC permeability with respect to PLC

The analysis of the PLC permeability with respect to the lacunar-canalicular porosity exhibits a linear behavior (Figure 4-10). Experimental data of the PLC permeability and the porosity plotted in the graph were assessed from the sixty loaded osteons based on curve fitting of the analytical model (Benalla et al., 2011) versus experimental data of loss tangent and μCT scanning as well as the structural model, respectively. The equation of the linear fit model of the data is $K_{rr} = (1.54\phi - 0.14)10^{-22}\ m^2$ and the correlation is R = 95% with $p < 0.05$.

4.4.5.2. Loss tangent with respect to porosity

The plot of the loss tangent with respect to the PLC, the most highly sensitive parameter of the analytical model parameters, displays a linear behavior in the narrow range of porosity we investigated. Both the loss tangent and the PLC values presented in the plot were obtained from the sixty loaded osteons based on cyclic loading and μCT scanning as well as the structural model, respectively. The correlation in this plot is R= 75.6% and the equation of the linear fit model of the data is $\tan\delta = 0.0029\phi + 0.013$

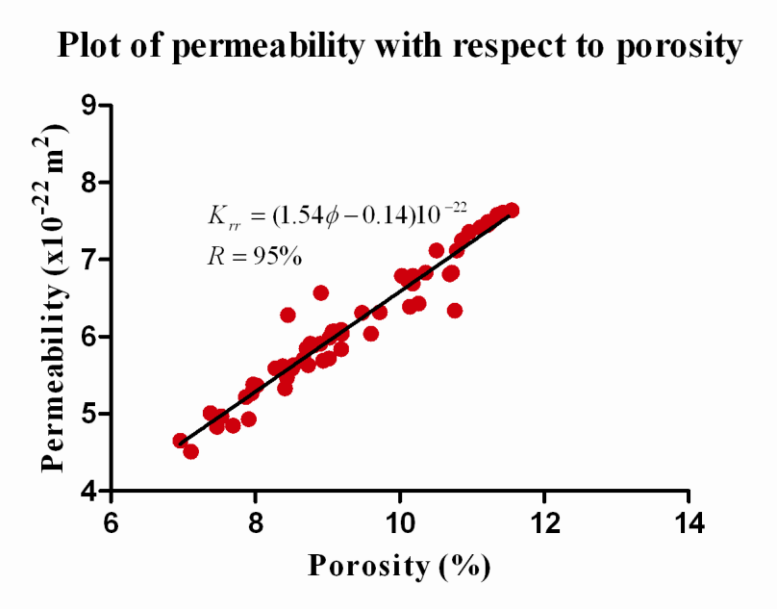

Figure 4-10. *PLC permeability versus PLC. Data are obtained from the sixty loaded osteons*

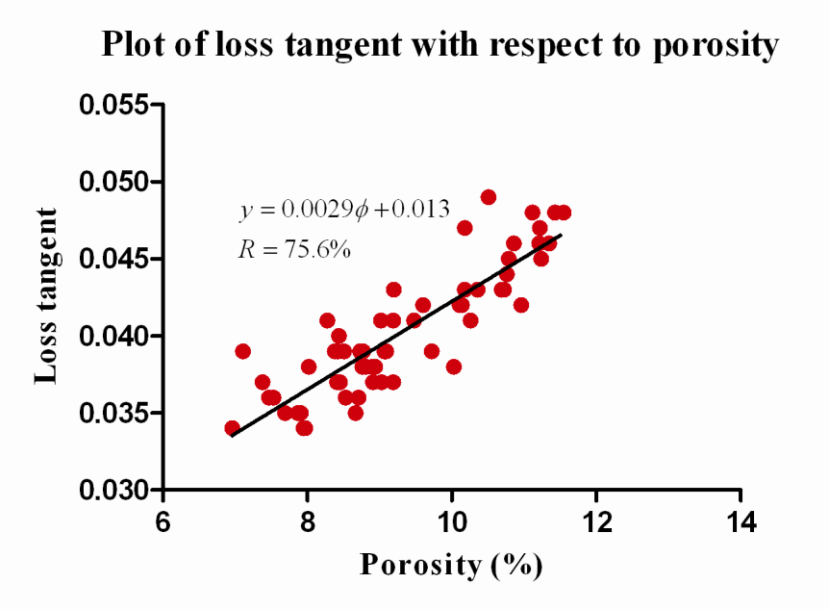

Figure 4-11. *Experimental data of the loss tangent versus the PLC. The loss tangent is obtained based on experimental data of the sixty loaded osteons with a magnitude of 1000 $\mu\varepsilon$ in a range of frequency between 1 and 100 Hz.*

4.5. Discussion

The objective of this study was to determine accurately the PLC permeability of human cortical bone. The PLC permeability cannot be determined directly in the conventional manner first employed by Henri Darcy; it must be done indirectly because the porosity in the lacunar-canalicular domain is intertwined with the PV and specimens with extremely small domains containing only the PLC must be isolated. The PLC permeability in previous studies has been determined based on a combination of analytical and experimental studies. We have followed a similar approach in the present study, an approach in which the PLC permeability was derived from curve fitting of the poroelastic model developed in chapter 3 and experimental measurements of key model parameters such as the loss tangent, PLC, tissue matrix material modulus. In contrast to the indirect determination of the PLC permeability, the loss tangent in the PLC domain was obtained from direct measurements of strain and stress in the bone samples.

The preparation of the specimen is of importance because the determination of the PLC permeability should be performed on the PLC domain only. Any intertwining of the PV with the PLC will increase the value of the PLC permeability. The importance of isolating a section of an osteon stems from the fact that it represents a specimen that contains the PLC alone (Figure 3-2). Gailani et al. (2009), Dong et al. (2005), Frasca et al. (1976) and Ascenzi et al. (1959, 1968, 1985 and 1994) presented efficient procedures to cut the osteon; however, the methodology employed and reported in this thesis is more direct in the sense that the whole procedure can be performed in two steps, and more accurate because the cutting procedure can be simultaneously observed and followed with the microscope.

The freshness of the specimen is one of the most important factors for improving the accuracy in determining the PLC permeability. Bone tissue loses some of its freshness with time

and storage conditions, despite of all precautions one can take. However, keeping the bone specimens hydrated with physiological solution and performing the experiment immediately after the isolation of the sample is critical to acquire PLC measurements *ex vivo* that could be as close as possible to the *in vivo* condition. Plots of the loss tangent obtained from loaded osteons versus time show a decline of less than 1% for a time duration of five hours while it reaches 5% for a period of five days under the same storage conditions. The 1% decrease of the loss tangent doesn't affect the final result of the PLC permeability while the 5% decrease causes a reduction of 10% on the level of the final value of the PLC permeability. In this study we have made every effort to preserve the freshness of our osteons by storing them immersed in PBS solution and loading them within five hours after the cutting.

The sensitivity study of the various model parameters indicated that the PLC and Young's modulus of the tissue material were the most influential on our indirect measurement method of the PLC permeability. Therefore, instead of adopting a single value of PLC and Young's modulus of the tissue matrix material from the literature, an effort was made to determine these parameters for each tested osteon. The individual determination of these parameters for each osteon increased the accuracy in determining the PLC permeability. The PLC $(9.29 \pm 1.24)\%$ and the Young's moduli of the matrix material in the radial direction, $(15.29 \pm 1.31)\ GPa$, as well as the axial direction, $(18.72 \pm 1.61)\ GPa$, were found in close agreement with values reported by Goulet et al. (2009) and Espinoza et al. (2009), respectively.

In this study, the value of the lacunar-canalicular permeability is in reasonable agreement with previous theoretical and experimental publications. The value of the PLC permeability obtained in this work, $(6.12 \pm 0.83)10^{-22}\ m^2$, is located in the middle range of theoretical values

(10^{-17} -10^{-18} m^2, Kameo et al. 2010; 10^{-20} - 10^{-23} m^2, Beno et al. 2006) and the experimental measurements (10^{-22} m^2, Galli and Oyen 2009; 10^{-24} - 10^{-25} m^2, Gailani et al. 2009). The standard deviation of the PLC permeability measurements in our study, $0.83\,10^{-22}\,m^2$, represents a percentage of variability of 13.6%. The percentage illustrates the closeness of the PLC permeability values obtained from all the samples. The improved methodology in cutting the osteon samples as well as the individual study of each osteon in terms of curve fitting and model parameters determination played an important role in the convergence of the results, notably the values of the PLC permeability. A general overview of the literature associated to the determination of the PLC permeability suggests two main reasons that play an important role in the wide span of the PLC permeability in previous studies. The first reason is related to the cutting of the osteon. In order to measure the PLC permeability only, the PV should not be included in the sample to be tested. The second reason is associated with the material properties of the specimen. In most previous works, the material properties of the bone tissue matrix were adopted from literature and generalized to all the bone samples. The adopted values may be close to the real ones; however, certain parameters may present a high degree of sensitivity to the analytical model, which causes a significant variation on the determination of the PLC permeability. In summary, the accuracy in determining PLC permeability of human bone was improved in this study due to (a) the analysis of the sensitivity of key parameters on the analytical model, (b) the exclusion of any PV influence in our specimens, (c) the freshness of samples, (d) the measurement of key material properties affecting the intrinsic PLC permeability, (e) the curve fit of the analytical model in Benalla et al. (2011) of the loss tangent performed independently for each sample.

The second goal of this study was to investigate the dependence of the PLC permeability with respect to frequency. The novel finding of the frequency dependence of the PLC permeability shown in Figure 4-9, illustrates the behavior of permeability within a range of physiological frequency. The PLC permeability was solved numerically at the twelve frequencies based on the osteon model parameters and the experimental data of the loss tangent. Note that this curve shows that the variability of the PLC permeability changes linearly from 7.51 10^{-22} m^2 to 4.82 10^{-22} m^2 when the frequency increases from 1 to 100 Hz, at a rate of -3 10^{-24} m^2/Hz. The inverse relationship between PLC permeability and frequency is considered to be mainly related to the decrease of the loss modulus and the increase of the storage modulus in the matrix material (Figures 3-3 and 3-4). Zhang et al. (1998) determined the relaxation time in the PLC permeability to be around 4.9 ms, which corresponds in terms of frequency to 204 Hz. Based on that, it is expected that the decreasing rate of the PLC permeability will increase after 204 Hz because the PLC will not have enough time to relax entirely. The incomplete relaxation of the PLC will cause the interstitial fluid to lower its velocity between all the lacunae and through the canaliculi which will amplify the decreasing rate of the PLC permeability after 204 Hz.

The error bars calculated, based on the standard deviations in both plots of loss tangent and the PLC permeability versus frequency, Figures 4-8 and 4-9, respectively, are larger at low frequency and keep decreasing as the frequency increases. The variability of the error bar size in both curves can be explained based on the behavior of the storage modulus and the loss modulus with respect to frequency in Figures 3-3 and 3-4, respectively. The plot of the storage modulus with respect to frequency in Figure 3-3 shows how the stored energy increases, while the curve of the loss modulus in Figure 3-4 illustrates how the lost energy as well as the damping energy decrease in a loaded osteon as the frequency increases. Therefore, the loaded osteon tends to

become purely elastic with increasing frequency, which reduces the size of the error bars and increases the agreement with model fit in Figures 4-8 and 4-9.

The sensitivity study showed that the lacunar-canalicular porosity is one of the most influential parameters of the model inputs. Therefore, the variation of the PLC permeability and the loss tangent with respect to the lacunar-canalicular porosity were also studied. We found a strong relationship between the permeability and the PLC as well as between the loss tangent and the PLC for the sixty loaded osteons. The high correlation, R= 95%, appearing from the plot of the permeability with respect to porosity (Figure 4-10) shows that there is a linear relationship between the two parameters. In this case, the equation of the linear fit model of the data, $K_{rr} = (1.54\phi - 0.14)10^{-22}\, m^2$, represents an empirical formula relating the permeability to the porosity in the lacunar-canalicular region. However, the correlation, R= 75%, related to the plot of the loss tangent versus the PLC is less than the one between lacunar-canalicular permeability and PLC, and thus illustrates that the loss tangent is not dependent on the lacunar-canalicular porosity alone and that other parameters such as the elastic constants, inner and outer radius of the osteon are also involved.

Some limitations of this study are related to three assumptions. First, the idealization of the osteon and the Haversian canal as pure cylinders is not fully correct. Actually, the shape of the osteon and the Haversian canal may not be purely circular and their radii may slightly change from bottom to top. However, the small height of the osteon sections, 500 μm, minimizes the inaccuracy of this assumption. Second, in the evaluation of the canalicular porosity, the canaliculi are considered as straight tubes relating the lacunae with each other and with the Haversian canal while some of these canaliculi, especially the ones emanating from the summit or the underneath of the lacunae, radiate along the vertical axis of the lacunae before they bend

horizontally following the radial direction (Marotti 1996). Fortunately, only few canaliculi from the bottom and the top of the lacunae take that bended shape, which reduces their effects. Finally, the third limitation is related to the assumption considering the outer boundary of the osteon impermeable. The permeability of the cement line, if it exists, should be negligible comparing to the one in the inner wall separating the PLC and the Haversian canal.

References

Ascenzi A, Baschieri P, Benvenuti A (1994) The Torsional Properties of Single Selected Osteons. J. Biomech., 27(7): 875–884.

Ascenzi A, Benvenuti M, Mango F, Similia R (1985) Mechanical Hysteresis Loops From Single Osteons: Technical Devices and Preliminary Results. J. Biomech. 18(5): 391–398.

Ascenzi A, Bonucci E (1968) The Compressive Properties of Single Osteons. Anat. Rec. 161: 377–391.

Ascenzi A, Fabry C (1959) Technique for Dissection and Measurement of Refractive Index of Osteons. J. Biophys. Biochem. Cytol. 6: 139–143.

Benalla M, Cardoso L, Cowin SC (2011) Analytical basis of the lacunar-canalicular permeability of bone using cyclic loading. Biomech. Model. Mechanobiol. Accepted: 14 September 2011.

Beno T, Yoon YJ, Cowin SC, Fritton SP (2006) Estimation of bone permeability using accurate microstructural measurements. J. Biomech. 39: 2378–87.

Biot M.A (1941) General theory of three-dimensional consolidation. J. Appl. Phys. 12: 155-164.

Cowin SC (1999) Bone poroelasticity. J. Biomech. 32: 217-238

Cowin SC, Doty SB (2007) Tissue Mechanics. Springer. pp 348, 360

Cowin SC, Gailani G, Benalla M (2009) Hierarchical Poroelasticity: Movement of interstitial fluid between porosity levels in bones. Phil. Trans. R. Soc. 367: 3401–43

Cowin SC, Mehrabadi MM (2007) Compressible and Incompressible Constituents in Anisotropic Poroelasticity: The Problem of Unconfined Compression of a Disk. J. Mech. Phys. Solids, 55: 161–193.

Cowin SC, Moss-Salentijn L, Moss ML (1991) Candidates for the Mechanosensory System in Bone. J. Biomech. Eng. 113: 191–197

Cowin SC, Weinbaum S, Zeng Y (1995) A case for bone canaliculi as the anatomical site of strain-generated potentials. J. Biomech. 28: 1281-96

Dong XN, Zhang X, Guo XE (2005) Interfacial Strength of Cement Lines in Human Cortical Bone. Mech. Chem. Biosyst., 2(2): 63–68.

Espinoza Orías AA, Deuerling JM, Landrigan MD, Renaud JE, Roeder RK (2009) Anatomic variation in the elastic anisotropy of cortical bone tissue in the human femur. J. J Mech Behav Biomed Mater. 3:255-63.

Frasca P, Harper RA, Katz JL (1976) Isolation of Single Osteons and Osteon Lamellae. Acta Anat. (Basel). 95: 122–129.

Fritton SP, Weinbaum S (2009) Fluid and solute transport in bone: Flow induced mechanotransduction. Annu. Rev. Fluid Mech. 41: 347–74

Galli M, Oyen ML (2009) Fast identification of poroelastic parameters from indentation tests. Comput Model Eng Sci 48:241–270

Gailani GB, Benalla M, Mahamud R, Cowin SC, Cardoso L (2009) Experimental Determination of the Permeability in the Lacunar-Canalicular Porosity of Bone. J. Biomech. Eng. 131: 1010071-7

Gailani GB, Cowin SC (2008) The unconfined compression of a poroelastic annular cylindrical disk. Mechanics of Materials. 40: 507-23

Gailani G, Cowin S (2011) Ramp loading in Russian doll poroelasticity. J. Mech. Phys.Solids. 59: 103-120

Gardinier JD, Townend CW, Jen KP, Wu Q, Duncan RL, Wang L (2010) In situ permeability measurement of the mammalian lacunar-canalicular system. J. Bone 46: 1075-81

Gururaja S, Kim HJ, Swan CC, Brand RA, Lakes RS (2005) Modeling deformation-induced fluid flow in cortical bone's canalicular–lacunar system. Ann. Biomed. Eng. 33: 7- 25

Kameo Y, Adachi T, Sato N, Hojo M (2010) Estimation of bone permeability considering the morphology of lacuno-canalicular porosity. Journal of the Mechanical Behavior of Biomedical Materials , 3: 240-248

Marotti, G (1996) The structure of bone tissue and the cellular control of their deposition. Italian Journal of Anatomy and Embryology 4: 25–79.

Oyen ML (2008) Poroelastic nanoindentation responses of hydrated bone. J. Mater. Res. 23: 1307-14

Remaggi F, Cane V, Palumbo C, Ferretti M (1998) Histomorphometric study on the osteocyte lacuno-canalicular network in animals of different species. I. Woven-fibered and parallel fibered bones. Italian Journal of Anatomy and Embryology 103: 145–155

Rice JR, Cleary MP (1976) Some basic stress diffusion solutions for fluid-saturated elastic porous media with compressible constituents. Rev. Geophys. Space Phys. 14: 227-241

Smit TH, Huyghe JM, Cowin SC (2002) Estimation of the poroelastic parameters of bone. J. Biomech. 35: 829-36.

Thompson M and Willis J R (1991) A reformation of the equations of anisotropic poroelasticity. J. Appl. Mech. 58: 612-616

Wagner DW, Lindsey DP, Beaupre GS (2011) Deriving tissue density and elastic modulus from microCT bone scans J. Bone. 49(5):931-8

Wang L, Fritton SP, Cowin SC, Weinbaum S (1999) Fluid pressure relaxation depends upon osteonal microstructure: modeling an oscillatory bending experiment. J. Biomech. 32: 663-72

Weinbaum S, Cowin SC, Zeng Y (1994) A model for the excitation of osteocytes by mechanical loading-induced bone fluid shear stresses. J. Biomech. 27: 339-60

You LD, Weinbaum S, Cowin SC, Schaffler MB (2004) Ultrastructure of the osteocyte process and its pericellularmatrix. Anat. Rec. 278:A505–13

Zeng Y, Cowin SC, Weinbaum S (1994) A fiber matrix model for fluid flow and streaming potentials in the canaliculi of an osteon. Ann. Biomed. Eng. 22: 280–92

Zhang D, Weinbaum S, Cowin SC (1998) Estimates of the peak pressures in the bone pore water. J. Biomech. Eng. 120: 697-703

Zhou X, Novotny JE, Wang L (2008) Modeling fluorescence recovery after photobleaching in loaded bone: potential applications in measuring fluid and solute transport in the osteocytic lacunar–canalicular system. Ann. Biomed. Eng. 36: 1961–77

Chapter 5

Conclusion and future work

5.1. Conclusion

The permeability of the lacunar-canalicular porosity is a major determinant of the fluid flow in the lacunar-canalicular porosity. Interstitial fluid flow is believed to be at the origin of the mechanosensation phenomena in bone since it exerts a drag force on the cell process of osteocytes. The drag force is thought to be transformed into biochemical signals that modulate the rate of resorption and formation of bone. Therefore, changes on PLC permeability are considered to have an important role in bone mechanosensation.

During the last decade, the PLC permeability has been investigated by different means, including theoretical and experimental approaches. Theoretical studies have been mainly based on poroelasticity and the analysis of the ultrastructure of the canalicular network. The experimental approaches have relied on indirect determination of the PLC by combining FEM or analytical model with measurements in cortical bone using nanoindentation, imaging of tracer diffusivity using confocal microscopy, and micromechanical loading. Not yet explained is the fact that the PLC permeability measurements reported in the literature are several orders of magnitude below the values predicted by analytical studies. It is possible that the PLC permeability has not been determined with sufficient accuracy. The discrepancy between theoretical and experimental values of PLC permeability could be due to the many assumptions and unknowns in theoretical work, as well as the difficulty to control experimental conditions, the variability of testing methods and tested samples. All these factors represent a set of important possible limitations preventing the accurate assessment of the PLC permeability.

The aim of this thesis was to determine the PLC permeability with higher accuracy than in previous approaches. A major difficulty in accurately assessing the PLC permeability is

associated with the topological intertwining of the vascular and the lacunar-canalicular porosities at the microscopic scale. To overcome this limitation, the work presented in chapter 3 and 4 was designed to be applied to a single osteon, a domain in which the interaction of interstitial fluid flow in the PLC can be separated from the PV.

The analytical study in chapter 3 was also designed to investigate the frequency dependent behavior of a poroelastic annular disk representative of an osteon, with material properties and boundary conditions that are considered similar to the ones existing in cortical bone. Importantly, this analytical study has shown that 1) the lacunar-canalicular porosity is the most influential parameter of the PLC permeability, 2) the elastic properties of the mineralized tissue matrix are the second most influential parameter on the permeability, but to a lesser extent than the effect produced by the PLC on PLC permeability, and 3) the PLC permeability changes as a function of the loading frequency. In conclusion, the analytical study demonstrated the feasibility of determining the PLC permeability without the influence of the PV using a single osteon. It also allowed the identification of parameters that need to be measured for each osteon to increase the accuracy of the PLC permeability assessment.

Based on the results of the analytical study, an experimental apparatus was constructed to measure the PLC permeability through curve fitting of the analytical model to experimental data on the lag time between the measured cyclic stresses produced by cyclic strains in an osteon sample. Important improvements of our experimental approach versus the approaches of previous studies were 1) the isolation of fresh human samples that contain the PLC only, 2) the measurement of the lacunar porosity from μCT images, 3) the estimate of the canalicular porosity and the elastic modulus of the mineralized matrix material for each osteon from μCT images. Since the material properties vary from one osteon to the other depending on several

parameters such as, bone mineral density, number of lacunae, inner and outer diameter, we consider that by evaluating the tissue properties for each osteon, we have achieved PLC permeability measurements that could be considered closer to the true value of the permeability *in vivo*.

Important observations were made in this experimental study, in particular, the one concerning the change in properties of the mineralized tissue material a few hours after isolation of the osteon from the frozen whole bone. Such changes are small, less than 1% in loss tangent, and their contribution is almost negligible with regard to PLC permeability, if the testing is performed within 5 hours after isolation of the osteon. Changes in properties of the osteon are more significant after a few days, from which one may conclude that the lack of freshness of the sample could actually contribute to differences reported in the literature.

Previous studies in literature have reported that the PLC permeability varies across different animal species, such as mice, rat, dog, cow, etc. In this thesis, the PLC permeability was investigated in aged human bone; therefore, the PLC permeability measured in this study may be specific to the range of age of the donors, and cannot be generalized to donors of different age or to other species. More studies using the same experimental approach, and including samples from different age and bones would need to be performed to determine whether age or skeletal site are determinant factors of variability in PLC permeability reported in the literature.

Based on the experimental study the following conclusions were drawn: 1) the PLC permeability is frequency dependent; 2) a strong correlation between porosity and permeability exists in the lacunar canalicular domain within the range of porosity analyzed; and 3) the PLC

permeability may decrease by approximately 35% when the loading frequency increases from 1 to 100Hz, suggesting that bone loading and physical activity (i.e. walking, running, muscle contraction) at different frequencies may result in changes in the PLC permeability. It is possible that this decrease with increasing frequency may have an effect on bone mechanosensation.

In summary, an analytical and experimental framework that permits analyzing the PLC permeability of bone has been developed. A contribution has been made to the understanding of *why the theoretical and experimental values reported in the literature of the PLC are different by several orders of magnitude. This report contains more accurate measurements of the PLC permeability of human bone than previously reported. It also documents the frequency dependence of the PLC permeability*. The frequency dependent PLC permeability in bone could have major implications for bone mechanosensation, but at the present time, it remains a major question to be explored. Possible future work is suggested in the next section.

5.2. Future work

5.3.1 Formulation of the permeability vs. the porosity in the PLC

In this thesis, it was observed that the lacunar-canalicular porosity is directly proportional to the permeability. Indeed, Figure 4-10 shows a high correlation (R= 95%) between experimental data of permeability and porosity. Therefore, the equation of the model fit, $K_{rr} = (1.54\phi - 0.14)10^{-22}\, m^2$ (Figure 4-10) represents an empirical linear relationship between these two parameters in the PLC. If the validity of this empirical equation is verified with further theoretical and experimental studies, this novel approach will represent a simpler way to estimate the PLC permeability, based on the measurement of the lacunar-canalicular porosity only.

5.3.2. Determination of the PLC permeability using different osteonal specimens

In this study the specimen is a section of an osteon as shown in Figure 3-2. The Haversian canal is centralized in the middle of the specimen and the cement line surrounds the osteon. The cement line is considered as impermeable and the only opening the PLC porosity has to exchange its interstitial fluid with the PV is through the wall of the Haversian canal. Based on these assumptions the boundary conditions for the ODE in chapter (3), equation (4), were expressed in equations (5) as

$$\frac{\partial \tilde{p}}{\partial \lambda}(1,t) = 0,\ \tilde{p}(a,t) = 0\,, \tag{1}$$

for the cement line and inner wall, respectively. In this forthcoming project we would like to redo the same study using an osteonal sample without the cement line. In this case the boundary conditions for the inner and outer boundaries of the Haversian system will be the same, permitting flow across both boundaries,

$$\tilde{p}(1,t) = 0,\ \tilde{p}(a,t) = 0\,. \tag{2}$$

The most challenging part of this study is the isolation of the osteonal specimen without the cement line. The proposed study may be structured to provide a measure of the permeability of the cement line, if it is nonzero, or to verify its impermeability.

Bibliography

References For Chapter 1

Abramowitz M, Stegun IA (1964) Handbook of Mathematical functions with Formulas, Graphs and Mathematical Tables. National Bureau of Standards Applied Mathematics Series 55, 379- 80

Bonivtch AR, Bonewald LF, Nicolella DP (2007) Tissue strain amplification at the osteocyte lacuna: a microstructural finite element analysis. J Biomech 40(10):2199-2206.

Burr DB, Milgrom C, Fyhrie D, Forwood M, Nyska M, et al. (1996) In vivo measurement of human tibialstrains during vigorous activity. Bone 18:405–10

Cowin SC (1999) Bone poroelasticity. J. Biomech. 32: 217-238

Cowin SC (1981) Mechanical properties of bone. Mechanical of structured media. APS Selvadurai. pp 151- 184.

Cowin SC, Doty SB (2007) Tissue Mechanics. Springer. pp 350, 352

Cowin SC, Doty SB (1989) Bone mechanics. Boca Raton. pp 242, 248

Cowin SC, Gailani G, Benalla M (2009) Hierarchical Poroelasticity: Movement of interstitial fluid between porosity levels in bones. Phil. Trans. R. Soc. 367: 3401–43

Cowin SC, Moss-Salentijn L, Moss ML (1991) Candidates for the mechanosensory system in bone. J. Biomech.Eng. 113:191–97

Fritton SP, Weinbaum S (2009) Fluid and solute transport in bone: Flow induced mechanotransduction. Annu. Rev. Fluid Mech. 41: 347–74

Fritton SP, Rubin CT (2001) In vivo measurement of bone deformations using strain gages. In Bone Mechanics Handbook, ed. SC Cowin, pp. 8.1–8.41. Boca Raton, FL: CRC

Gailani GB, Benalla M, Mahamud R, Cowin SC, Cardoso L (2009) Experimental Determination of the Permeability in the Lacunar-Canalicular Porosity of Bone. J. Biomech. Eng. 131: 1010071-7

Remaggi F, Cane V, Palumbo C, Ferretti M (1998) Histomorphometric study on the osteocyte lacuno-canalicular network in animals of different species. I. Woven-fibered and parallel fibered bones. Italian Journal of Anatomy and Embryology 103: 145–155

Rubin CT, McLeod KJ, Bain SD (1990) Functional strains and cortical bone adaptation: epigenetic assurance of skeletal integrity. JBiomech. 23:43-54.

Turner CH, Pavalko FM (1998) Mechanotransduction and functional response of the skeleton to physical stress: the mechanisms and mechanics of bone adaptation. J Orthop Sci 3:346-355.

Vankan WJ, Huyghe JM, Janssen JD, Huson A (1996) Poroelasticity of saturated solids with an application to blood perfusion. Int. J. Engng Sci. 34,1019-3b

You L, Cowin SC, Schaffler MB,Weinbaum S (2001) A model for strain amplification in the actin cytoskeletonof osteocytes due to fluid drag on pericellular matrix. J. Biomech. 34:1375–86

Zhang D, Weinbaum S, Cowin SC (1998) Estimates of the peak pressures in the bone pore water. J. Biomech. Eng. 120: 697-703

References For Chapter 2

Benalla M, Cardoso L, Cowin SC (2011) Analytical basis of the lacunar-canalicular permeability of bone using cyclic loading. Biomech. Model. Mechanobiol. Accepted: 14 September 2011.

Biot MA (1941) General theory of three-dimensional consolidation. J. Appl. Phys. 12, 155-164.

Biot MA (1955) Theory of elasticity and consolidation for a porous anisotropic solid. J. Appl. Phys. 26: 182-182.

Biot MA (1956-a) General solution of the equations of elasticity and consolidation for a porous material. J. of Applied Mechanics, Trans. ASME, v78, pp. 91-96

Biot MA (1956-b) Theory of propagation of elastic waves in a fluid saturated porous solid, parts I and II. J. of the Acoustical Society of America, v28, pp. 168-91

Carroll MM (1979) An Effective Stress Law for Anisotropic Elastic Deformation, *J. Geophys. Res.* 84:7510-7512.

Cowin SC, Gailani G, Benalla M (2009) Hierarchical Poroelasticity: Movement of interstitial fluid between porosity levels in bones. Phil. Trans. R. Soc. 367: 3401–43

Cowin SC, Mehrabadi MM (2007) Compressible and incompressible constituents in anisotropic poroelasticity: The problem of unconfined compression of a disk. *J. Mech. Phys. Solids.* ***55****:*161-193.

Cowin SC, Doty SB (2007) *Tissue Mechanics*. Springer

Darcy H (1856) *Les Fontains Publiques de la Ville de Dijon*, Dalmont: Paris.

Gailani GB, Cowin SC (2008) The unconfined compression of a poroelastic annular cylindrical disk. *Mechanics of Materials* 40:507-523.

Gailani GB, Benalla M, Mahamud R, Cowin SC, Cardoso L (2009) Experimental Determination of the Permeability in the Lacunar-Canalicular Porosity of Bone. J. Biomech. Eng. 131: 1010071-7

Nur A, Byerlee JD (1971) An exact effective stress law for elastic deformation of rock with fluids. *J. Geophys. Res.* **76**:6414.

References For Chapter 3

Abramowitz M, Stegun IA (1964) Handbook of Mathematical functions with Formulas, Graphs and Mathematical Tables. National Bureau of Standards Applied Mathematics Series 55, 379- 80

Beno T, Yoon YJ, Cowin SC, Fritton SP (2006) Estimation of bone permeability using accurate microstructural measurements. J. Biomech. 39: 2378–87

Buechner PM, Lakes RS (2003) Size effects in the elasticity and viscoelasticity of bone. Biomech. Model. Mechanobiol. 1: 295 – 301

Burger EH, Klein-Nulend J, van der Plas A, Nijweide PJ (1995) Function of Osteocytes in Bone–Their Role in Mechanotransduction. J. Nutr. 125(7 Suppl):2020S-2023S

Ciani C, Ramirez Marin PA R, Doty SB, Fritton SP (2007) Bone microstructure in OVX and normal rat bone as revealed by confocal and electron microscopy. Bioengineering Conference, 2007. NEBC '07. IEEE 33rd Annual Northeast. 23-24

Cowin SC (1999) Bone poroelasticity. J. Biomech. 32: 217-238

Cowin SC (2001) Bone mechanics handbook. 2nd edn Boca Raton, FL: CRS Press. 17: 2-5

Cowin SC, Doty SB (2007) Tissue Mechanics. Springer. pp 348, 360

Cowin SC, Gailani G, Benalla M (2009) Hierarchical Poroelasticity: Movement of interstitial fluid between porosity levels in bones. Phil. Trans. R. Soc. 367: 3401–43

Cowin SC, Moss-Salentijn L, Moss ML (1991), ‘‘Candidates for the Mechanosensory System in Bone,’’ J. Biomech. Eng. 113: 191–197

Cowin SC, Weinbaum S, Zeng Y (1995) A case for bone canaliculi as the anatomical site of strain-generated potentials, J. Biomech. 28: 1281-96

Drabousky DP (2009) Prony Series Representation and Interconversion of Viscoelastic Material Functions of Equine Cortical Bone. Department of Mechanical and Aerospace Engineering, Western Reserve University

Fornells P, García-Aznar JM, Doblaré M (2007) A finite element dual porosity approach to model deformation-induced fluid flow in cortical bone. Ann. Biomed. Eng. 35: 1687–1698

Fritton SP, Wang L, Weinbaum S, Cowin SC (2001) Interaction of mechanical loading, blood flow, and interstitial fluid flow in osteonal bone. Proceedings of the Bioengineering conference. BED 50: 341-42

Fritton SP, Weinbaum S (2009) Fluid and solute transport in bone: Flow induced mechanotransduction. Annu. Rev. Fluid Mech. 41: 347–74

Gailani GB, Benalla M, Mahamud R, Cowin SC, Cardoso L (2009) Experimental Determination of the Permeability in the Lacunar-Canalicular Porosity of Bone. J. Biomech. Eng. 131: 1010071-7

Gailani GB, Cowin SC (2008) The unconfined compression of a poroelastic annular cylindrical disk. Mechanics of Materials. 40: 507-23

Gardinier JD, Townend CW, Jen KP, Wu Q, Duncan RL, Wang L (2010). In situ permeability measurement of the mammalian lacunar-canalicular system. J. Bone 46: 1075-81

Garner E, Lakes R, Lee T, Swan C, Brand R (2000) Viscoelastic dissipation in compact bone: implications for stress-Induced fluid flow in bone. J. Biomech. Eng. 122: 167-172

Goulet GC, Coombe D, Martinuzzi RJ, Zernicke RF (2009) Poroelastic evaluation of fluid movement through the lacunocanalicular system. Ann. Biomed. Eng. 37-7: 1390–1402

Gururaja S, Kim HJ, Swan CC, Brand RA, Lakes RS (2005) Modeling deformation-induced fluid flow in cortical bone's canalicular–lacunar system. Ann. Biomed. Eng. 33: 7- 25

Han Y, Cowin SC, Schaffler MB, Weinbaum S (2004) Mechanotransduction and strain amplification in osteocyte cell processes and flow across the endothelial glycocalyx. Proc. Nat. Acad. Sci. USA. 101: 16689-94

Jee W (1988) The skeletal tissues. In L. Weiss (Ed.), Cell and Tissue Biology: a Textbook of Histology. Baltimore: Urban & Schwarzenberg. pp 207

Kameo Y, Adachi T, Sato N, Hojo M (2010) Estimation of bone permeability considering the morphology of lacuno-canalicular porosity. Journal of the Mechanical Behavior of Biomedical Materials , 3: 240-248

Lakes RS (1982) Dynamical study of couple stress effects in human compact bone. J. Biomech. Eng. 104: 7–11

Nguyen V, Lemaire T, Naili S (2009) Numerical study of deformation-induced fluid flows in periodic osteonal matrix under harmonic axial loading. C. R. Mecanique. 337: 268–76

Oyen ML (2008) Poroelastic nanoindentation responses of hydrated bone. J. Mater. Res. 23: 1307-14

Ramtani S (2007) Parametric sensitivity analysis applied to a specific one-dimensional internal bone remodeling problem. Computers in Biology and Medicine. 37: 1203 – 09

Rémond A, Naïli S, Lemaire T (2008) Interstitial fluid flow in the osteon with spatial gradients of mechanical properties: a finite element study. Biomech. Model. Mechanobiol. 7: 487–95

Smit TH, Huyghe JM, Cowin SC (2002) Estimation of the poroelastic parameters of bone. J. Biomech. 35: 829-36.

Swan CC, Lakes RS, Brand RA, Stewart KJ (2003) Micromechanically based poroelastic modeling of fluid flow in Haversian bone. J. Biomech. Eng. 125: 25-37

Wang L, Fritton SP, Cowin SC, Weinbaum S (1999) Fluid pressure relaxation depends upon osteonal microstructure: modeling an oscillatory bending experiment. J. Biomech. 32: 663-72

Wang L, Fritton SP, Weinbaum S, Cowin SC (2003) On bone adaptation due to venous stasis. J. Biomech. 36: 1439-51

Weinbaum S, Cowin SC, Zeng Y (1994) A model for the excitation of osteocytes by mechanical loading-induced bone fluid shear stresses. J. Biomech. 27: 339-60

Wu D, Ci S, Luo H (2011). A theoretical framework for interaction measure and sensitivity analysis in cross-layer design. ACM Transactions on Modeling and Computer Simulation. 21: 1-26

Yang G, Kabel J, Rietbergen BV, Odgaard A, Huiskes R, Cowin SC (1999). The Anisotropic Hooke's Law for Cancellous Bone and Wood. Journal of Elasticity. 53: 125–146

Zeng Y, Cowin SC, Weinbaum S (1994) A fiber matrix model for fluid flow and streaming potentials in the canaliculi of an osteon. Ann. Biomed. Eng. 22: 280–92

Zhang D, Weinbaum S, Cowin SC (1998) Estimates of the peak pressures in the bone pore water. J. Biomech. Eng. 120: 697-703

Zhou X, Novotny JE, Wang L (2008) Modeling fluorescence recovery after photobleaching in loaded bone: potential applications in measuring fluid and solute transport in the osteocytic lacunar–canalicular system. Ann. Biomed. Eng. 36: 1961–77

References For Chapter 4

Ascenzi A, Baschieri P, Benvenuti A (1994) The Torsional Properties of Single Selected Osteons. J. Biomech., 27(7): 875–884.

Ascenzi A, Benvenuti M, Mango F, Similia R (1985) Mechanical Hysteresis Loops From Single Osteons: Technical Devices and Preliminary Results. J. Biomech. 18(5): 391–398.

Ascenzi A, Bonucci E (1968) The Compressive Properties of Single Osteons. Anat. Rec. 161: 377–391.

Ascenzi A, Fabry C (1959) Technique for Dissection and Measurement of Refractive Index of Osteons. J. Biophys. Biochem. Cytol. 6: 139–143.

Benalla M, Cardoso L, Cowin SC (2011) Analytical basis of the lacunar-canalicular permeability of bone using cyclic loading. Biomech. Model. Mechanobiol. Accepted: 14 September 2011.

Beno T, Yoon YJ, Cowin SC, Fritton SP (2006) Estimation of bone permeability using accurate microstructural measurements. J. Biomech. 39: 2378–87.

Biot M.A (1941) General theory of three-dimensional consolidation. J. Appl. Phys. 12: 155-164.

Cowin SC (1999) Bone poroelasticity. J. Biomech. 32: 217-238

Cowin SC, Doty SB (2007) Tissue Mechanics. Springer. pp 348, 360

Cowin SC, Gailani G, Benalla M (2009) Hierarchical Poroelasticity: Movement of interstitial fluid between porosity levels in bones. Phil. Trans. R. Soc. 367: 3401–43

Cowin SC, Mehrabadi MM (2007) Compressible and Incompressible Constituents in Anisotropic Poroelasticity: The Problem of Unconfined Compression of a Disk. J. Mech. Phys. Solids, 55: 161–193.

Cowin SC, Moss-Salentijn L, Moss ML (1991) Candidates for the Mechanosensory System in Bone. J. Biomech. Eng. 113: 191–197

Cowin SC, Weinbaum S, Zeng Y (1995) A case for bone canaliculi as the anatomical site of strain-generated potentials. J. Biomech. 28: 1281-96

Dong XN, Zhang X, Guo XE (2005) Interfacial Strength of Cement Lines in Human Cortical Bone. Mech. Chem. Biosyst., 2(2): 63–68.

Espinoza Orías AA, Deuerling JM, Landrigan MD, Renaud JE, Roeder RK (2009) Anatomic variation in the elastic anisotropy of cortical bone tissue in the human femur. J. J Mech Behav Biomed Mater. 3:255-63.

Frasca P, Harper RA, Katz JL (1976) Isolation of Single Osteons and Osteon Lamellae. Acta Anat. (Basel). 95: 122–129.

Fritton SP, Weinbaum S (2009) Fluid and solute transport in bone: Flow induced mechanotransduction. Annu. Rev. Fluid Mech. 41: 347–74

Galli M, Oyen ML (2009) Fast identification of poroelastic parameters from indentation tests. Comput Model Eng Sci 48:241–270

Gailani GB, Benalla M, Mahamud R, Cowin SC, Cardoso L (2009) Experimental Determination of the Permeability in the Lacunar-Canalicular Porosity of Bone. J. Biomech. Eng. 131: 1010071-7

Gailani GB, Cowin SC (2008) The unconfined compression of a poroelastic annular cylindrical disk. Mechanics of Materials. 40: 507-23

Gailani G, Cowin S (2011) Ramp loading in Russian doll poroelasticity. J. Mech. Phys.Solids. 59: 103-120

Gardinier JD, Townend CW, Jen KP, Wu Q, Duncan RL, Wang L (2010) In situ permeability measurement of the mammalian lacunar-canalicular system. J. Bone 46: 1075-81

Gururaja S, Kim HJ, Swan CC, Brand RA, Lakes RS (2005) Modeling deformation-induced fluid flow in cortical bone's canalicular–lacunar system. Ann. Biomed. Eng. 33: 7- 25

Kameo Y, Adachi T, Sato N, Hojo M (2010) Estimation of bone permeability considering the morphology of lacuno-canalicular porosity. Journal of the Mechanical Behavior of Biomedical Materials , 3: 240-248

Marotti, G (1996) The structure of bone tissue and the cellular control of their deposition. Italian Journal of Anatomy and Embryology 4: 25–79.

Oyen ML (2008) Poroelastic nanoindentation responses of hydrated bone. J. Mater. Res. 23: 1307-14

Remaggi F, Cane V, Palumbo C, Ferretti M (1998) Histomorphometric study on the osteocyte lacuno-canalicular network in animals of different species. I. Woven-fibered and parallel fibered bones. Italian Journal of Anatomy and Embryology 103: 145–155

Rice JR, Cleary MP (1976) Some basic stress diffusion solutions for fluid-saturated elastic porous media with compressible constituents. Rev. Geophys. Space Phys. 14: 227-241

Smit TH, Huyghe JM, Cowin SC (2002) Estimation of the poroelastic parameters of bone. J. Biomech. 35: 829-36.

Thompson M and Willis J R (1991) A reformation of the equations of anisotropic poroelasticity. J. Appl. Mech. 58: 612-616

Wagner DW, Lindsey DP, Beaupre GS (2011) Deriving tissue density and elastic modulus from microCT bone scans J. Bone. 49(5):931-8

Wang L, Fritton SP, Cowin SC, Weinbaum S (1999) Fluid pressure relaxation depends upon osteonal microstructure: modeling an oscillatory bending experiment. J. Biomech. 32: 663-72

Weinbaum S, Cowin SC, Zeng Y (1994) A model for the excitation of osteocytes by mechanical loading-induced bone fluid shear stresses. J. Biomech. 27: 339-60

You LD, Weinbaum S, Cowin SC, Schaffler MB (2004) Ultrastructure of the osteocyte process and its pericellularmatrix. Anat. Rec. 278:A505–13

Zeng Y, Cowin SC, Weinbaum S (1994) A fiber matrix model for fluid flow and streaming potentials in the canaliculi of an osteon. Ann. Biomed. Eng. 22: 280–92

Zhang D, Weinbaum S, Cowin SC (1998) Estimates of the peak pressures in the bone pore water. J. Biomech. Eng. 120: 697-703

Zhou X, Novotny JE, Wang L (2008) Modeling fluorescence recovery after photobleaching in loaded bone: potential applications in measuring fluid and solute transport in the osteocytic lacunar–canalicular system. Ann. Biomed. Eng. 36: 1961–77